ABSTRACT

Title of dissertation: THE CLIMATE IMPACT OF
THE MESSINIAN SALINITY
CRISIS

Lisa Nicole Murphy, Doctor of Philosophy, 2010

Dissertation directed by: Assistant Professor Daniel Kirk-Davidoff
Department of Atmospheric and Oceanic Science

This study uses an atmospheric general circulation model to examine the regional and global climate response to the Messinian Salinity Crisis (MSC) $\sim$6 Ma. During this time, the tectonic collision of the African and European plates isolated the Mediterranean Sea (MedSea) from the Atlantic Ocean. MedSea level is estimated to have fallen between 1000-2000 m and desiccation may have lasted for 90 kyr. Our results show that the substantial MedSea depression generates planetary-scale atmospheric waves responsible for significant climate effects throughout the Northern Hemisphere. A notable deepening of the Aleutian Low and a significant equatorward shift in the Atlantic jet stream are evident.

Cyclical patterns in Messinian sediments suggest alternating wet and dry climate during the MSC. These cycles have been attributed to variations in the Earth's precession. This is the first study to detail how reduced MedSea level alters orbitally-driven climate change during the Late Miocene. Reduced MedSea level results in wetter conditions to the Northeast, in particular the Alps, consistent with proxy

data. This signal is robust under all precession signals and is supported by evidence of greater weathering of the Alps during the MSC. Desiccation and lowered MedSea level results in greater precipitation over the Guinea Coast region of North Africa. Greater runoff from this region is supported by proxy evidence of higher monsoon intensity and enhanced total organic carbon accumulation throughout the Messinian.

We couple our model to an online aerosol model to examine the response of dust to varying orbital parameters and to MedSea desiccation. Modeling dust source and transport changes in response to decreased dustiness during precession minimum shows that warmer tropical North Atlantic SSTs, attributed to increased insolation in the absence of dust, enhances evaporation and favors more precipitation over the western tropical North Atlantic. This stresses the importance of allowing dust to respond to climate change and including prognostic dust in paleo-simulations that examine changes in the West African monsoon.

Enhanced dust loading over the tropical North Atlantic Ocean occurs when the Mediterranean is desiccated. This reduces the net radiative flux at the surface, which cools SSTs north of the Equator and shifts the ITCZ towards the Southern Hemisphere, consistent with theories that link African dust with extended Sahel droughts. Greater ocean productivity results from nutrient rich iron-laden dust waters, which is consistent with increased benthic foraminiferal accumulation rates off the African coast between 5.8 Ma and 5.25 Ma. The dustier Northern Hemisphere inhibits convective precipitation in the tropical North Atlantic and large-scale precipitation over Eastern Europe and into Central Asia, in agreement with proxy

evidence of greater aridity in these regions between 6.2 and 5 Ma. Our results show that a desiccated Mediterranean has a significant impact on Northern Hemisphere sea-ice formation during precession maximum, which agrees with $\delta^{18}O$ proxies. Sea ice growth spreads southward, especially in the Labrador and Bering Seas. Interestingly, proxy data studies show discontinuous sea-ice in the Labrador Sea and south of Greenland, as well as concurrent ice-rafting in both the northwest Pacific and Gulf of Alaska sites in the late Miocene, a few million years prior to Northern Hemisphere glaciation.

THE CLIMATE IMPACT OF THE MESSINIAN SALINITY CRISIS

by

Lisa Nicole Murphy

Dissertation submitted to the Faculty of the Graduate School of the
University of Maryland, College Park in partial fulfillment
of the requirements for the degree of
Doctor of Philosophy
2010

Advisory Committee:
Assistant Professor Daniel Kirk-Davidoff, Chair/Advisor
Professor James Carton
Professor Sumant Nigam
Professor Natalie Mahowald
Associate Professor Michael Evans, Dean's Representative

Foreword

Chapter 3 of this dissertation is an edited verision of the manuscript: Murphy, L.N., D.B. Kirk-Davidoff, N. Mahowald, B.L. Otto-Bliesner, 2009: A numerical study of the climate response to lowered Mediterranean Sea level during the Messinian Salinity Crisis, Palaeo., Palaeo., Palaeo., 279, 41-59.

Acknowledgments

I would like to take some time to thank everyone in my life for all the support, love and encouragment especially over these past 5 years. First and foremost I would like to thank all the women of my family. My incredible mother, grandmother, aunt and sister. You gave me the courage to go forward in my career and the values that I needed to succeed. You are such hardworking, strong and independent women and I will always look up to you. To my sister, Laura, for always knowing how to make me laugh. I know I can always count on you to cheer me up after I've had a bad day. To the rest of my family: I love you all so much. Thank you for all your love and support over the past 23 years of schooling. Finally, to my wonderful husband, Marlos. I could never have made it here without you! Thank you for all of your help along the way. And most of all thanks for loving me.

I would like to thank my advisor, Dr. Daniel Kirk-Davidoff, for all of his guidance, words of wisdom, and especially for his patience at the beginning. I needed your support and you were there to give it!

Thank you to NCAR for the computer resources and especially Christine Shields, Natalie Mahowald, Bette Otto-Bliesner, Dani Bundy, and Sam Levis for their much needed advice.

I would also like to thank all of the dear friends that I have had the privledge to meet here at the University of Maryland. To Alan Cohn and Megan Linkin. Thank you for all the wonderful memories and good times. To Melanie Cook and Zahra Chaudry for being amazing and providing shelter when I was homeless! To Melanie

Table of Contents

List of Tables

List of Figures

List of Abbreviations

MedSea	Mediterranean Sea
MSC	Messinian Salinity Crisis
US	Upper Sea
LS	Lower Sea
LL	Lower Land
HL	Half Land
P-	Precession Minimum
P+	Precession Maximum

Chapter 1

Introduction

1.1 Abstract

Roughly six million years ago, tectonic movements isolated the Mediterranean Sea (MedSea) from the Atlantic Ocean, an event known as the Messinian Salinity Crisis (MSC). Subsequent evaporative drawdown of the MedSea resulted in a sub-aerial depression with a depth between 1500-2500 m. During the Late Messinian, paleoclimate records indicate enhanced productivity in the Atlantic Ocean, increased aridity in Central Asia, and glaciation in the Northern hemisphere. Nevertheless the mechanisms that generate such changes are still speculative. Here we use the NCAR Community Atmosphere Model coupled with a Slab Ocean Model (CAM-SOM) to examine the regional and global climate response to the complete desiccation and reduced MedSea level during the late Miocene.

Our results show that the substantial MedSea depression generates planetary-scale atmospheric waves responsible for significant climate effects throughout the Northern Hemisphere. A notable deepening of the Aleutian Low and a significant equatorward shift in the Atlantic jet stream are evident. In DJF, vertical ascent at the northern margin of the MedSea results in a 1.5-2.5 mm day^{-1} precipitation anomaly at reduced MedSea level over the Alps, consistent with proxy data. Annual mean area averaged MedSea evaporation is slightly higher than control conditions. Ex-

cept when salinity is a substantial barrier to evaporation, our results suggest that a partially filled basin cannot exist in equilibrium and the MedSea must either be partly connected to the Atlantic Ocean or completely desiccated. Base level lowering, which alters the water budget, must be taken into account when considering the freshwater budget during the MSC.

Cyclical patterns in Messinian sediments suggest alternating wet and dry climate during the MSC. These cycles have been attributed to variations in the Earth's precession. We examine how orbital variations, namely precession maximum (P+) and minimum (P-), drive hydrological changes during the MSC. This is the first study to detail how reduced MedSea level (Lowered Sea, LS) alters orbitally-driven climate change during the Late Miocene. The spatial pattern of anomalous precipitation over the MedSea with wetter conditions in the NE and drier conditions in the SW in consistent under all precession signals and is supported by evidence of greater weathering over the Alps during the MSC (Willett *et al.* (2006)). Desiccation and lowered MedSea level results in higher precipitation over the Guinea Coast region of North Africa. Greater runoff from this region is supported by proxy evidence of higher monsoon intensity and enhanced total organic carbon accumulation. The hydrological cycle of Northern Africa is sensitive to both precession changes and MedSea level changes.

We couple CAM-SOM to an online aerosol model to examine the effect of precession changes on dust production and the effect of a desiccated MedSea. Modeling the dust source and transport changes in response to decreased dustiness during precession minimum shows that warmer tropical North Atlantic SSTs, attributed to

increased insolation in the absence of dust, enhances evaporation and favors more precipitation over the western tropical North Atlantic. This stresses the importance of allowing dust to respond to climate change and including dust feedbacks in paleo-simulations that examine changes in the West African monsoon.

Enhanced dust loading over the tropical North Atlantic Ocean occurs when the Mediterranean is desiccated. This reduces the net radiative flux at the surface, which cools SSTs north of the Equator and shifts the ITCZ towards the Southern Hemisphere, consistent with theories that links African dust with extended Sahel droughts. Greater ocean productivity results from nutrient rich iron-laden dust waters, which is consistent with increased benthic foraminiferal accumulation rates off the African coast between 5.8 and 5.25 million years ago (denoted Ma for mega-annum). The dustier Northern Hemisphere inhibits convective precipitation in the tropical North Atlantic and large-scale precipitation over Eastern Europe and into Central Asia, in agreement with proxy evidence of greater aridity in these regions between 6.2 and 5 Ma.

Our results show that a desiccated Mediterranean has a significant impact on Northern Hemisphere sea-ice formation during precession maximum, which agrees with $\delta^{18}O$ proxies. Sea ice growth spreads southward, especially in the Labrador and Bering Seas. Interestingly, proxy data studies show discontinuous sea-ice cover from the Labrador Sea to the south of Greenland, and concurrent ice-rafting in both the northwest Pacific and Gulf of Alaska sites in the late Miocene, a few million years prior to Northern Hemisphere glaciation.

1.2   Introduction

Paleoclimate records indicate enhanced productivity in the Atlantic Ocean, increased aridity in Central Asia, and glaciation in the Northern hemisphere during the late Messinian. Nevertheless the mechanisms that generate such changes are still speculative. One possible source is the oceanographic isolation of the Mediterranean Sea (MedSea), which resulted in substantial MedSea level fall beginning at 5.96 Ma and desiccation between 5.59 to 5.50 Ma. This spectacular event occurred in the Messinian (7 to 5.3 Ma), the last stage of the Miocene epoch (23.8 to 5.3 Ma), and is known as the Messinian Salinity Crisis (MSC). From a climate dynamics perspective, the MSC is an illuminating event to study, yet sophisticated modeling tools have not been used to shed light on the regional and global climate impacts triggered by the MSC. Hydrological changes may have important feedbacks on the climate system. This may bring sizeable climate impacts from regional to hemispheric scales. One interesting aspect to examine includes the effect of topography on climate. Topographic forcing can result in the propagation of Rossby waves, which can link external forcing in one location to more distant locations via teleconnections. The MedSea is in an ideal location to study storm track effects due to its proximity to the Atlantic/North African/Asian waveguide. Focusing our analysis on the large-scale pattern of variability that results from anomalous forcing will allow us validate our simulated atmospheric response against the geological proxy record.

1.2.1 The Messinian Salinity Crisis

The Mediterranean Sea (MedSea), an arid region dominated by atmospheric subsidence, has suffered from a water deficit since the Miocene epoch (Fauquette et al., 2006) when it attained a near-modern configuration. Currently, constant water inflow from the Atlantic Ocean inhibits the MedSea from evaporating. However, roughly 6 Ma, during the late Miocene, the oceanic gateways linking the Atlantic Ocean and MedSea were restricted and closed (Hsu *et al.* (1973)). Evaporative drawdown of the MedSea resulted in a subaerial depression with a depth greater than 1000 m (Hsu *et al.* (1973); Barber, 1981; Gargani and Rigollet, 2007). Evidence of the closure of the straits connecting the Atlantic and the MedSea is found in observations of deep abyssal flow in the North Atlantic Ocean (Hassold et al., 2006). Incised riverbeds along the periphery of the MedSea and a thick (up to 3 km in some regions) unit of evaporites on the MedSea floor (Hsu, 1973; Krijgsman et al, 1999) are evidence of this desiccation. Cyclical variations in the sedimentary pattern suggest high frequency salinity changes attributed to orbital forcing since variations in seasonal insolation can drive changes in the hydrological cycle.

The Messinian was marked by 18 glacial-interglacial cycles (Hodell *et al.* (2001)) and three peaks of glaciation occurred just after the initiation of the Messinian Salinity Crisis (MSC) (Vidal *et al.* (2002)). Evidence of tidewater glaciation dating from the Latest Miocene was discovered in the Yakataga Formation in the Gulf of Alaska (Lagoe et al., 1993). Krissek (1995) gives evidence of ice rafted debris (IRD) between 5.5 and 6 Ma in the Gulf of Alaska and Kurile/Kamchatka (Site 881, $\sim 162°$E,

47°N) regions. In fact two prominent glacial effects occurred during the "Messinian Gap", the final stage of a major drawdown roughly 5.6-5.5 Ma (CIESM, 2008). Sun and Liu (2006) suggested that a 6% reduction in global oceanic salinity during the MSC may have resulted in greater sea ice formation due to the higher freezing point of the lower salinity water.

Messinian deposits in deep ocean basins are rarely preserved and many existing cores are incomplete due to bottom water erosion and severe carbonate dissolution. Nevertheless, a continuous record of the Miocene is found in ODP Site 959 in the eastern equatorial Atlantic. ODP Site 959 is located in the African trade winds region, where ocean biogeochemistry and coastal upwelling play significant roles. Reduced calcium carbonate concentrations and enhanced carbon dissolution is observed off the equatorial African coast between 5.8 and 5.2 Ma, coinciding with the Mediterranean desiccation event. Wagner (2002) suggests that corrosive deep waters were a consequence of reduced global oceanic salinity by more than 6% due to the MSC. A reduction in oceanic salinity causes undersaturation with respect to calcium carbonate and more extensive calcium carbonate dissolution in the ocean (Ryan et al., 1973). Poor preservation of foraminiferal assemblages between 5.75 and 5.4 Ma at Site 959 is noted as a consequence of dissolution effects in Norris (1998). Furthermore, Wagner (2002) observed increased productivity in the eastern North Atlantic at 5.65, 5.6, and 5.55 Ma, a period of global cooling. These peaks coincide with the final isolation, drawdown and erosion of the MedSea that occurred between roughly 5.59 to 5.5 Ma. Diester-Hauss et al. (2003) suggests an additional source of organic matter (food) was active during this time. During this period, an

exposed MedSea floor may become a source region for dust production. Increased dust generation in the Late Miocene may have contributed to spikes in the $\delta^{18}O$ record. Nutrients contained in dust may enhance productivity in marine and terrestrial ecosystems thus sequestering more atmospheric carbon dioxide and cooling global climate. We will examine this theory further through the implementation of an interactive aerosol model.

The enormous change in the level of the MedSea during the MSC can be expected to have brought about significant impacts on the Mediterranean climate. The basin itself must have experienced a substantial warming due to the change in elevation alone. Beyond this obvious impact, topographic changes may be expected to cause a response in the regional geopotential height field patterns that in turn imply changes in the overall regional circulation and storm tracks. Differences in storm track characteristics, such as intensity, frequency and location may result in significant changes in the hydrological cycle of the Mediterranean region (Mariotti *et al.* (2002)). Shifts in storm tracks can lead to droughts or floods, as storms transport copious amounts of heat, moisture and momentum (Chang, 2003). The associated changes in the local water budget may have implications in the surrounding regions by altering the availability of atmospheric moisture.

1.2.2   Topographic forcing on climate

There is a long history of utilizing numerical models to examine the influence of topography on climate (Cook and Held, 1991; Grose and Hoskins, 1978;

7

Kutzbach et al., 1993; Manabe and Terpstra, 1974; Ramstein et al., 1997; Seager et al., 2002; Zhongshi et al., 2007). In our atmosphere, stationary waves, or departures of the extratropical time mean flow from zonal symmetry, can be both orographically and thermally forced (Held and Ting, 1989; Held et al., 2002). Wave propagation is one fundamental way by which fluid carries energy from one location to another. Orographically forced stationary waves can propagate zonally and meridionally, contribute to the forcing of atmospheric jets (Nigam and DeWeaver, 2003), and control the location of storm tracks (Held and Ting, 1989). Storms transport copious amounts of heat, moisture, and momentum, and therefore shifts in storm tracks can lead to substantial regional-scale and hemispheric-scale variability (Chang et al., 2002; Mariotti et al., 2002). Storm tracks and stationary waves are mutually dependent. Heating affects how the flow interacts with orography and forces planetary-scale waves that transport heat, energy, and momentum, resulting in atmospheric teleconnections (Muller and Ambrizzi, 1995; Liu and Alexander, 2007). Anomalous heat and momentum fluxes can then shift storm tracks, resulting in anomalous flow (Held et al., 1989).

According to Wallace and Gutzler (1981), to a first approximation the climatological stationary wave pattern can be described by forced Rossby waves (planetary-scale waves) that are equivalent barotropic. This means that the amplitude of the geopotential and velocity perturbations increase with height while phase lines are constant with height. In a barotropic fluid of constant depth, Rossby waves result from the β-effect, or the gradient of planetary vorticity. Previous studies have shown that outside of forcing regions, barotropic models of linear wave theory are qualitatively

comparable to baroclinic models in representing wave trains (Hoskins and Karoly, 1981; Ambrizzi and Hoskins, 1997). Therefore, stationary waves can be explained by the two-dimensional barotropic Rossby wave propagation. The stationary wave response is dependent on the zonal state as well as size and location of the topographic barrier. Under this assumption, it becomes possible to diagnose the anomalous flow that results from some external forcing.

Linear shallow water theory can be used to separate individual forcing terms from the total atmospheric response (Nigam and DeWeaver, 2003). However, the relative contribution of orographic and thermal forcing to stationary waves has been shown to be dependent on the prescribed low-level zonal mean winds (Held and Ting, 1990). Lee (1995) used a linear barotropic model to show that in a zonally varying background flow barotropic eddy steering controls the location, horizontal structure, and amplitude of storm tracks. Storm track properties critically depend on the properties of the disturbances that interact with the storm track (Lee, 1995; James, 2007). Lee (2000), using a linear barotropic model, found that barotropic dynamics are very important for storm tracks along North Africa and the Middle East. As eddies propagate equatorward from the Atlantic storm track, they receive energy when they encounter cyclonic shear on the poleward side of the subtropical jet. The refractive index can be used to examine wave propagation characteristics. Rossby waves are reflected at turning latitudes where the refractive index is zero and propagate towards critical latitudes where the refractive index becomes very large. Meridionally propagating waves tend to bend towards a large meridional gradient of the absolute vorticity. The subtropical jet, which has a significant gradient in

9

absolute vorticity, therefore creates a waveguide effect, allowing eddies to propagate along the subtropical jet rather than to the equator. These waves may also be meridionally trapped (Lee, 2000; Hoskins, 1983). Perturbations become meridionally trapped in regions of easterlies because the squared refractive index becomes negative. Therefore regions of positive refracted index become preferred Rossby wave propagation paths (Hsu and Lin, 1992).

Held (1983) studied the effects of eliminating mountains and found that in the absence of mountains, the equivalent barotropic trough over eastern North America is significantly reduced and flow across the North Atlantic becomes more zonal. Seager et al. (2002) studied the influence of North American mountains on the thermohaline circulation and temperature contrast between Western Europe and eastern North America, and found that half of the temperature difference is due to forced orographic stationary waves. It is difficult to attribute what features of an anomalous circulation result from orographic and thermal forcing in a GCM. Simple modeling can be used to determine what features of the atmospheric response to external forcing are explained by linear theories of Rossby wave propagation.

Local changes in the Mediterranean region have been shown to have remote impacts in modern observations. The water budget of the MedSea has been positively correlated to the North Atlantic Oscillation (NAO) (Mariotti et al., 2002), a large-scale circulation pattern characterized by a seesaw in the sea level pressure (PSL) between the subtropical Azores high and the Icelandic low. Li et al. (2006) showed that an idealized 2 K cooling of the MedSea resulted in changes to both the Aleutian and Icelandic Lows (Li et al., 2006). This exemplifies the role the MedSea has on the

environment and the teleconnectivity between the Mediterranean and remote locations, suggesting the importance of global modeling as opposed to higher-resolution regional modeling studies.

We will focus our efforts on examining the atmospheric response to both orographic and thermal forcing using an atmospheric general circulation model (AGCM). We shift our focus from questions that are addressable in simpler models to questions that can only be addressed in more sophisticated models. We examine the role of orographic forcing, orbital forcing and dust radiative forcing during the Late Miocene, and compare our model results with the evidence of the paleoclimate record, bringing a critical perspective to both the model output and the paleoclimate reconstruction.

This work is divided into six chapters. Chapter 2 provides a description of the atmospheric general circulation model and boundary conditions used in this study. Chapter 3 examines the influence of orographic forcing on regional and hemispheric climate. Chapter 4 investigates the orbital modulation on the hydrological cycle of the MedSea and North Africa. In Chapter 5, an online dust aerosol model is coupled to the AGCM in order to determine the role of an exposed basin on aerosols and the resulting dust feedback on the Late Miocene climate. Chapter 6 presents a summary and ongoing future work.

Chapter 2

Atmospheric General Circulation Model

2.1 Description of model

In this study on the climate response to the evaporation and desiccation of the Mediterranean Sea during the Messinian Salinity Crisis, we used the NCAR Community Atmosphere Model (CAM) version 3 (Collins *et al.* (2004)) coupled to the Community Land Model (CLM3), a Slab Ocean Model (SOM) and a thermodynamic sea ice model. Although Sea Surface Temperatures (SSTs) in the SOM are able to respond to changes resulting from a modified MedSea and atmospheric changes, the SOM does not simulate the full ocean circulation, but rather assumes seasonally varying but otherwise fixed ocean heat transport. An alternative approach would have been to hold SSTs fixed, while allowing ocean-atmosphere heat fluxes to vary as air temperatures over the ocean changed. Our choice was to allow the mixed layer temperature to adjust to changes in model fluxes, rather than to require large changes in air-sea fluxes to hold SST constant. Climate modeling studies often utilize this SOM/sea ice configuration of CAM (a short list includes: Gibbard et al., 2005; Kirkevag et al., 2008; Mahowald et al., 2006; Maloney and Sobel, 2004; Vavrus et al., 2008), which accounts for oceanic heat transport without incurring the computational costs of implementing a fully dynamic ocean model. For the local changes in the Mediterranean climate investigated here, ocean circu-

lation feedbacks are unlikely to have had a first-order effect on the change due to the MSC. However, ocean-atmosphere feedbacks are more important for the remote effects seen throughout the Northern Hemisphere.

The atmospheric model uses a terrain-following hybrid coordinate with a spectral Eulerian dynamical core and is comprised of 26 vertical levels. The SST dataset in the SOM requires two additional fields specifying mixed layer depths and surface flux balance information. Horizontal oceanic heat transport is represented by compensating heat sources and sinks known as the Q flux, which are derived by running a fixed-SST model to equilibrium, and setting the Q flux equal to the local heating or cooling in the ocean mixed layer that compensates for loss or gain of energy to the atmosphere via the modeled aerodynamic fluxes.

For these experiments CAM3 is run at T42 resolution (an equivalent grid spacing of roughly 2.8°x 2.8°). CAM3 is coupled to the CLM3 (Oleson et al., 2004), which incorporates biogeophysics, hydrological cycle, biogeochemistry and dynamic vegetation. The vegetation is divided into plant functional types (PFT) that are characterized by structure. The vegetation structure, including leaf and stem area index as well as canopy height, is input to each grid cell for each PFT. Due to extensive computational requirements to run with the full dynamic vegetation model, our experiments use fixed, prescribed vegetation. A detailed model description is provided in Collins et al. (2004) and Oleson et al. (2004).

2.2 Isolation of the Mediterranean Sea

While previous AGCM modeling studies of the MSC have used paleo-physiography (Gladstone et al., 2007), they did not examine the impact of desiccation and the

role of Mediterranean Sea level on the atmosphere. We believe our efforts are the first to detail both the regional and global effects due to changes in the MedSea level during the MSC. Five experiments were performed using the NCAR CAM3-SOM to simulate the MedSea base level changes that occurred during the MSC and isolating the effect of each separate component on the atmosphere (Table 3.1).

Normally, the Atlantic Ocean provides a heat flux into the MedSea, and the MedSea is a substantial source of heat for the overlying atmosphere. During the MSC, the MedSea was isolated from the Atlantic in the sense that there was no substantial heat flux into the Mediterranean. The present barotropic (two-way) mass flux into the Mediterranean through the straits of Gibraltar is 0.8 Sv with a net inflow of 0.05 Sv to balance net evaporation in the MedSea (Lafuente et al., 2002). Assuming it took 100,000 years for the MedSea to evaporate, the net annual water flux into the MedSea must be less than 10^{-3} Sv (we assume the surface area of the MedSea is 2.5 x 10^{12} m^2 and its depth is 1000 m). If we assume it took just 10,000 years to evaporate, then a net water flux of 10^{-2} Sv is required into the MedSea. Since the ocean heat flux associated with a transport of 10^{-2} Sv is negligible, we use the term isolation in the sense that any Atlantic water heat flux to the MedSea is in-consequential. For all the experiments, the horizontal ocean heat transport (Q flux) into the MedSea is shut down to represent the isolation of the MedSea from strong ocean heat transport during the MSC. Q flux was computed from an uncoupled run forced with fixed SSTs, observed sea ice cover, and the MedSea converted to land. The missing heat flux is redistributed globally, though an adjustment procedure in which the Q fluxes are derived in order to balance the ocean heat budget at the fixed

SST values. The effect on the model climate of changing Q-flux itself is discussed in Chapter 3.

2.2 Boundary conditions

Trace gas concentrations, including atmospheric CO_2, are set to present-day levels based on alkenone-based estimates of the partial pressure of CO_2 in the atmosphere (pCO_2) (Pagani et al., 1999), the pressure difference between the ocean and atmosphere,that indicate pCO_2 values were above pre-industrial values during the late Messinian. We use the default CO_2 concentration in CAM, which is set to 350 ppm.

In our study, mountain topography was set to modern day elevations following Kuhlemann's (2007) paleogeographic maps. Kuhlemanns (2007) 8 Ma paleotopographic map of central Europe is comparable to Smith and Sandwell's (1997) present-day topographic map based on Geosat, ERS-1/2, and Topex/Poseidon altimeters. Although a substantial region of the Alps extended above 2000 m for the entire Miocene, rapid uplift beginning around 5 Ma brought about significant topographic changes in southern Europe (Kuhlemann, 2007). However, the orographic relief of the Alps is crudely represented at T42 resolution and elevations do not extend above 1500 m, with only 2 grid boxes extending above 750 m (Fig. 3.1).

Since only insignificant plate tectonic movements have occurred since the Tortonian (Ruddiman and Kutzbach (1989)), we followed the Francois *et al.* (2006) and Stepphun *et al.* (2006) studies and assumed a modern day land-sea distribution for our

Messinian runs. Most MSC modeling studies incorporate Tortonian ($\sim$ 8 Ma) paleo-geography, which overestimates changes in sub-basin area and volume (Meijer *et al.* (2004); Meijer and Krijgsman, 2005; Meijer, 2006; Stepphun et al., 2006). According to Meijer et al. (2004), Messinian geography would most likely be intermediate between the present day configuration and their reconstruction. Considering the crude representation of the land/ocean distribution at T42 resolution (46 grid points comprise the Mediterranean Sea), the incorporation of paleogeography is not expected to modify our results. Modern day vegetation is also used in this study, except when the MedSea was removed (refer to the UL and LL simulations).

Although the Greenland ice sheet did not form until the late Pliocene (near 2.37 Ma) (Shackleton et al., 1984), in order to minimally disturb the model and focus solely on changing MedSea boundary conditions we chose not to remove the Greenland ice sheet. Lunt et al. (2004) removed the Greenland ice sheet in a coupled climate model and found surface temperature anomalies to be localized and circulation changes that consist of decreased geopotential height over the North Atlantic and increased geopotential height throughout central Eurasia. This circulation response is similar to what we find when we lower the MedSea base level (Chapter 3).

2.3   Limitations in our Model Simulations

Our simulations are not perfect and we can expect further changes in the Messinian Mediterranean water budget if we included better physical representa-

tions. Evaporation increases with increasing temperatures, wind velocities and re-duced water salinities. It is important to note that in the real world, the Dead Sea doesn't evaporate completely because its increased salinity reduces the water vapor pressure at the surface of the sea (Raoult's Law), reducing evaporation. An extremely salty LS might have somewhat lower E-P than our results indicate, since this mechanism is not included in the model. However, double diffusion, which is not included in this model, may result in a positive feedback. Thermal diffusivity is much greater than salt diffusion. When thermal diffusion occurs, the salt particles become much denser than the medium and precipitate to the sea floor. This process occurred during the MSC when a large (1000-3500 m) layer of halite accumulated on the MedSea floor (Krijgsman and Meijer (2008)). The density of the deep MedSea would become higher than the surface, which would increase the stratification of the sea and weaker turbulent mixing. The surface of the MedSea, which would have a lower concentration of salt would heat up faster than if the salt concentration was distributed evenly. This results in a feedback that would accelerate evaporation. We also do not take into account the change in the volume of the MedSea. As the MedSea evaporates, the volume decreases. The smaller volume of water would receive the same amount of insolation, thus increasing the surface temperature of the sea and further increasing evaporation, resulting in a positive feedback loop.

2.4 Model Validation

2.4.0.1 Seasonal Cycle

Assuming the long-term mean of the MedSea water deficit is balanced by the water flux at the Gibraltar Strait gives the following equation:

$$G = E - P - R - B, \tag{2.1}$$

where E is evaporation, P is precipitation, R is runoff and B is the net flux from the Black Sea to the MedSea. The magnitude of net inflow from the Black Sea is small in comparison to precipitation and Atlantic water inflow: presently, the Black Sea contributes roughly 0.21 mm day^{-1} to the MedSea (Mariotti *et al.* (2002)). However, paleo-depth measurements suggest the Black Sea also experienced a substantial drop in sea level (Bartol and Govers (2009); Popescu *et al.* (2006); Gillet *et al.* (2007)), which further exacerbated the water deficit during the MSC. Assuming an average basin depth of 2,500 m, and current rates of P, E and B, the MedSea would evaporate in approximately 5,000 years. Since one evaporative draw down would not account for the massive salt layer (Hsu *et al.* (1973)), several studies have suggested the MedSea went through several cycles of desiccation and refilling (Meijer and Krijgsman (2005)). Conversely, since a closed MedSea would evaporate quickly, Roveri *et al.* (2001) suggests desiccation and flooding episodes were not externally (orbitally) forced. The evolution of the Messinian desiccation depends critically on the freshwater budget since MedSea level is highly dependent on the freshwater budget when isolated (G=B=0).

In Chapter 3 we discuss the impact of altering the horizontal heat transport (Q flux) on global climate. We can hypothesize that in the absence of Q flux, an isolated MedSea might be cooler and evaporate less. To examine this further we compare the seasonal cycle of evaporation and precipitation in our control (US), a CAM-SOM control run (Cntl) and climatology based on 1979-1999 shown in Mariotti *et al.* (2002)) (referred to as M02) (figure 2.1). In Mariotti *et al.* (2002), precipitation is from the Climate Prediction Center Merged Analysis of Precipitation (CMAP) (Xie and Arkin (1996)) and evaporation is from the University of Wisconsin–Milwaukee (UWM) Comprehensive Ocean–Atmosphere Data Set (COADS) (da Silva *et al.* (1994)). MedSea averages of the hydrological components are calculated using Gaussian weights over the region 30°to 46°N and 6°W to 37°E. The standard deviation (shaded gray) is shown for our US simulation. This shows large variability in the seasonal cycle of MedSea precipitation, especially in the summer and fall. Figure 2.1 shows that MedSea evaporation in the Cntl run agrees well with M02 in the winter. Throughout the rest of the year, evaporation possesses the same cycle but has a larger magnitude than M02. Precipitation, on the other hand, is in better agreement with M02 during the last half of the year and deviates from M02 estimates during the winter and spring. Eliminating the Qflux into the MedSea in our US run leads to a reduction in evaporation and precipitation compared to M02 (4.3). Our US simulation shows greater amplitude in the seasonal cycle of evaporation with a strong minimum persisting from the winter through the spring and large maximum during the late summer. In our US simulation, precipitation is reduced throughout the year and reaches a minimum approximately three months after the evaporation

minimum. The minimum in E-P corresponds to the minimum in evaporation and occurs between February and March. Greater evaporation from July to September is associated with more rain, and thus little change in E-P.

The annual mean freshwater deficit (E-P-R) of the US and LS simulations are much higher than modern estimates given in M02 (table 4.3). Our control (US) MedSea water deficit of 2.16 mm day^{-1} is 58% higher than the modern water deficit in M02 (1.37 mm day^{-1}), while our LS water deficit value of 2.33 mm day^{-1} is 70% higher than current estimates. Comparing E-P-R values in US_P- and US_P+ to US gives a 31% decrease and 7% increase in the freshwater budget, respectively. The level of the MedSea has the largest effect on the freshwater deficit at precession minimum. Reduced MedSea level increases evaporation by 7% and reduces precipitation by 14% under P- orbital forcing, increasing the freshwater deficit by 28%. The geological record shows that during past periods of an intense North African monsoon (at P-), the MedSea water deficit is reduced and deep-water formation is inhibited (Nolet and Corliss (1990)).

Comparing our data to the current climate shows, that the CAM-SOM (Cntl) simulation has a good representation of the seasonal variability of the MedSea water budget parameters. However, eliminating the heat flux into the MedSea results in a significant and substantial departure from the current climate.

2.5 Figures
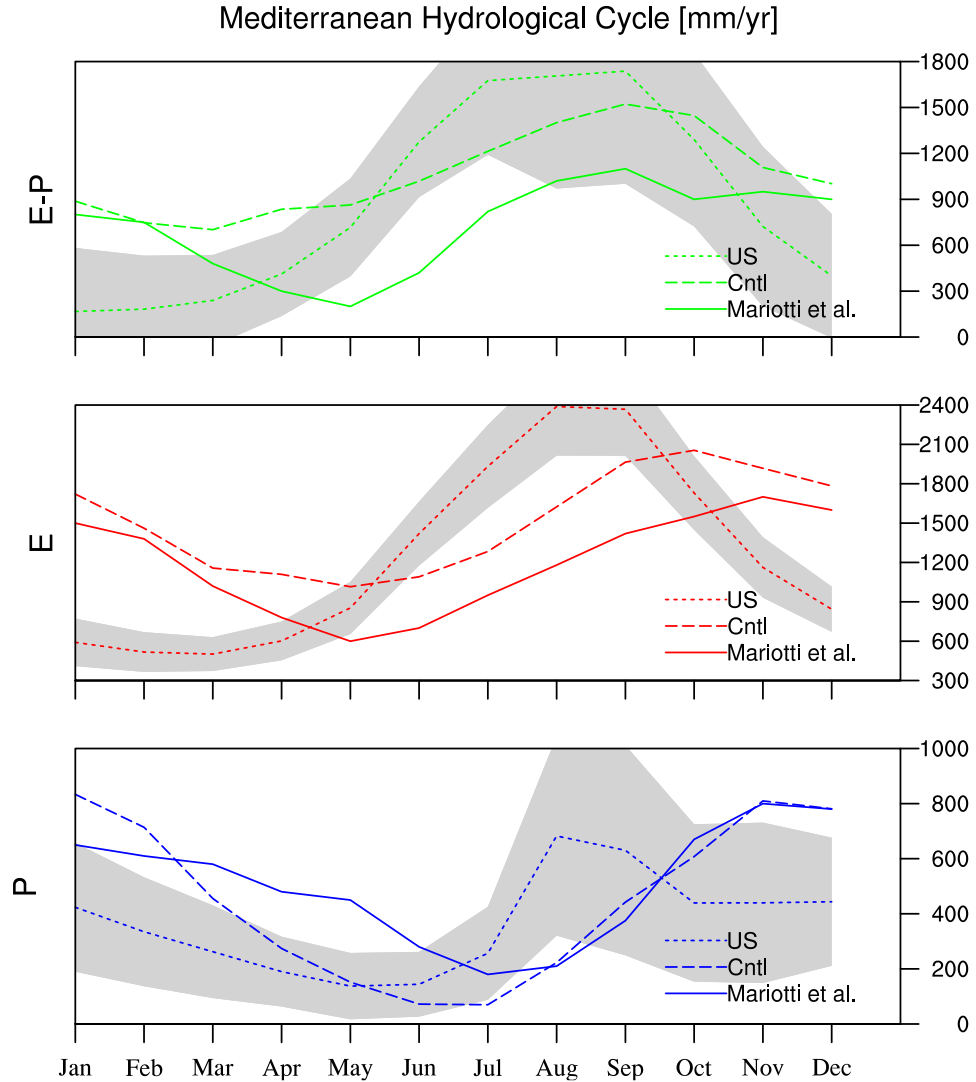
Figure 2.1: Annual cycle of evaporation-precipitation (E-P) (top), evaporation (middle) and precipitation (bottom) averaged over the Mediterranean Sea (6°W-37°E, 30°-46°N) for our control US (dotted), a CAM-SOM control run with no Q-flux modification (Cntl) (dashed), and present day estimates (Mariotti *et al.* (2002) (solid). Presend day esitmates of precipitation are from the CMAP dataset and evaporation from the UWM/COADS. This data is presented in Mariotti *et al.* (2002). The standard deviation calculated over the last 30 years of model simulation and is shown for the US simulation.

Chapter 3

Desiccation Experiments

3.1 Abstract

Roughly six million years ago, tectonic movements isolated the Mediterranean Sea (MS) from the Atlantic Ocean, an event known as the Messinian Salinity Crisis (MSC). Subsequent evaporative drawdown of the MS resulted in a subaerial depression with a depth between 1500 and 2500 m. In this study, five simulations are run using the National Center for Atmospheric Research (NCAR) Community Atmosphere Model version 3 (CAM3) configured with the slab ocean model. Three simulations have been performed to test the climate impacts to desiccation and to changing the MS base level. In this study, the MS base level is reduced 750 m in the Half Land simulation (HL), and 1500 m in the Lowered Sea (LS) and Lowered Land (LL) simulations. The HL and LL simulations differ from the LS in that the surface is converted to land, representing the complete desiccation of the MS. The substantial MS depression generates planetary-scale atmospheric waves responsible for significant climate effects throughout the Northern Hemisphere. A notable deepening of the Aleutian Low and a significant equatorward shift in the Atlantic jet stream are evident. In DJF, vertical ascent at the northern margin of the MS results in a 1.5-2.5 mm day-1 precipitation anomaly in the LS run over the Alps, consistent with proxy data. Annual mean area averaged MS evaporation is slightly

higher than control conditions. Except when salinity is a substantial barrier to evaporation, our results suggest that a partially filled basin cannot exist in equilibrium and the MS must either be partly connected to the Atlantic Ocean or completely desiccated. Base level lowering, which alters the water budget, must be taken into account when considering the freshwater budget during the MSC.

3.2   Introduction

Changes in global sea level, orbital forcing, climate change (Hodell et al., 2001; Warny et al., 2003), and the orogenic uplift (Krijgsman *et al.* (1999);Duggen *et al.* (2003)) have all been cited as isolating MedSea from the Atlantic Ocean during the MSC (Seidenkrantz et al., 2000; Warny et al., 2003). Krijgsman et al. (1999b; 2001) used astronomical dating methods to deduce that plate tectonics triggered the MSC by severing the connection between the MedSea and Atlantic Ocean at 5.96 Ma. Benthic foraminifera and stable isotope data show that vertical uplift as early as the latest Tortonian (approximately 11 to 7 Ma) began restricting the Rifian Corridor in Northern Africa, one of several gateways (the others being the Rifian corridors, which closed at different times during the Late Miocene (Betzler et al., 2006; Martin et al., 2001)) that existed between the Mediterranean and the Atlantic prior to the onset of the MSC (Seidenkrantz et al., 2000; Kouwenhoven et al., 2003). Additionally, pollen data analysis confirms that climate variations did not initiate the MSC (Warny et al., 2003; Fauquette et al., 2006). However, a lowering of global sea level resulting from glaciation may have contributed to further isolation of the

MedSea by modulating the water level at the existing straits (Adams et al., 1977; Aharon et al., 1993; Hodell et al., 1986). The benthic $\delta^{18}O$ signal, a commonly used paleoclimate indicator of glacio-eustatic sea-level changes, suggests that ice formation prior to the MSC led to a decrease in global sea level of nearly 70 m (Hodell et al., 1994; Hodell et al., 2001; Clauzon et al., 1996).

Here we summarize the aspects of the history of the Messinian desiccation most relevant to our simulations. Please refer to Hilgen et al. (2007) and CIESM (2008) for a detailed history of Messinian events in the Mediterranean Sea. Isolation from the Atlantic Ocean during the MSC in combination with a negative MedSea annual water budget led to the deposition of a thick layer of evaporites (Krijgsman et al, 1999a). The "Lower Evaporite" unit, consisting of gypsum anhydrite and dolomite rocks, was deposited between 5.96 and 5.6 Ma (CIESM, 2008). Krijgsman et al. (1999a) suggests the massive layer of halite, potash and magnesium salts was deposited between the "Lower Evaporite" and "Upper Evaporite" units. Anhydrite and magnesium salts are characteristic of extremely hot (greater than 35°C), dry environments (Hsu, 1972; Rouchy and Caruso, 2006). Our Lowered Land simulation (see Section 3.3) represents the "Messinian Gap", when the combined effects of tectonic uplift and two peak glacial stages resulted in the isolation of the MedSea and the final stage of a major drawdown roughly 5.6-5.55 Ma (CIESM, 2008).

The "Upper Evaporite" unit and Lago-Mare facies were deposited between $\sim$ 5.6 and 5.33 Ma. The Upper Evaporite unit, consisting of gypsum and marl, marks a change in the MedSea hydrological budget influenced by precession-driven climate changes (Krijgsman et al., 2001). Shallow brine pools formed more than 1000 m

below world sea level (Roveri et al., 2006). According to Blanc (2006), the "Upper Evaporites" were deposited in a closed basin in which Atlantic water inflow is suppressed, the eastern MedSea basin surface was reduced ~ 1700 m, and the western MedSea basin surface was reduced ~ 1500 m. Reduced marine inputs and increased freshwater inputs brought about Lago-Mare conditions in the latest stage of the MSC (Rouchy et al., 2001). Our Lowered Sea simulation is meant to represent this latest phase of the MSC and tests the sensitivity of the climate impacts to sea level, a very important consideration in determining under what conditions a brackish Mediterranean (as in the Lago-Mare) could be maintained.

3.3 Experimental design

While previous AGCM modeling studies of the MSC have used paleo-physiography (Gladstone *et al.* (2007)), they did not examine the impact of desiccation and the role of Mediterranean Sea level on the atmosphere. We believe our efforts are the first to detail both the regional and global effects due to changes in the MedSea level during the MSC. Five experiments were performed using the NCAR CAM3-SOM to simulate the MedSea base level changes that occurred during the MSC and isolating the effect of each separate component on the atmosphere (Table 3.1).

In our control upper sea (US) run, we simulate the impact of isolating the MedSea from the Atlantic Ocean. The sea level and surface characteristics of the MedSea are unchanged but the new Q flux is implemented. All other runs are compared to the US run, so that the climate changes due to the changes in sea level and surface type

26

are isolated, and the Q flux alteration does not contribute to the modeled climate changes. A sensitivity test is conducted to investigate the effect of changing land surface characteristics over the MedSea. In this upper land (UL) experiment (which does not represent any real state of the MedSea during the Messinian), we convert the MedSea to land but the terrain remains at the present day sea level. Changing the land surfaces causes changes in the fluxes of heat, momentum and water to the overlying atmosphere, the impact of which is included in our simulations (Oleson et al., 2004). At T42 resolution only three grid points over the MedSea are considered to be completely ocean and the other 34 Mediterranean grid boxes are partial land-ocean points (land fraction is less than 0.6). In order to remove the Mediterranean Sea these ocean and partial ocean-land boxes are converted to land. In order to account for the change from ocean to land, soil color, texture and plant characteristics were added. These values were taken from a grid box over the Saharan Desert at 8°E, 18°N. We assumed that the land characteristics of a desiccated basin would be similar to a point representing a desert. The UL run allows us to examine the atmospheric response to the thermal forcing due to surface characteristic changes, without the topographic changes accompanying the MSC.

In the lowered sea (LS) experiment, the MedSea level is reduced up to a maximum of 1500 m, a conservative estimate of sea level fall during the MSC and consistent with paleoriver profiles in Gargani (2004), and water remains in the basin. The elevation was lowered as a linear function of land fraction in each grid box. The deepest point is located in the eastern sub-basin. Much of the surface of the basin is between 700 m to 1400 m below sea level with only three grid points in the center

27

of the MedSea that reach a maximum depth of 1500 m. This was done to examine the effect of sea level fall on the climate and allows us to examine the atmospheric response to purely orographic forcing.

In the lowered land (LL) experiment, the surface of the MedSea is converted to land and is lowered in the same manner as the LS simulation. Surface characteristics are the same as the land sensitivity (UL) run. In the LL run the basin is fully desiccated (no water remains in the basin). This experiment examines the effect of complete evaporation and sea level fall in the MedSea. A half land (HL) simulation is also conducted in the same manner as the LL run, except that the surface is lowered only 750 m.

There are several reasons to keep our simulations simple. First, knowledge of appropriate Messinian boundary conditions is not perfect. Ongoing tectonic processes throughout this time make constructing paleogeography complicated. Focusing on the atmospheric response allows us to concentrate computational resources on resolution and running multiple scenarios. While other groups have modeled the Late Miocene climate, most have focused on the Tortonian (11.6-7.2 Ma) (Francois *et al.* (2006), Micheels *et al.* (2007)), or did not account for the reduction in MedSea level or desiccaiton (Favre *et al.* (2007), Gladstone *et al.* (2007)). Our study is unique in that it takes into account the reduction in Mediterranean Sea level and allows SSTs to respond to the associated atmospheric changes.

3.4   Results

Simulations were integrated for 70 years. Climatological annual and monthly means are calculated over the last 30 years of the model runs except for the HL simulation, which was integrated for 55 years and means were computed over the last 15 years of the model run. The climatological monthly means were then used to calculate monthly climatological standard deviations. A student's t-test was performed to determine where the experiments were statistically different from the control run and values that were statistically different at the 0.05 or less critical level of significance are shown. Changing the horizontal heat transport in the ocean, Q flux, has several important implications for global climate in our simulations (discussed further in Section 3.4.3), therefore we discuss anomalies between the four experiments (UL, HL, LL, and LS) and our control simulation (US), rather than a true control run (without implementing the new Q flux). This ensures that any artificial changes due to the implemented Q flux are identical in all simulations and the responses shown are due to thermal and orographic effects of an altered MedSea. The modeled atmospheric response to topographic forcing may vary as model resolution and momentum transport schemes vary. We plan future experiments at higher spatial resolution that will help to clarify the extent to which our results depend on the specific model used and to comparing our results with other modeling groups using different climate models.

Lowering the surface topography of the Mediterranean Sea results in an 80-hPa (Fig. 3.1B) and 160-hPa (Fig. 3.1C and 3.1D) annual mean surface pressure anomaly over

the Mediterranean basin relative to our control. This pressure change is slightly lower than the pressure change expected from the hypsometric equation. Assuming heights are fixed above 500 h-Pa, potential temperature, θ, is conserved following the flow, and parcels near the surface flow down to the bottom of the basin conserving θ, Z is an array from -1500 m to 5500 m, and $\theta = T_0 + (Z_i + 1500)/7000 * T_1$, where $T_1 = 20$ K and is an estimate of the increase in θ from the surface to 500-hPa and $T_0 = 285$ K. A 1500 m reduction in surface elevation results in a 186-hPa increase in surface pressure.

3.4.1   Lowered Sea results

3.4.1.1   Temperature response

Figure 3.2 shows the winter (December-February) (left) and summer (June-August) (right) temperature anomaly for the northern hemisphere. Lowering the sea level of the MedSea leads to a clear warming of the Mediterranean basin (Fig. 3.2E–H). Using back of the envelope type calculations and assuming an adiabatic lapse rate from sea level down to the lowered Mediterranean predicts a warming of 14 K. We expect the warming to be somewhat less than this, since the terrestrial lapse rate is strongly governed by the surface energy budget, which is not strongly height-dependent (Meyer, 1992).

The area averaged MedSea (defined as: 6°W-37°E, 30°–46°N) surface temperature (TS) anomaly in DJF is warmest when water is retained in the basin (LS). In the LS basin, the surface temperature warms 4.4 K in DJF and 3.6 K in JJA. We expect

the LS basin to be warmer than the LL basin because of the higher heat capacity of water that should allow the basin to retain the heat that was gained during the summer.

Figure 3.2 shows that while thermal forcing lead to a large warming in the Mediterranean region and cooling in the Gulf of Alaska (Figs. 3.2A and 3.2B), orographic forcing results in a stronger global response (Figs. 3.2E-3.2H). The planetary wave response to orographic forcing is stronger over the Eurasian continent during the winter and leads to a larger area of cooling in the North Pacific during the summer. Figure 3.3 shows zonal (east-west) and vertical cross sections of summer and winter temperature anomalies (shaded) and wind anomalies (vectors) averaged meridionally from 30°to 40°N. During the winter, advection of warm, moist air into India is orographically lifted near the Himalayas resulting in anomalous precipitation and upper level divergence near 75°N. At upper levels, the westward flowing branch of this diverging air converges with upper level Westerlies over the MedSea. There is greater ascent in the middle and upper troposphere over the MedSea when water remains in the basin (Fig. 3.3E) compared to when the basin is completely desiccated (LL) (Fig. 3.3C).

3.4.1.2 Circulation and atmospheric water balance

In our modeling study, topographically and thermally induced changes in regional wind results in the transport of moisture-laden air into southern Europe (Figs. 3.4C-3.4F). Figure 3.4 shows seasonal anomalies in Omega (vertical velocity) (con-

toured) and wind anomalies (vectors) throughout the Mediterranean Sea, Europe, Northern Africa, and Southern Eurasia.

In DJF, the wind field shows anomalous cyclonic (counterclockwise) rotation at the surface, which is representative of low atmospheric pressure. In contrast to the simulations where the height field is unchanged (UL) and the winds over the MedSea are primarily zonal (flowing from east to west), lowering the height field (LS and LL runs) generates strong southerly flow over the central and eastern MedSea. The vertical velocity field shows descent at the northwestern edge of the MedSea where the atmospheric flow enters the basin and ascent at the northeastern edge of the MedSea where the wind exits the basin (Fig. 3.4C and 3.4F).

Changes in the wind pattern are consistent with changes in the hydrological cycle (Fig. 3.5). Figure 3.5 is plotted in the same fashion as Fig. 3.4 but shows total precipitation anomalies (convective and large scale precipitation). A significant increase in precipitation occurs along the northeastern margin of the MedSea in the LS simulation (Fig. 3.5E). Enhanced precipitation in this area is consistent with enhanced southerly winds that push air up the slope of the northern edge of the basin. In DJF a topographically forced precipitation anomaly of 1.5-2.5 mm day^{-1} extending from Italy to Bulgaria occurs in the LS simulation (Fig. 3.5E). This is more than a 50% relative increase in precipitation.

The presence of both warm temperatures and abundant water in our LS simulation results in a higher total precipitable water (vertically integrated throughout the entire atmosphere) over the MedSea compared to the LL simulation (Fig. 3.6). Precipitable water is the amount of water vapor in a vertical column extending from the

surface to the top of the atmosphere. Higher precipitable water may supply more energy to the atmosphere and thus generate and sustain weather disturbances. Precipitation and latent heat changes not only depend on precipitable water but also on topographically induced changes in vertical velocity. This additional energy is only liberated when upward motion or radiative cooling results in condensation. A notable and substantial DJF relative precipitation increase occurs over eastern North Africa ($> 100\%$) in the LS simulation and India ($> 50\%$) in both the LS and LL simulations (Fig. 3.5C and 3.5E).

The impact of the desiccation of the MedSea on the annual atmospheric water budget integrated over the Mediterranean Sea (6°W-37°E, 30°N-46°N) is shown in Table 3.2. Our LS simulation results in an annual MedSea averaged E-P of 2.57 mm day^{-1} compared to our control climate E-P of 2.32 mm day^{-1}. Figure 3.7 shows the percent difference in annual mean water budget components (P, E and E-P) for the UL, LL and LS simulations. In our LS simulation, evaporation increases by 5 to 25% from east to west (Fig. 3.7H) while E-P transitions from negative values in the northeast to positive values in the southwest (Fig. 3.7I). If salinity is not a substantial barrier to evaporation, the basin is unlikely to refill completely, since a substantially filled basin (as in the LS simulation) increases evaporation (3.48 mm day^{-1}) compared to control conditions (3.35 mm day^{-1}) preventing complete refilling until some larger climatic event occurs, or until a tectonic event reopens the connection with the Mediterranean. It is important to note that in the real world, the Dead Sea doesn't evaporate completely because its increased salinity reduces the equilibrium vapor pressure of water over it (Raoult's Law), reducing evaporation. An extremely salty

LS might have somewhat lower E-P than our results indicate, since this mechanism is not included in the model.

3.4.1.3   Planetary wave response

Figures 3.8 and 3.9 show the winter (December-February) (left) and summer (June-August) (right) geopotential height (Z) anomaly for the northern hemisphere. Monthly averages of geopotential height show maximum variance near the semi-permanent lows and explain a substantial portion of the wintertime atmospheric circulation. A difference in the average geopotential height field indicates variability in the circulation and therefore changes in the paths that storms tend to follow. Large changes in the boundary conditions of the MedSea produce an orographically forced planetary wave response that results in changes in both the height field (Figs. 3.8 and 3.9) and temperature field (Fig. 3.2) throughout the Northern Hemisphere. Figures 8 and 9 display the geopotential height response for all three experiments (UL, LL and LS) at 850-hPa and 300-hPa, respectively. The development of a wave train that propagates throughout the Northern Hemisphere is apparent in the 300-hPa maps of geopotential height anomalies. A significant deepening of the geopotential height field over the Gulf of Alaska is seen in both the LS and complete desiccation scenarios (Figs. 3.9E and 3.9G). The Aleutian and Icelandic lows are both semipermanent lows through which synoptic scale low-pressure systems frequently pass and intensify (Zhu et al., 2007). These centers have significant effects on the atmospheric circulation in the Northern Hemisphere.

Climatological winter anomalies in both the LS and complete desiccation (LL) simulations result in a barotropic response over the Mediterranean Region with vertically stacked low height anomalies from the surface to the upper troposphere. Low heights also extend from the lowered basins (LS and LL) across the North Atlantic reaching the North American continent. Higher heights occur downstream from the MedSea over Russia and Eastern Europe. This dipole pattern produces strong southerly winds at the surface (Figs. 3.4C and 3.4E).

Changes in precipitation can be related to the large-scale stationary wave response and subsequent variations in storm tracks. Eddy Kinetic Energy and the variance of meridional wind at 250-hPa, a good diagnostic for storminess (Lau, 1988; Chang, 2003), were examined to determine if changes in the storm track dynamics occurred. Figure 3.10 shows the variance of the 250-hPa meridional wind component for the control US run (Fig. 3.10A) and the anomalies for the LS (Fig. 3.10B), UL (Fig. 3.10C) and LL (Fig. 3.10D) simulations. The meridional wind variance shows a moderate and significant equatorward shift near the entrance region of the MedSea (Figs. 3.10B and 3.10D). A more intense remote response in the LS winter compared to the LL winter is related to a more zonal (W-E) storm track across the Atlantic basin with intensified storm energetics at the entrance region of the MedSea and decreased atmospheric stability over the basin. We can deduce that the changes in precipitation along the storm track were related to the presence of anomalously high total column precipitable water and possibly to a small shift in storm energetics.

3.4.2 Lowered Land results

3.4.2.1 Temperature response

The area averaged surface temperature of the LL basin warms 2.7 K in DJF and 11.1 K in JJA. In JJA, the surface of the lowered MedSea is warmest when water is removed (LL, HL and UL). The increased warming in the LL run compared to the LS is due to the smaller surface heat capacity of land compared to water. Locally, surface heating results in a 10-hPa decrease in surface pressure over the lowered basin (not shown).

Anomalously warm air extends up to 700-hPa above the MedSea (Figs. 3.3D and 3.3F) leading to increased atmospheric instability, which perturbs the storm track and leads to a strong global response in the geopotential height field (Figs. 3.8F and 3.8H and Figs. 3.9F and 3.9H).

The vertical cross sections (Fig. 3.3) show that during the winter the overlying atmosphere experiences similar warming when the level of the MedSea is lowered (LL and LS) and is independent of the surface characteristics. In the winter, the atmosphere drives temperature changes at the surface because solar forcing is weak. In the summer, when solar forcing of diurnal variability is much larger, the surface forces temperature changes in the atmosphere and the temperature response of the overlying atmosphere depends on the surface heat capacity. This allows the atmosphere above the LL to warm much more than the atmosphere above the LS.

3.4.2.2 Circulation and atmospheric water balance

In JJA, the development of cyclonic rotation to the north and anticyclonic rotation to the southeast of the MedSea (Figs. 3.4D and 3.4F) results in a southwesterly flow across the lowered MedSea. This air entrains moisture and transports warm, humid air into southeastern Europe and North Africa (Figs. 3.2D and 3.2F). Since the absolute humidity, or vapor density, of warmer air is higher than for cooler air the warmer air contains more moisture (Fig. 3.6F). Zonal flow subsides as it enters the basin in the west and rises as it exits the basin in the east (Figs. 3.3D and 3.3F) resulting in a 0.5–1 mm day^{-1} precipitation anomaly over the Alpine region (Fig. 3.5C). Typically, the Mediterranean climate consists of warm, dry summers, however, moisture is released when the air is orographically lifted at the northern margin of the basin (Fig. 3.5F). This is a 10% relative increase in precipitation. JJA precipitation is enhanced by 0.5-1.5 mm day^{-1}, more than a 100% increase compared to the control simulation, near modern Greece (Fig. 3.5F). Large subsidence occurs to the east of the basin over the Arabian Peninsula.

Diminished moisture inhibits precipitation and leads to a sufficient reduction in annually averaged MedSea evaporation (0.31 mm day^{-1} for the LL runs) (Figs. 3.7B and 3.7E) so that the E-P budget of the basin is brought very close to balance. The integrated Mediterranean watershed E-P is reduced to -0.03 mm day^{-1} from 2.32 mm day^{-1} under control conditions (Table 3.2). Since the system is almost to equilibrium a seasonal shallow sea might exist, becoming deeper in wet years and shallower in dry years. Our results have neglected the ability of salinity to reduce

the vapor pressure over a very briny sea, which might allow for a permanent shallow sea (as it currently does for the Dead Sea).

3.4.3   Impact of changing Q flux

In order to isolate the MedSea from the Atlantic Ocean the horizontal heat transport in the ocean, Q flux, was altered (see Section 3.3). This change was found to have several implications for global climate. Figures 3.11 and 3.12 shows the differences between our simulations (US, UL, LS, and LL) and a CAM3-SOM control simulation (CNTL) run at the same resolution (T42) but without a change in Q flux (the CAM3-SOM control simulation (CNTL) run at the same resolution (T42) but without a change in Q flux (the CAM-SOM control simulation (CNTL) (available online at: http://www.cgd.ucar.edu/ccr/CPT/climatology.html) was integrated for 40 years and averages were taken over the last 10 years of model simulation).

3.4.3.1   Temperature

Figure 3.11 shows differences in the TS field. The upper four panels in Fig. 3.11 show the differences between the runs in which the elevation of the MedSea was unchanged (US and UL) and the control (CNTL). The lower six panels in Fig. 3.11 show the differences between the runs in which we lowered the elevation of the MedSea (HL, LL and LS) and the control (CNTL). Differences between the upper four and lower six panels are due to the lowering and/or evaporation of the MedSea. When the SOM is allowed to adjust, heat fluxes arise in the atmosphere that tends

to move the SST slightly away from the values to which the Q fluxes adjusted. The new oceanic heat flux scheme alters the SST pattern in the Atlantic basin, since SST anomalies are consistent among all panels. Removing the heat flux supplied to the MedSea from the Atlantic Ocean results in cooler Mediterranean SSTs during the winter and a slight warming during the summer (Figs. 3.11A and 3.11B). In DJF cooling in the MedSea is reduced in the LL and LS simulations (Figs. 3.11G and 3.11I) due to adiabatic heating of air parcels as they encounter the lowered basin (Figs. 3.11E, 3.11G, and 3.11I). A significant warming of the MedSea occurs during the summer when the sea level is lowered (LS) (Fig. 3.11J) but is more robust when the water is removed from the MedSea (UL, HL and LL) (Figs. 3.11D, 3.11F, and 3.11H). Thermal and orographic forcing during the summer results in cooler SSTs off the Aleutian Islands (Figs. 3.11D, 3.11H and 3.11J) and warming to the northeast of the MedSea (Figs. 3.11F, 3.11H and 3.11J).

3.4.3.2 Geopotential height

Figure 3.12 shows the differences in geopotential height between our simulations and the CNTL run. While the implemented Q flux results in lowered geopotential heights in the tropics, northeast of the MedSea in DJF (Fig. 3.12A), and a narrow region in the far North Pacific in JJA (Fig. 3.12B), topographic and thermal forcing due to changing the MedSea elevation and surface type result in the remote middle and high latitude geopotential height response as evident in the lower four panels (Figs. 3.12G–J). We note that DJF geopotential heights over the Gulf of

Alaska in DJF are lowered with respect to the CNTL run, but are not statistically significant at the 95% level (Fig. 3.12G and 3.12I).

3.5   Discussion

Our modeling framework tests the impact of complete desiccation and lowered MedSea level while keeping other factors constant. A schematic illustration of the global climate effects of the MSC is shown in Fig. 3.13. The simulated climate implications of the MSC are not confined to the Mediterranean region, but instead propagate globally through variations in the storm track. A global barotropic downstream response occurs throughout the Northern Hemisphere during both seasons when the elevation of the MedSea is lowered (LS and LL) but is strongest during the winter in our LS simulation. This planetary wave response propagates downstream and initiates global changes in the height field. In the LS and LL winter simulations a modest but significant equatorward shift in the variance of the meridional wind, a diagnostic of storm track intensity is evident. The large-scale stationary wave response leads to strong temperature anomalies in both winter and summer. Annually, the LS and complete desiccation simulations result in a notable deepening (300 hPa) of the Aleutian Low. The stationary wave response to topography tends to be only weakly non-linear, so that our results, specifically the remote response, are likely not strongly sensitive to the heights of the Mediterranean mountains.

3.5.1   Temperature

3.5.1.1   Local response

Lowering the MedSea level led to a 160-hPa decrease in the annual surface pressure relative to the control run. Strong adiabatic warming occurred as air rushed into the deep basin. During the summer, our simulation of the complete desiccation of the MedSea resulted in the largest warming. In JJA, the TS over the basin warmed by more than 10 K. In DJF, the LS and complete desiccation simulations showed similar warming of 6 K.

Fauquette et al. (2006) gives annual mean precipitation and annual mean temperature estimates based on pollen reconstructions at various sites along the MedSea coastline corresponding to the MSC. Comparing proxy data to our model results is difficult since pollen data is based on individual sites, while modeled data is averaged over a grid box on the order of $2x10^5$km^2. Fauquette et al.'s (2006) proxy data for the MSC period corresponds to the Lower Evaporite phase in all sites except the Maccarone and Torre Sterpi, which correspond to the Upper Evaporite phase. The LS simulation gives estimates of annual mean temperatures that are within the range of proxy data at all locations except in Northern Italy, which is too cool in the LS run compared to Fauquette et al. (2006) but consistent with cooler conditions found in Bertini (2006). The LL simulation is too warm ($\sim$3 K) near the Maccarone and Eraclea Minoa sites. In all of our simulations (LL, LS, and US), temperatures near Torre Sterpi are between 5–10 K cooler than those suggested by proxy data.

3.5.1.2 Remote response

During the Miocene, proxy data indicates warmer (compared to present) higher latitudes and similar temperatures in the tropics reducing the meridional temperature gradient (Dutton and Barron, 1997). Faunal and oxygen isotope data suggest cooler conditions during the Messinian compared to the middle and early Miocene. Moreover, hiatuses within Messinian aged deep-sea sections correspond to major climatic cooling in the North Pacific (Barron and Keller, 1982) and northwestern Canada and Alaska (White et al., 1996).

Our results show cooling of high latitude ocean regions. There is support for this in the geological record. Strong cooling over the North Pacific, specifically off the coast of the Aleutian Islands, occurs throughout the year in the LS and complete desiccation scenarios. Lowering the sea level of the MedSea results in an annual cooling of more than 0.5 K in the North Pacific. While this cooling is not strong enough to result in glaciations it can lead to a continuing trend toward high latitude glaciation. Cooling in the Gulf of Alaska is in accord with evidence of initial tidewater glaciation in the Yakataga Formation (far North Pacific) between 5.0 and 6.7 Ma (Lagoe et al., 1993) and IRD beginning between 5.5 to 6 Ma in the Kurile/Kamchatka region (Site 881, $\sim$ 162°E, 47°N) (Krissek, 1995). It is interesting that the development of IRD is coincident with restriction of Atlantic water into the MedSea. Strong and statistically significant cooling of the North Atlantic SSTs occurs in the LS and complete desiccation scenarios, but may be related to changes in Q flux. Utilizing a coupled model may result in important feedbacks in the thermohaline circulation as

it is expected the salinity of the Atlantic Ocean will be reduced due to the absence of Mediterranean outflow water. Lower salinity and cooler waters in the North Atlantic would reduce the overturning circulation and lead to important consequences for global climate.

3.5.2 Water Budget

3.5.2.1 Mediterranean Sea

In our LS simulation, we concluded that changes in the local zonal wind pattern and higher precipitable water values in a partially desiccated basin led to a large positive anomaly in precipitation that extends from the Alps eastward into Bulgaria during boreal winter. The precipitation anomaly over the Alps is greater than 1.5-2.5 mm day^{-1}, a 50% increase compared to the US simulation. This anomaly is substantial when compared to climatological area averaged precipitation, which varies between 1.4–4.8 mm day^{-1} during the winter in this region (Mariotti et al., 2002). Willett et al. (2006) suggested that wetter conditions during the Lago-Mare period led to the abrupt cessation of outward growth in the Alps due to increased weathering. Our results suggest that a switch in the zonal winds due to the lowered elevation of the MedSea during the Messinian coupled with the availability of water could allow air parcels to entrain water as they move across the lowered basin. This water is precipitated as air is topographically lifted at the northeastern edge of the Mediterranean Sea. The transport of water from the MedSea to the Alps during the Lago-Mare period may have led to increased weathering. Rouchy and Caruso

43

(2006) state that the transition to the Lago-Mare period occurred when a wetter climate existed near the mountainous regions along the coast of the MedSea. Our precipitation response in our LS simulation tends to support these conclusions and correlates well with evidence suggesting a relatively moist central and northern Italy during the Messinian stage (Bertini, 1994).

Mean annual precipitation estimates in our control (US) simulation are substantially lower than Fauquette et al.'s (2006) estimates and are most likely a result of the modified Q fluxes. The LS and LL simulations are too dry compared to proxy data with the exception of Northern Italy and the Gibraltar Strait where the LS climate is humid, consistent with proxy evidence (Fauquette et al., 2006; Bertini, 1994; Rouchy and Caruso, 2006).

3.5.2.2 North Africa

Griffin (2002) suggests periods of insolation minimum in combination with the poleward migration of Africa led to the northward shift of monsoon and desert zones and speculates the drawdown of the MedSea intensified the wet phase in North Africa, which consequently supplied more moisture to the MedSea and allowed for the transition to the Upper Evaporite layer. An increase in precipitation occurs over northeastern Africa, an area of low-level convergence, in DJF in the LS simulation. While the magnitude is small (< 0.5 mm day^{-1}) it comprises more than a 100% relative increase in precipitation. Lago Mare conditions may have also resulted from the initiation of the North African monsoon during precession minimum conditions,

which would have supplied the Mediterranean region with greater precipitation and runoff, as suggested by Griffin (2002).

3.6   Concluding remarks

There is still uncertainty regarding the formation of halite on the bottom of the MedSea during the MSC. Box model studies (Meijer, 2006) and budget calculations (Krijgsman and Meijer, 2008) have been performed to determine the water budget and strait exchange necessary to reach saturation. Meijer and Krijgsman (2005) found that the degree of saturation in the MedSea is critically dependent on the freshwater budget. However, in the absence of any clear alternative, previous studies of water and salt budgets have used present day hydrological fluxes (Meijer and Krijgsman, 2005; Meijer, 2006). Meijer and Tuenter (2007) found that precession minimum reduces the MedSea net water loss (E-P-R) by 20% in a coupled model of intermediate complexity. In our LS simulation, which uses present day orbital forcing, area averaged MedSea evaporation is slightly higher than control conditions. Moreover, the area averaged MedSea precipitation is equivalent to the US simulation. Unless salinity is a substantial barrier to evaporation, our results suggest that a partially filled basin cannot exist since a partially filled basin increases evaporation compared to the control. The MedSea must either be partly connected to the Atlantic Ocean (and filled to sea level) or completely desiccated, or else in rapid transition from one state to the other.

Eddy contribution to the zonal mean moisture, heat and momentum budget is signif-

icant at 30°N. At this latitude there is a substantial increase in meridional stationary eddy moisture, momentum and heat flux when the Mediterranean basin is a desert. Although the elimination of Mediterranean Outflow Water due to the isolation of the MedSea during the MSC should have led to reduction in North Atlantic Deep Water formation and thus poleward heat and energy transport, our results suggest the contribution of eddies may have prevented abrupt global climate change during this event.

Base level lowering, which alters the water budget, must be taken into account when considering the freshwater budget during the MSC. To get the most quantitatively useful information for the MSC we must take into account all known changes including paleo-physiography, orbital changes, and MedSea level variations. We are currently investigating these changes in further experiments with CAM3. A future paper will discuss the effect of orbital precession, on the water budget of the Med-Sea. We are also planning coupled model experiments to investigate the response of the thermohaline circulation of the Atlantic Ocean to the loss of the Mediterranean outflow water.

3.7 Tables

Table 3.1: Description of our simulations conducted using NCAR CAM3-SOM.

CASE NAMES	Messinian Event	Description
CNTL (Control Run)	n/a	Used to determine the impact of our implemented Q flux on climate
US (Upper Sea)	Control	Horizontal heat transport through the strait is eliminated
UL (Upper Land)	Sensitivity	to check the sensitivity of removing the MedSea
	Sensitivity	to check the sensitivity of removing the MedSea
HL (Half Land)	Sensitivity to MedSea level lowering	Same as UL but now the surface is lowered 750 m.
	Sensitivity to MedSea level lowering	Same as UL but now the surface is lowered 750 m.
LL (Lowered Land)	"Messinian Gap" Same as UL	Simulates the "Messinian Gap"
	but now the surface is lowered 1500 m.	when the MedSea was completely desiccated.
LS (Lowered Sea)	"Upper Evaporite" layer. Same as US	Simulates the period when the "Upper Evaporite" layer was deposited.
	but now the surface is lowered 1500 m.	Shallow, briny pools of water existed thousands of meters below sea level.

Table 3.2: Area averaged annual mean evaporation, precipitation and annual atmospheric water budget (E-P) integrated over the Mediterranean Sea (6°W-37°E, 30°N-46°N).

CASE	Evaporation [mm day^{-1}]	Precipitation [mm day^{-1}]	Annual Water Budget (E-P) [mm day^{-1}]
US	3.35	1.00	2.32
UL	0.46	0.56	-0.04
LL	0.31	0.37	-0.03
LS	3.48	0.88	2.57

3.8 Figures
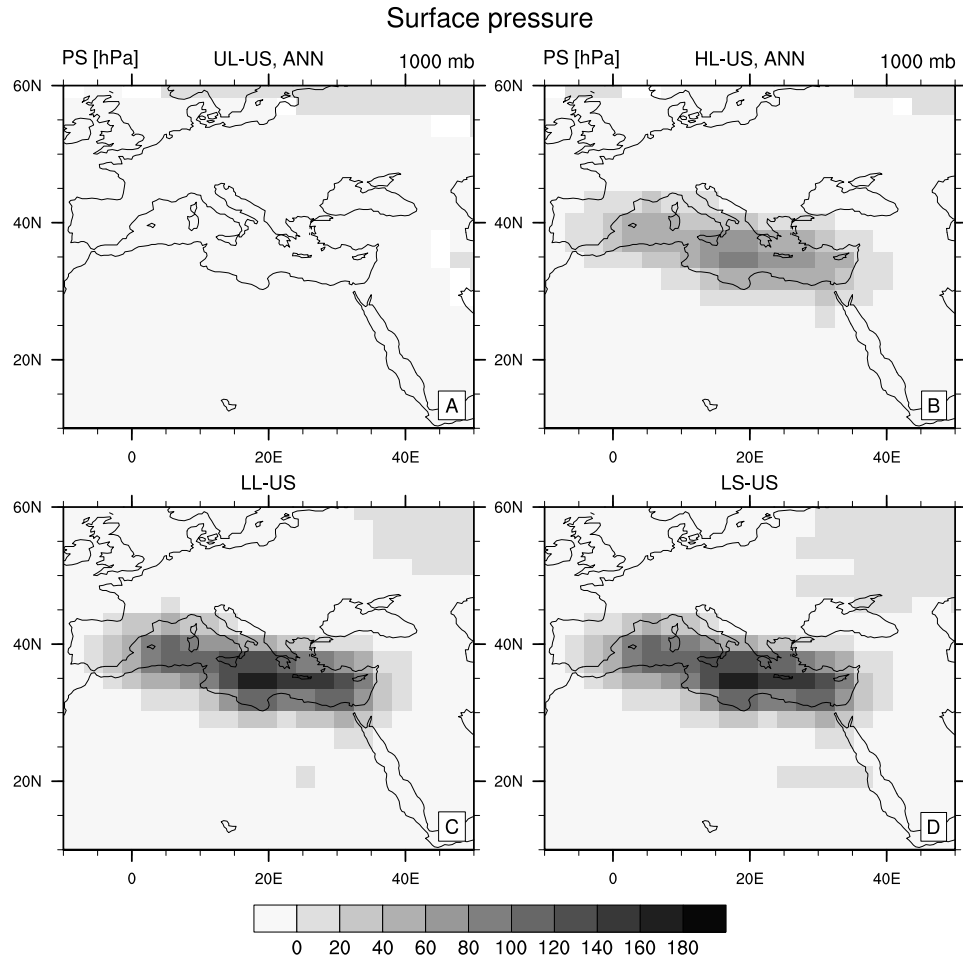
Figure 3.1: Annually averaged surface pressure anomalies (hPa) for the UL (A), HL (B), LL (C), and LS (D) simulations. All panels show statistically significant differences at the 95% level only.

Surface temperature (radiative)
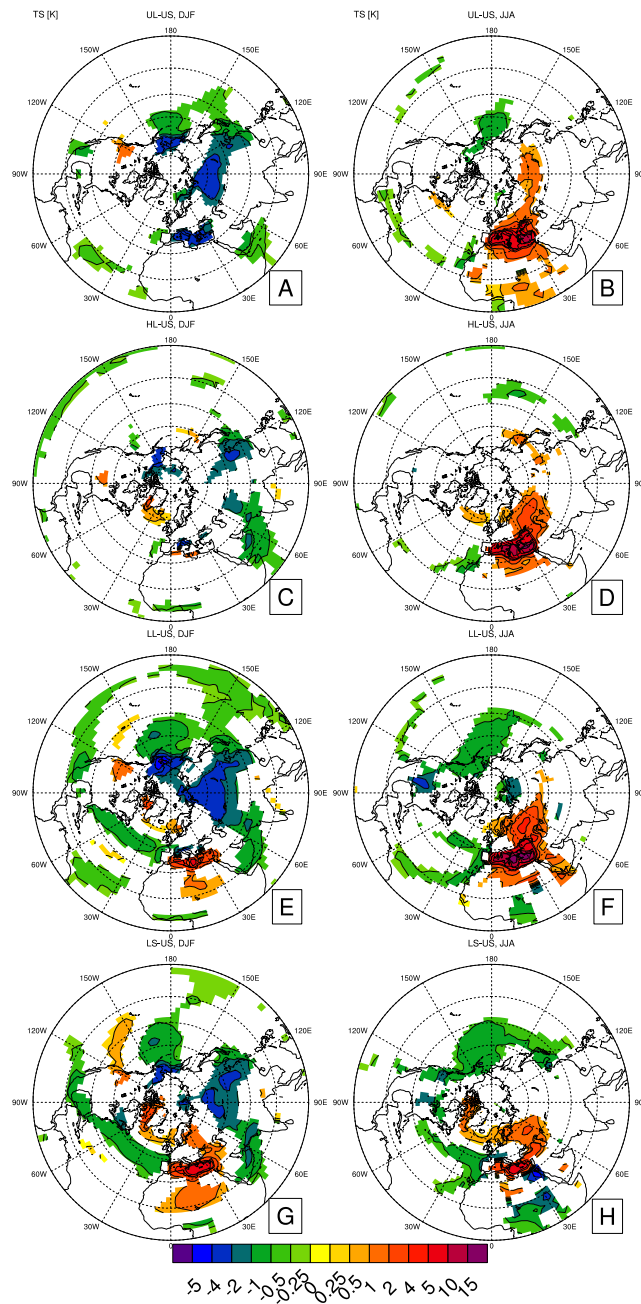
Figure 3.2: Northern Hemisphere Polar Stereographic plots of surface temperature (TS) anomalies (K) for the UL (A and B), HL(C and D), LL (E and F), and LS (G and H) simulations. Winter (DJF) anomalies are on the left and summer (JJA) anomalies are on the right. All panels show statistically significant differences at the 95% level only.
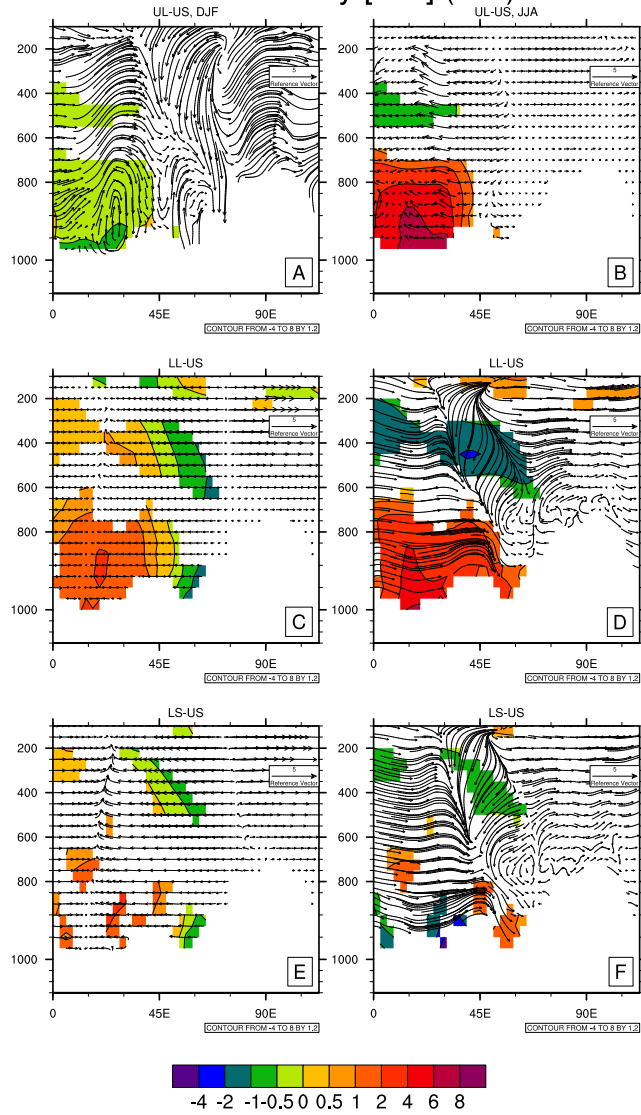
Figure 3.3: Meridional (north-south) vertical cross sections of temperature anomalies (shaded) (K) and wind anomalies (vector) (m s-1) averaged latitudinally from 30°to 40°N for the UL (A and B), LL (C and D) and LS (E and F) simulations. Winter (DJF) anomalies are on the left and summer (JJA) anomalies are on the right. All panels show statistically significant differences at the 95% level only.

850-hPa Omega Anomaly [Pa/s] (shaded) and 850-hPa Wind Anomaly [m/s] (vec)
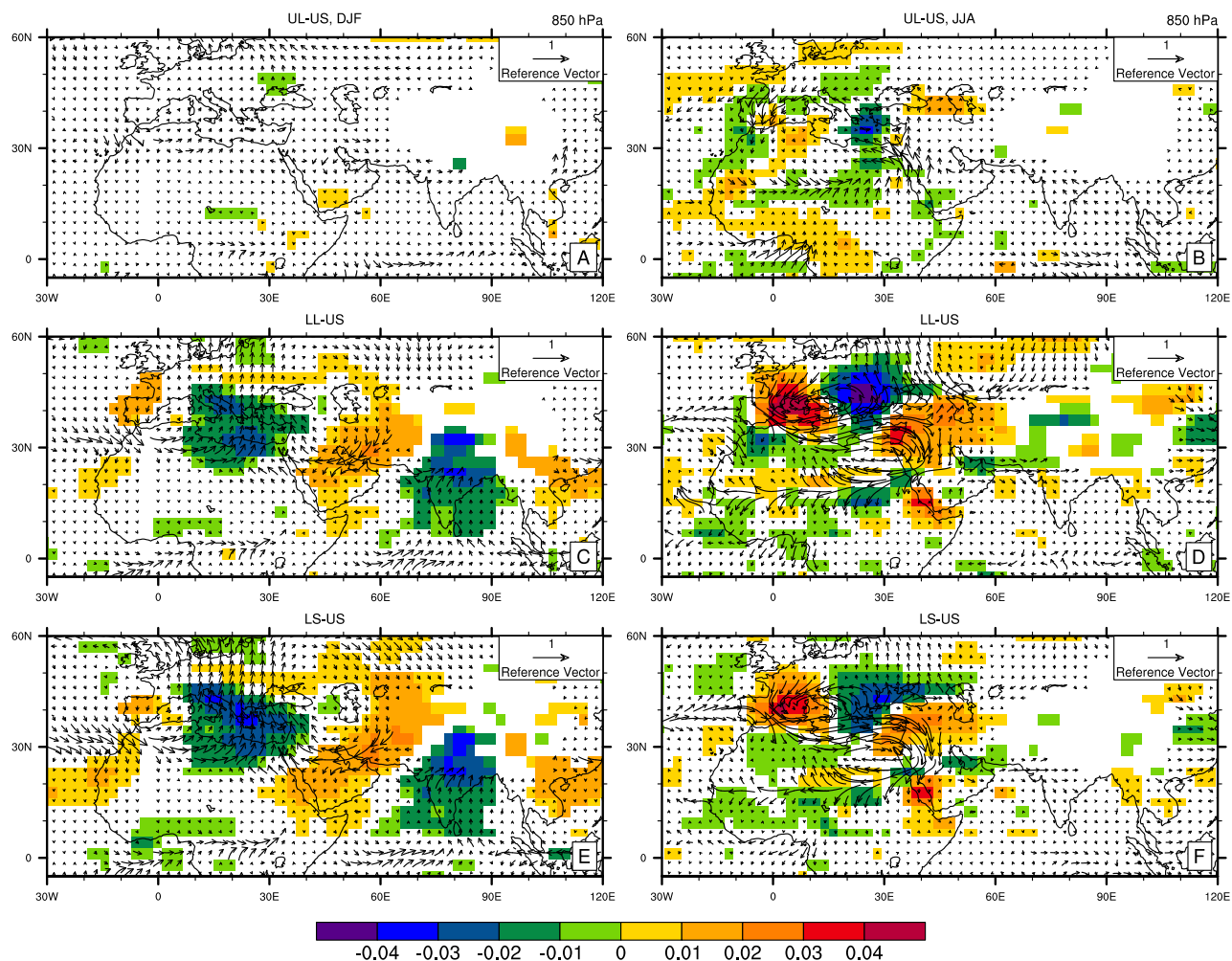
Figure 3.4: Vertical velocity (shaded) (Pa s^{-1}) at 500-hPa, and wind anomaly (vectors) (m s^{-1}) at 850-hPa over the Mediterranean and Southern Eurasia for the UL (A and B), LL (C and D), and LS (E and F) simulations. Winter (DJF) anomalies are on the left and summer (JJA) anomalies are on the right. All panels show statistically significant differences at the 95% level only.

Total Precipitation Anomaly
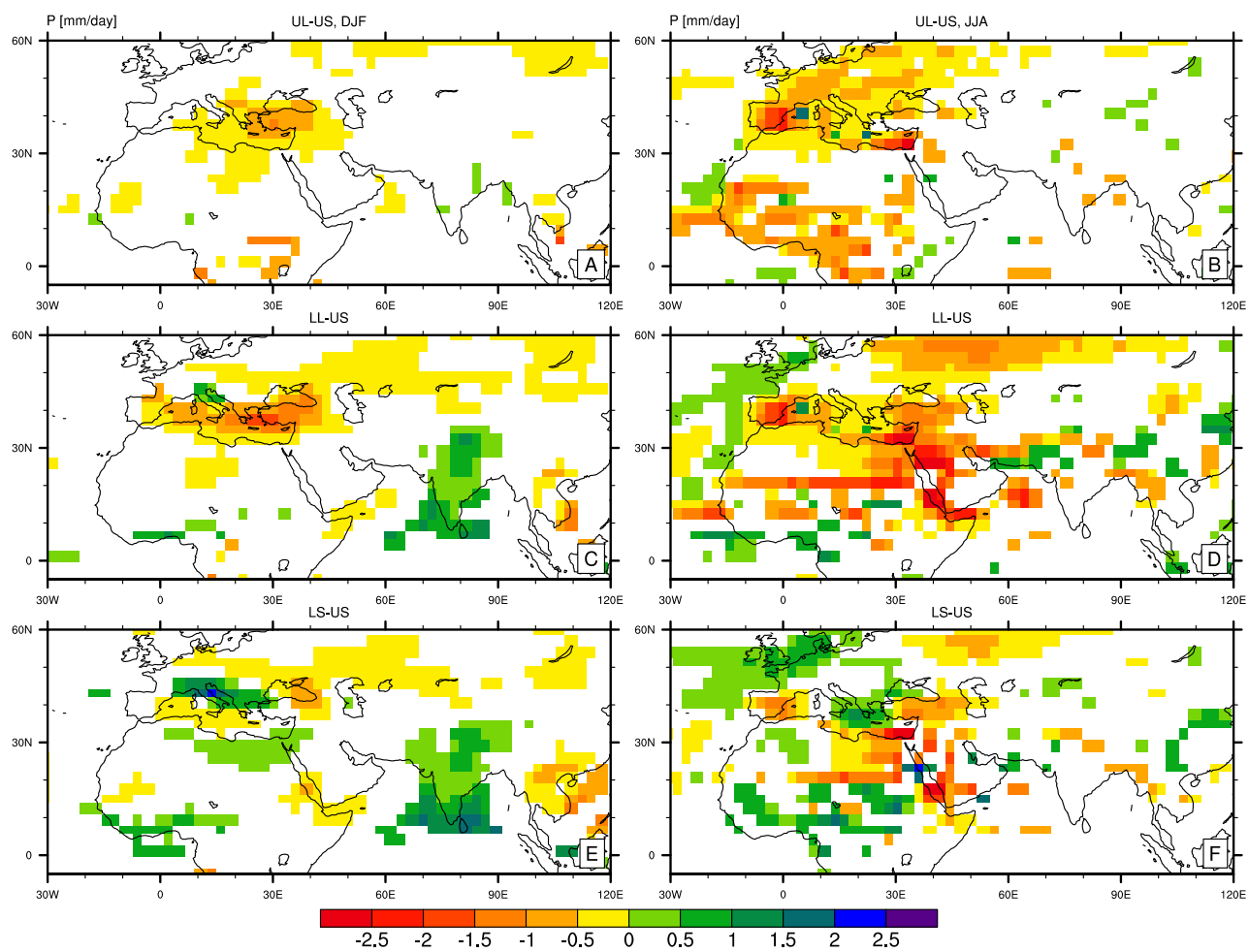
Figure 3.5: As Fig. 3.4 but showing total precipitation (mm day^{-1}). Total precipitation includes both convective and large-scale precipitation.

Figure 3.6: As Fig. 3.4 but showing the vertically integrated precipitable water (kg m^{-2}).
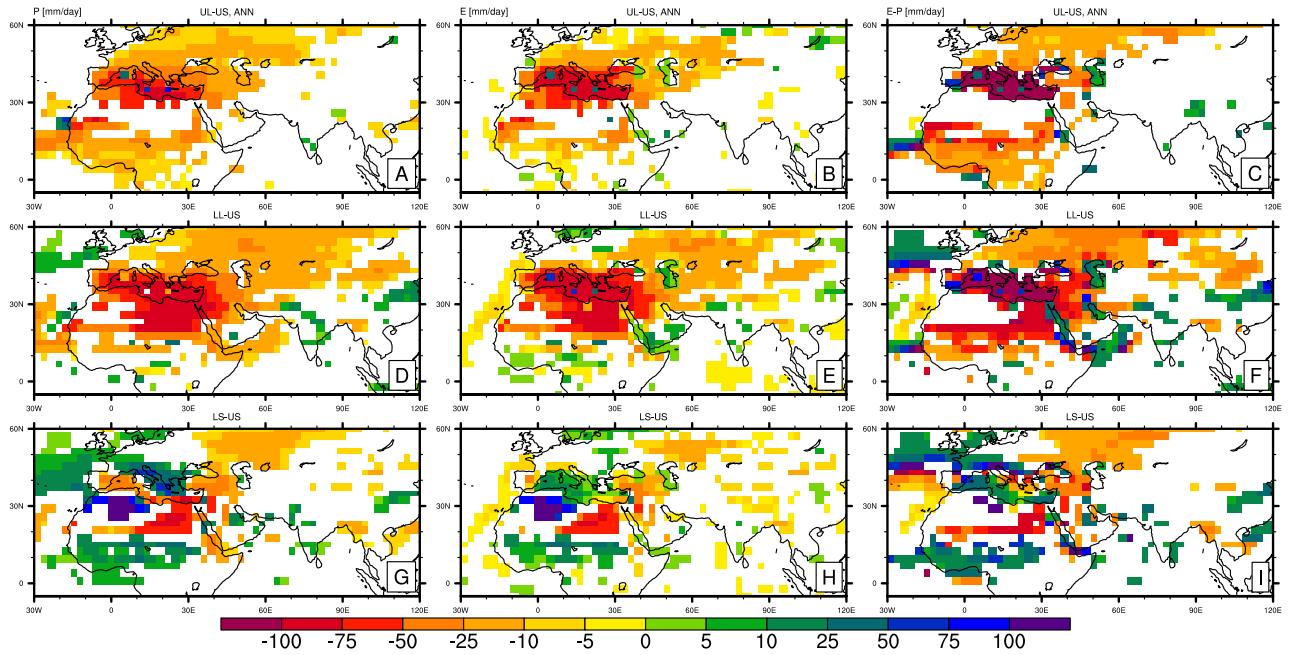
Figure 3.7: Annual mean percent change in precipitation (left column), evaporation (middle column), and evaporation minus precipitation (right column) (mm day−1) over the Mediterranean and Southern Eurasia for the UL (top row), LL (middle row), and LS (bottom row) simulations. All panels show statistically significant differences at the 95% level only.

Geopotential Height (above sea level)
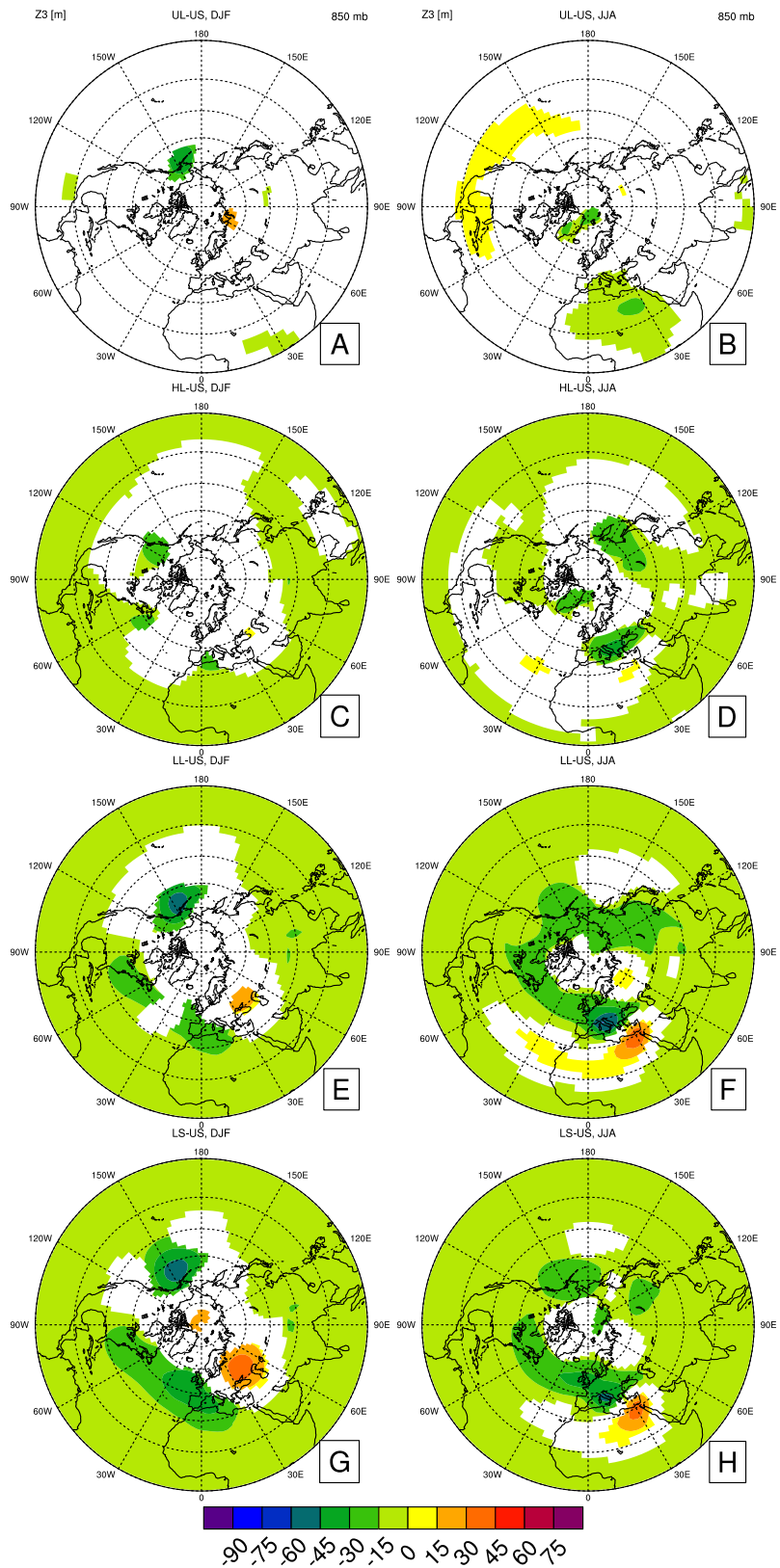
Figure 3.8: As Fig. 3.2 but showing the geopotential height anomalies (m) at 850–hPa.

Geopotential Height (above sea level)
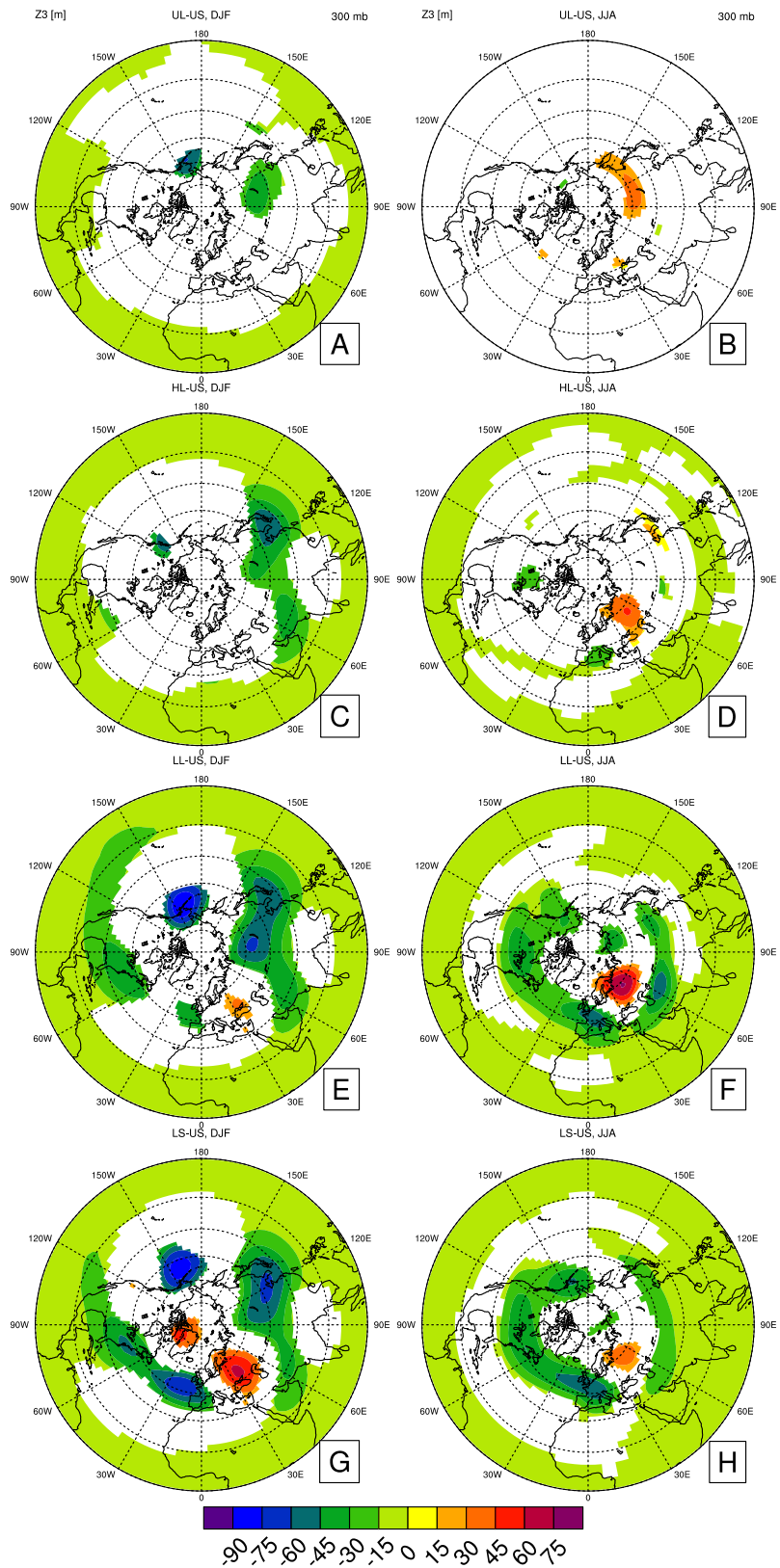
Figure 3.9: As Fig. 3.2 but showing the geopotential height anomalies (m) at 300–hPa.

Variance of V

US, DJF

LS-US, DJF

UL-US

LL-US
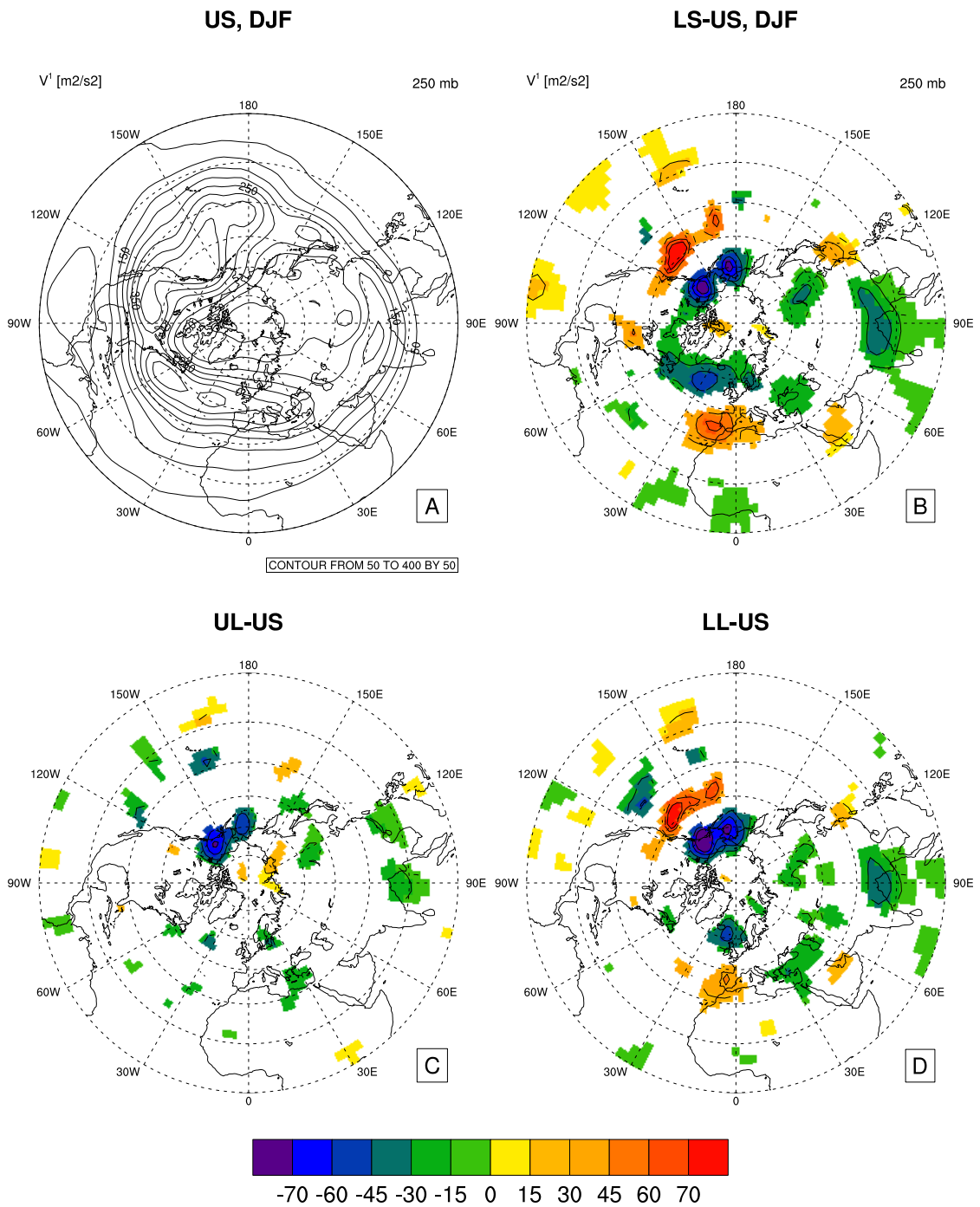
Figure 3.10: Northern Hemisphere Polar Stereographic plots of DJF 250–hPa meridional velocity variance for the US (A) and anomalies for the UL (B), LL (C), and LS (D) simulations. Anomaly panels show statistically significant differences at the 95% level only.

Surface temperature (radiative)
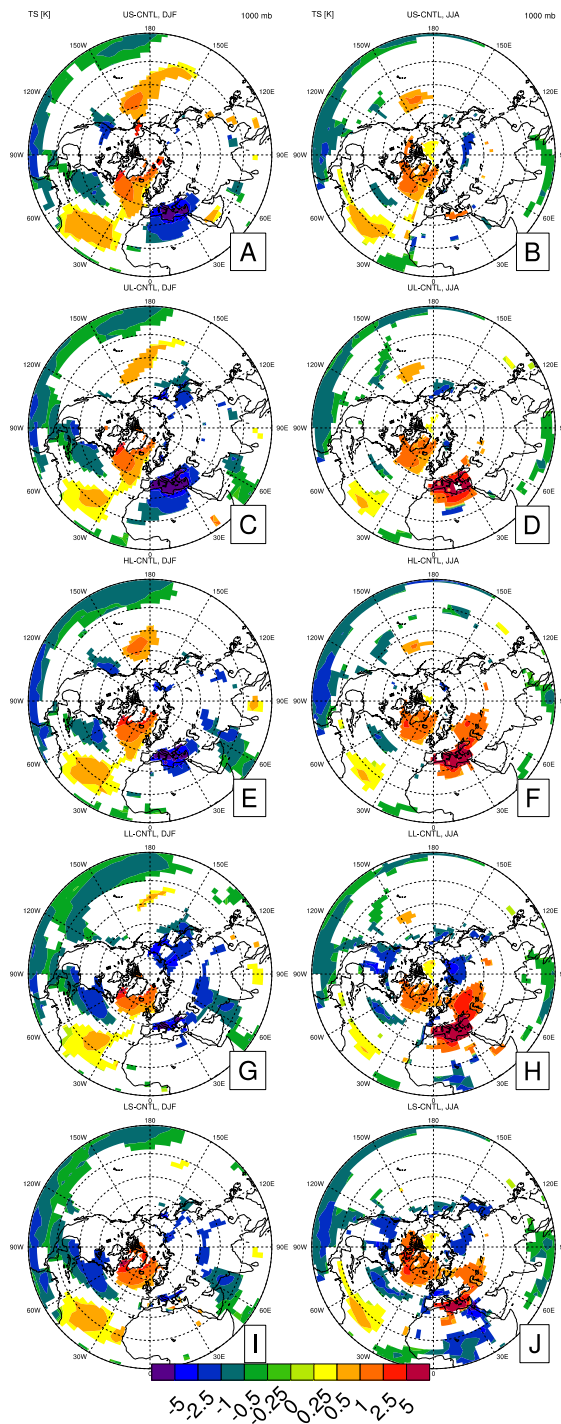
Figure 3.11: Northern Hemisphere Polar Stereographic plots of surface temperature anomalies (K) for the US (A and B), UL (C and D), HL (E and F), LL (G and H), and LS (I and J) simulations. Differences are with respect to a control run with no change in Q flux (CNTL). Winter (DJF) anomalies are on the left and summer (JJA) anomalies are on the right. Only statistically significant differences are shown.

Geopotential Height (above sea level)
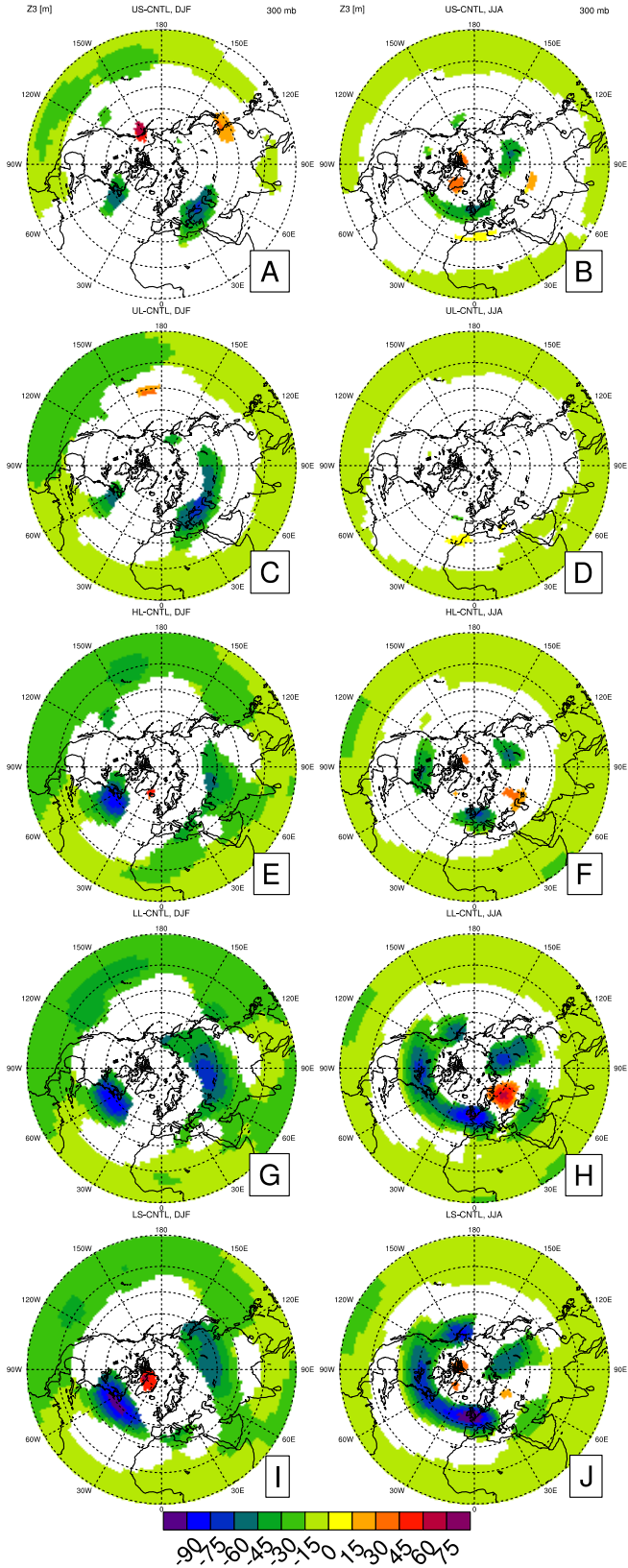
Figure 3.12: As Fig. 3.11 but showing the geopotential height anomalies (m) at 300–hPa.

61
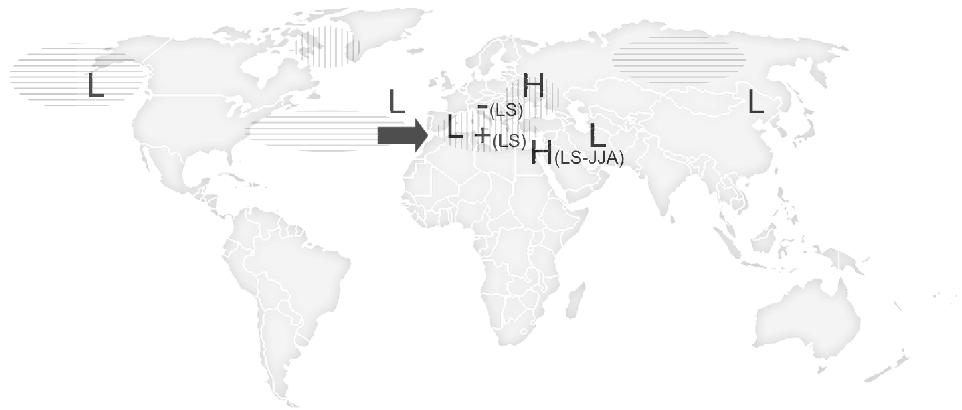
Figure 3.13: A schematic illustration of the most salient changes that occurred in our simulations of the MSC. The circles with vertical lines indicate locations where surface temperatures warmed. The circles with horizontal lines indicate locations where surface temperatures cooled. The H's are regions where the surface pressure increased and the height field was raised and the L's indicate regions where the surface pressure decreased and the height field was lowered. The positive sign indicates where the annual E-P was positive (LS run) and the negative sign indicates where the annual E-P was negative (LS run). The thick black arrow indicates where the winter storm track was strengthened (LS and LL run).

Chapter 4

Orbital Forcing Experiments

4.1 Abstract

In this chapter we use the NCAR Community Atmosphere Model configured with a Slab Ocean to investigate how orbital variations, namely precession maximum (P+) and minimum (P-), drive hydrological changes during the MSC. Previous Late Miocene modeling studies (Favre et al; Gladstone et al., 2006; Steppuhn et al., 2006; Francois et al., 2006; Murphy et al., 2009) have not taken into account orbital forcing. This is the first study to detail how reduced MedSea level (Lowered Sea, LS) alters orbitally-driven climate change. We focus on regional hydrological changes in the MedSea and the North African summer monsoon response, which is sensitive to MedSea level. Increased precipitation and runoff over the northern periphery of the MedSea and increased evaporation of the MedSea at reduced sea level occurs under all orbital signals. Sinced lowered MedSea level increases the water deficit, the fresh to brackish water conditions during the Lago Mare event is expected to occur at precession minimum and at relatively high MedSea level. Another robust feature occurs over the West African monsoon region where reduced MedSea level substantially increases precipitation over this region.

4.2 Introduction

The Mediterranean Sea (MedSea) is a semi-enclosed sea that has a strong seasonal cycle consisting of hot, dry summers and mild, wet winters. Atlantic Ocean water enters the MedSea at the surface of the Gibraltar Strait. High evaporation and evaporative cooling increases the density of the water and results in deep-water formation in the eastern MedSea. Below the surface of the strait, highly saline MedSea deep-water enters the Atlantic Ocean and sinks to a depth of $\sim$1000 m. This water mass is known as Mediterranean outflow water (MOW) and is the warmest (13°C), saltiest (38.4 psu) water at this depth in the global ocean (Price and Baringer, 1994). The salinity of marginal basins, such as the MedSea, is especially sensitive to small climate perturbations. Roughly 6 Ma during the Messinian Salinity Crisis (MSC), tectonic collision between Africa and Europe closed the Mediterranean-Atlantic connection. The elimination of Atlantic inflow and high rates of evaporation, resulted in the evaporation and desiccation of the MedSea. Evaporation deposited between 1000-3000 m of evaporites that consist of alternating sequences of gypsum and shale. Cyclical sediments represent high-frequency salinity changes resulting from orbitally-induced climate variability (Krijgsman *et al.* (1999)).

Periodic changes in the Earth's orbital parameters, which include precession, obliquity, and eccentricity, affect the distribution and strength of incident insolation and may be the primary driving force in past climate change events on timescales from 20 kyr to 100 kyr (Zachos *et al.* (2001)). Precession is the change in the orientation of the Earth's axis with respect to fixed stars; full cycles occur over approximately

19,000 and 23,000 years. Precession maximum (minimum) occurs when winter (summer) solstice is at perihelion. Eccentricity, the departure of the Earth's orbit around the sun from a perfect circle, influences the net seasonal and annual insolation and has a quasi-periodicity of 400,000 and 100,000 years. Eccentricity modulates the influence of precession such that during periods of high eccentricity, the effect of precession on seasonal insolation is strong. The tilt of the Earth's axis relative to the orbital plane, or obliquity, alters the latitudinal distribution of incident solar radiation. Orbital forcing plays an important role in the North African monsoon (Kutzbach (1981); Kutzbach and Otto-Bliesner (1982)). Precessional forcing has a significant effect on the climate of North Africa and Southeast Asia (Floegel and Wagner (2006); Griffin (2002)).

The first stage of the MSC is characterized by the "Lower Evaporite" unit and contains 16-17 precessional cycles. It is hypothesized that evaporite deposition in the Mediterranean would occur during precession maximum (P+), which is characterized by increased aridity and higher dust flux from the Sahara; precession minimum (P-), characterized by wetter conditions and low dust flux, would subsequently refill the basin (Sierro *et al.* (1999);Krijgsman *et al.* (1999);Larrasoana *et al.* (2006)). Greater boreal summer insolation has been shown to shift the ITCZ northwards (Ruddiman, 2001). Modeling studies have shown that the circulation within the MedSea is very sensitive to changes in freshwater fluxes. Increased freshwater input into the MedSea inhibits deep-water convection and deposits organic-rich layers known as sapropels (Rossignol-Stick (1983)). Griffin (2002) suggested the drawdown of the MedSea transported greater moisture to North Africa, initiating the Ziet Wet

Phase, which would consequently have supplied more runoff to the MedSea.

The second stage of the MSC, the "Upper Evaporite" unit, contains at least eight precessional cycles (CIESM (2008)). The "Upper Evaporite" unit marks a change in the MedSea hydrological budget influenced by precession-driven climate changes (Krijgsman *et al.* (2001)). The latest stage of the "Upper Evaporite" unit, the Lago-Mare, is characterized by a significant shift in the MedSea water balance towards fresher conditions. The upper unit consists of gypsum and marls, characteristic of hypersaline condtions, while the lower unit, the Lago-Mare event, is characteristic of non-marine deposits of fresh to brackish water conditions ($\sim$5-20 g/l) (CIESM (2008)). The Lago-Mare event indicates a change in the hydrological conditions of the MedSea and increased freshwater input into the MedSea. Cooler and wetter (mostly near the mountainous regions) conditions are believed to have existed during the Lago-Mare event (Rouchy and Caruso, 2006). Can a precession-driven increase in freshwater runoff tip the MedSea water balance to allow for Lago-Mare condition?

The level of the MedSea during evaporite deposition is still controversial, since the level depends on the uplift rate at the straits and the water budget of the Med-Sea. Hilgen *et al.* (2007) and Krijgsman *et al.* (2001) favor a deep water model with continuous surface water input from the Atlantic, but blocked return flow at depth. Clauzon *et al.* (1996) suggests a shallow water model that underwent several cycles of desiccation and refilling. The Gargani and Rigollet (2007) modeling study shows numerous MedSea falls between 500-2500 m but states that uncertainty in the Mediterranean water budget would impose a +-10% uncertainty on the estimation

of MedSea level. Meijer and Krijgsman (2005) found that the degree of halite and gypsum saturation in the MedSea is critically dependent on the freshwater budget, especially in the eastern sub-basin where there is greater fresh water runoff into the sea. Previous studies on the salt precipitation in the MedSea have used present-day hydrological fluxes (Meijer (2006); Meijer and Krijgsman (2005)). External forcing has been a key constraint on understanding past salinity transitions. How do precession forced changes in the regional climate alter the MedSea hydrological cycle? These climate changes may be responsible for the major salinity fluctuations from marine (35-38 g/l) to hypersaline (130-160 g/l) conditions during the MSC. This work improves upon past modeling efforts on the MSC and is the first to examine the effect of external forcing on hydrological fluxes during the Late Miocene.

Murphy *et al.* (2009) found that reduced MedSea level increases the water deficit compared to control conditions, suggesting that a partially-filled basin cannot be sustained. Uncertainty regarding the water budget leads to uncertainty in the desiccation process and in determining the cause of major salinity transitions. It is also important to determine how sea-level-induced climatic changes feed back on the hydrological cycle, and therefore the desiccation process, during the MSC. We utilize an atmosphere-mixed layer ocean general circulation model to examine the role of the Mediterranean Sea level on precession-driven changes in regional water budget to provide improved estimates of palaeo-hydrological fluxes.

4.3   Experimental design

The NCAR Community Atmosphere Model (CAM) version 3 (Collins *et al.* (2004)) coupled to a Slab Ocean Model (SOM) and the Community Land Model (CLM3) is used in this study. CAM uses a terrain following hybrid coordinate with a spectral Eulerian dynamical core that has 26 vertical levels. While the SOM does not simulate the full ocean circulation, Sea Surface Temperatures (SSTs) are able to respond to atmospheric changes. The mixed layer SOM includes a thermodynamic sea ice component. A greater discussion on the implemented horizontal oceanic heat transport can be found in Murphy *et al.* (2009). Salinity dynamics are not accounted for in the SOM. The Community Land Model (CLM3) (Oleson *et al.* (2004)) incorporates biogeophysics, hydrological cycle, and biogeochemistry. A river transport model is utilized in CLM to transport total runoff over land to the ocean. Human water consumption and irrigation are not taken into account (Oleson *et al.* (2004)). Greater detail of this model is provided in Collins *et al.* (2004) and Oleson *et al.* (2004).

All simulations are run at T42 resolution (an equivalent grid spacing of roughly 2.8°x 2.8°). Branch runs were integrated from the equilibrated state of the Lowered Sea (LS) and Upper Sea (US) simulations described in Murphy *et al.* (2009). A simple set up of prescribed present-day vegetation and present-day greenhouse gas concentrations are used. Table 4.2 describes the orbital characteristics used in each simulation. Since the number sedimentary patterns do not account for changes in obliquity, we keep obliquity and eccentricity constant in our precession minimum

and precession maximum simulations. Obliquity is held at the present day value of 23.45°and eccentricity is increased to 0.05 to account for maximum seasonality in orbital precession. Under a more circular orbit, such as the present (eccentricity is 0.0167), precession has a negligible climatic effect. Precession in our experiment will have a larger effect on climate in our maximum precession simulations (LS_P+, US_P+). Jackson and Broccoli (2003) found that many climate variables respond linearly with respect to eccentricity. Maximum and minimum values of precession during the MSC are taken from Laskar *et al.* (1993). In the Lowered Sea and Upper Sea maximum precession simulations (LS_P+, US_P+), the Earth's vernal equinox at perihelion is set to 90°; in the Lowered Sea and Upper Sea minimum precession simulations (LS_P-, US_P-), it is set to 270°.

Runoff in CLM is comprised of surface (qover), sub-surface drainage (qdrai) and runoff from glaciers, lakes and wetlands (qrgwl).

$$R = qover + qdrai + qrgwl = E - P + \Delta SoilMoisureStorage \qquad (4.1)$$

Since we are not running with an active River Transport Model, we cannot calculate the volume of runoff at deltas. Instead, we show the column level runoff as simulated by the land model. Runoff from glaciers, lakes and wetlands accounts for any deficit in the water budget and can be negative. Three MedSea grid points that are considered wetland regions add a negative contribution to total runoff. In our results, annual and seasonal averages of total runoff do not include this contribution.

4.4 Results

4.4.1 Insolation response

Climate change in our US_P+ and US_P- simulations are driven by differences in the spatial and temporal distributions of insolation. This external forcing is due to changes in the orbital parameters that are described in Table 4.2. Figure 4.1 shows the seasonal cycle of insolation averaged for the Northern Hemisphere (NH) for present day orbital parameters (green), maximum precession (red) and minimum precession (blue). Precession minimum results in stronger seasonality in the NH, with stronger insolation in the summer and weaker insolation in the winter. Precession maximum reduces this seasonality. Seasonal insolation in our modern simulation (US_CLIM) is closer to precession maximum. Similar to Braconnot *et al.* (2007) we calculate seasons based on the present day calendar rather than a celestial calendar, which is based on the time equinoxes. Figure 4.2 shows a latitude versus time plot of mean (figures 4.2A, 4.2B and 4.2C) and anomalous (figures 4.2D, 4.2E and 4.2F) zonally averaged insolation. Figure 4.2F shows the difference between precession minimum and maximum. In the Arctic, there is more insolation from May through July and less from August through October. Between November and March, there are minimal differences in insolation between maximum and minimum precessional forcing. In the Northern Hemisphere, insolation is increased (decreased) by more than 80 W m^{-2} in the summer (winter). In general, insolation is a function of latitude. Although the seasonal distribution of heat is different in our minimum precession simulations compared to our maximum and modern precession runs, the

annual global mean of incident solar flux does not vary much within our orbital simulations. The present day global annual mean insolation is 341.842 W m^{-2} and becomes 342.095 W m^{-2} and 342.281 W m^{-2} for the precession minimum and maximum simulations, respectively.

Precession forced variations in seasonal insolation (P- relative to P+) results in strong global temperature changes (4.3). Figure 4.3 shows the seasonal differences in surface temperature. Precession minimum leads to a strong cooling in winter and spring (figures 4.3A, 4.3C) that is strongest over land. During the summer, higher insolation under precession minimum conditions leads to a warming that is strongest over land due to higher specific heat compared to the ocean. Strong continental heating results in greater precipitation over the Northern Africa and Northern South America, while reducing precipitation over nearby ocean regions (figure 4.4). Evaporative cooling and cloudier conditions cool North Africa in the summer. In the fall, opposite hemispheric patterns arise. In the NH, a reduction in insolation leads to cooling; the opposite is true in the SH. We would expect precession minimum to result in a cooler autumn and warmer spring, however, because of the tilt of the Earth's axis, in boreal autumn the NH (SH) receives less (more) insolation at precession minimum compared to precession maximum.

Precession minimum results in stronger convergence over North Africa which leads to wetter conditions over Northern Africa and the MedSea (figure 4.5). Figure 4.5 shows the difference in summertime (JJA) velocity potential and divergent wind fields at 850-hPa (figure 4.5a) and 200-hPa (figure 4.5b) due to precession changes. The large-scale circulation in the summer is characterized by convergence at the

surface and divergence aloft in southeast Asia. This ascending motion is associated with the monsoon circulation. Divergence at the surface and convergence aloft indicate subsiding motions in the southern tropical Atlantic. The largest precession difference occurs over Northern Africa, where precession minimum forces strong ascending motion. We also find anomalous rising motion over Northern South America and increased subsidence over much of the North Pacific Ocean. Figure 4.4B shows JJA anomalous precipitation due to precession changes. It is apparent that the large-scale subsidence and ascending motions shown in Figure 4.5 are associated with greater precipitation over Africa, Indonesia and the Amazon and drier conditions in the North Pacific. Anomalous convergence occurs in the Atlantic and Indian Ocean around 10°S. Intense divergence over the Pacific corresponds to reduced precipitation. A reduction in the annual mean temperature of the NH during precession minimum shifts tropical precipitation into the Southern Hemisphere (fig 4.6). Annually, there is greater precipitation over Northern Africa and the MedSea during P-. Interestly, reduced precipitation over India and increased precipitation over the eastern MedSea is consistent with theories linking remote changes in strength of the Indian monsoon to subsidence and aridification over the eastern MedSea (Rodwell and Hoskins (1996)). Our results show an increase in precipitation over the Bolivian Altiplano in agreement with findings that wet cycles in sediment cores drilled in the tropical Andes are correlated with precession minimum orbital conditions (Baker *et al.* (2001)).

4.4.2 Mediterranean Sea Hydrological Cycle

4.4.2.1 Comparison with proxy data

In the Gladstone *et al.* (2007) Late Miocene study, MedSea level lowering and desiccation were not taken into account. These features have been shown to shift the precipitation distribution and alter the water budget, respectively (Murphy *et al.* (2009)). Figure 4.7 shows the influence of reduced MedSea level on the water budget terms for precession maximum (left) and precession minimum (right). The spatial pattern at precession maximum is very similar to present day, where reduced MedSea increases precipitation over the Northeastern MedSea and decreases precipitation in the southeastern MedSea. This pattern is observed under both precession signals and should be reflected in the observational record.

Fauquette *et al.* (2006) used the relationship between relative pollen abundance of each individual taxon sampled and climate to quantify the climate of periods for which there are currently no modern analogs of the pollen spectra. This is achieved by transposing the climate requirements of the maximum number of modern taxa to the fossil data. The most likely value corresponds to the weighted mean. Here, we compare our simulations to mean annual precipitation based on the available pollen data. Figure 4.8 shows Fauquette *et al.* (2006) proxy data for the period corresponding to "Lower Evaporite" deposition (roughly 5.96-5.59 Ma). The black circles show the data values based on pollen reconstructions with corresponding error bars that reflect the uncertainty in each data value. There are eleven sites located around the periphery of the MedSea. Carmona, Andalucia, and Tarragona are located in South-

ern Spain; Bou Regreg and Habibas are in Northwestern Africa; Eraclea Minoa and Racalmuto are located in Sicily; Torre Sterpi, Borgo Tossignano, and Maccarone are located in Northern Italy; Site 380A is in the Black Sea. Our control US simulations are marked in blue at modern (diamond), minimum (triangle), and maximum (square) values of precession. Our LS simulations are marked in red. Finally, the green stars show present day climatological values based on the CMAP dataset (Xie and Arkin (1996)). Comparing the proxy data to current precipitation values highlights the difference in precipitation during the "Lower Evaporite" deposition. The Italian and Black Sea pollen data show an increase in annual mean precipitation compared to present day. Our LS simulation results in wetter conditions along the Northeastern border of the MedSea compared to our US simulation, which is in better agreement with proxy data. This suggests there was reduced MedSea level during the "Lower Evaporite" phase.

Comparisons between model data and pollen sites is problematic, since pollen is derived from a core and is representative of the immediate local environment, while model output is derived from a grid box whose center is closest to the core. Each model grid box has an area on the order 105 km^2. CMAP data is given at an even coarser resolution (2.5x2.5°grid spacing)

.

4.4.3 Mediterranean Sea Temperature

Comparing the seasonal cycle of temperature in the US and Cntl runs to NCEP-NCAR Reanalysis data shows that eliminating the horizontal heat transport to the MedSea cools the basin in the winter and warms it in the summer; however, the amplitude of the seasonal cycle is consistent with that of the NCEP-NCAR Reanalysis (figure 4.9). In the annual mean, Mediterranean SST in our US run is similar to the present day, while the LS run is slightly warmer than present day. The MedSea is the coolest in February and warmest in August in all runs, which agrees with the data. SST has a strong influence on evaporation within the MedSea. Warmer SSTs at reduced MedSea sea level, leads to greater evaporation and results in a precipitation maximum in August. In January and February, the MedSea surface temperature in the US run is reduced by nearly 3°C compared to reanalysis data. In the summer, the MedSea is warmed by roughly 3°C. CAM-SOM simulations are generally too warm during the summer, yet is in good agreement throughout the rest of the year. Reducing the MedSea sea level (LS) leads to a large warming throughout the year. In August, the LS run is 5°C warmer than NCEP-NCAR reanalysis. Typically, the MedSea gains 5.2 ± 1.3 W m^{-2} through advective heat flux (Macdonald *et al.* (1994)). In the absence of heat flux into the MedSea, adiabatic compression into the lowered basin results in a LS that is as warm as the PD during the winter. While reduced MedSea leads to strong heating in the summer, the elimination of horizontal heat transport into the MedSea during the winter prevents the LS SSTs from exceeding PD temperatures. This may ex-

plain why reconstructions based on pollen do not show large climate change during the MSC in locations around the MedSea periphery. Precession minimum results in greater seasonality in Mediterranean SST, with maximum SST reached in July, consistent with insolation maximum forcing. In July, US_P- is 7°C warmer than NCEP-NCAR Reanalysis. When the sea is reduced, the SST maximum lags one month.

4.4.4   Water budget of North Africa

In Section 4.4.1 we showed that orbital forcing has a strong influence on precipitation through changes in seasonal insolation. Annually, there is more precipitation over the MedSea and North Africa, especially Northeastern Africa, during precession minimum compared to precession maximum (4.6). Figure 4.7 shows the changes in the water budget due to reduced MedSea level. We zoom in to focus our discussion on the MedSea, North Africa and sourthern Eurasia. Precipitation over North Africa is dependent on both the precession signal and the level of the MedSea. During precession maximum, orographic forcing from reduced Mediterranean Sea level results in the development of anomalous low pressure (counter-clockwise rotation) center to the west and a high pressure (clockwise rotation) to the east of the Mediterranean. During the winter, LS anomalous circulation results in greater moisture transport from the Atlantic Ocean to Northwestern Africa. Increased vertical velocity leads and moisture convergence results in a wetter northwestern Sahara in DJF (this is a

50-75% increase in precipitation with respect to our control climate). Our results show that at reduced Mediterranean Sea level (-1500 m below sea level) the Sahara is warmer and Northern sub-Saharan Africa is cooler on annual time scales.

There are also features that are consistent under both precession signals. In Section 4.4.2 we discussed how reduced MedSea level increases precipitation to the northeast of the MedSea and reduces precipitation to the southwest of the MedSea. Reduced MedSea level moistens the region between the Guinea Coast and the Sahel, and reduces precipitation over Northeastern Africa into the Arabian Peninsula and through Turkey. The development of anomalous high pressure over Northeastern Africa (near Egypt) occurs in response to anomalous cooling. Over this region cold air causes the atmosphere to contract, leading to convergence in the upper atmosphere and subsidence below. Subsiding air lowers the relative humidity, leading to greater aridity in this region. This feature is consistent with proxies that record a transition from arid to humid conditions in the Adana Basin of Southern Turkey from the late Messinian into the early Pliocene (Darbas *et al.* (2008)).

The annual cycle of precipitation averaged between 10°W to 20°E over North Africa for the Cntl and modern day based on CMAP data is shown in figure 4.10CD). The anomalous precipitation over this region due to reduced MedSea level is shown for modern (figure 4.10A) and minimum precession forcing (figure 4.10B). Comparing the Cntl simulation to the CPC Merged Analysis of Precipitation (CMAP) dataset shows that North African precipitation extends ∼5°too far north into the Saharan Desert. There are deficiencies in simulating the timing of the West African monsoon in CAM-SOM. Precipitation begins about 2 months too early in the Cntl simulation,

which leads to less precipitation occurring over the summer monsoon months (June-September). There will also be limitations in simulating precipitation over eastern North Africa, particularly the Ethiopian Highlands, due to model resolution and unrealistic topography. Nevertheless, we are more concerned with the difference in precipitation over North Africa due to the Messinian desiccation. Our results show that during boreal summer a reduced MedSea results in greater precipitation over North Africa. This response is consistent under both modern precession and minimum precession forcing. Strong continental heating during precession minimum orbital forcing leads to a substantial increase in rain over the Saharan desert, extending to ∼30°N for a partially filled MedSea (LS_P-) and ∼3°N for a filled MedSea (US_P-). This suggests that the drawdown of the MedSea is not responsible for increasing the humidity of North Africa during the Zeit Wet phase (Griffin (2002)). Instead the Zeit Wet phase may result from a combination of MedSea isolation and precession minimum conditions.

During boreal summer, precession minimum results in increased warming over subtropical oceans (4.3B). Greater evaporation over subtropical oceans transports more atmospheric water vapor to the Guinea Coast. During precession minimum, reduced MedSea level results in stronger westerly flow extending from the Atlantic Ocean into North Africa between ∼4°N to 15°N (figure 4.11), resulting in greater precipitation compared to the US simulation. This represents a positive feedback in which more moisture transport into Africa leads to greater latent heat release and increased precipitation.

Increased solar forcing over the Northern Hemisphere during boreal summer under

precession minimum drives a dynamical response that involves a strengthening of the meridional overturning circulation over Africa (figure 4.12). The top and middle panels of figure 4.12 shows the JJA merdional stream function for precession minimum (left) and precession maximum (right) averaged zonally from 10°W to 20°E for our US (top) and LS (middle) simulations. The bottom panels show the difference in the stream function due to reduced MedSea level. Deep heating over the MedSea is advected over Northern Africa and leads to ascending motion. Convergence occurs at the surface between 20-30°N (figure 4.12E). Precipitation develops when the moist air reaches the convergence zone over North Africa. This results in greater precipitation under the rising branch and a northward penetration of the West African Monsoon. More precipitation over North Africa results in evaporative cooling.

4.4.4.1   Runoff

When the MedSea was isolated from the Atlantic Ocean, the MedSea climate consisted of warm, and relatively wet summers; however, during the remainder of the year, MedSea precipitation is reduced compared to PD (figure 4.7). Precession minimum forcing results in a distinct seasonality in precipitation. Figure 4.13 shows the contributions of the various terms to the freshwater budget. Runoff into the MedSea is calculated by masking values where the land mask is equal to one (indicating land only points) and averaging over values that have land fractions be-

tween 1 and 0 (partial land points). The freshwater budget of a filled MedSea under precession minimum conditions (US_P-) shows a substantial departure from modern orbital conditions (US). An extremely large increase in runoff occurs in late summer, corresponding to a peak in precipitation. In August, runoff into the MedSea is increased by an order of magnitude. Precipitation reaches its minimum value in June and causes a second, smaller peak in the fresh water deficit. The freshwater deficit is greatest in September when evaporation remains high but precipitation and runoff are reduced.

Tuenter *et al.* (2003) used a simple coupled model to show that during precession minima both net precipitation over the MedSea and runoff from the northern peripheral regions are increased. Precession minimum results in greater runoff from both the Northern borderlands and in the southeastern MedSea, where the Nile River is the largest contributor. Area-averaged MedSea evaporation is slightly increased and precipitation and runoff are substantially increased under precession minimum compared to precession maximum.

MedSea level has a significant impact on runoff (fig. 4.14). When the MedSea is reduced, there is a substantial reduction in runoff from Northeastern Africa, consistent with greater subsidence over this region. More runoff is supplied to the MedSea from the Northern borderlands due to greater precipitation. Most runoff enters the basin in DJF. Reduced MedSea level during the MSC may have also supplied more runoff to the Ivory Coast.

Precession maximum reduces the volume of runoff that enters the MedSea. Table 4.3 shows that under present day orbital parameters 0.19 mm day^{-1} of runoff en-

ters the MedSea. Under precession maximum this reduces to 0.13 mm day^{-1}, on the contrary, runoff entering the sea is almost doubled under precession minimum conditions (0.36 mm day^{-1}).

Runoff is increased at reduced MedSea level owing to greater rain over the Northern borderlands. Runoff reaches 0.27 mm day^{-1} under a reduced MedSea under modern orbital forcing and is highest at 0.40 mm day^{-1} under precession minimum conditions.

The level of the MedSea does not have a large impact on area-averaged MedSea precipitation under precession maximum. On the contrary, the level of the MedSea largely reduces precipitation by 14% and increases evaporation by 7% under precession minimum, leading to a larger MedSea water deficit compared to filled conditions.

4.4.5 African Easterly Jet

A large thermal contrast develops between land and sea in boreal summer. As the continents warm up, this induces a monsoonal circulation as a thermal low develops over Africa. This is strengthened under precession minimum, when the surface radiative forcing is increased relative to PD and precession maximum conditions. A heat low forms over North Africa and drives a monsoonal response. The strongest surface meridional temperature gradient is shifted northwards. Vertical wind shear develops to maintain thermal wind balance, creating a strong easterly jet, known as the African Easterly Jet (AEJ), centered around 600-hPa at the northern edge

of the ITCZ (4.15a,b). The AEJ is a region of moisture divergence and subsidence over the southern Sahara. Cook (2000) observed a reduction in the AEJ when the low-level baroclinicity is diminished. This has been observed when the prevailing climate over the Sahara is humid (Rowell (2003)) and is in agreement with our control US_P- simulation in which the magnitude of the AEJ is diminished compared to our US_P+ simulation (4.15a).

Reduced MedSea level warms the region through adiabatic compression as air flows into the deep basin (Murphy *et al.* (2009)). This shifts the region of maximum meridional temperature gradient, and consequently the AEJ, northwards. Drier conditions over North Africa at maximum precession results in a stronger AEJ compared to minimum precession.

4.4.5.1 Implications for Dust Transport

Horizontal and vertical wind shear generates African Easterly Waves that transport African dust westward to the Caribbean and the North America. AEW are responsible for about 30

4.5 Concluding remarks

Prior to the re-establishment of Atlantic inflow at the end of the Miocene, the MedSea experienced increased freshwater dilution and a Lago-Mare formed. Reduced MedSea level leads to enhanced precipitation and runoff from the northern

borderlands. These features are present in all orbital forcing simulations. Precession minimum results in a 110% and 90% increase in runoff into the MedSea under reduced and current MedSea level, respectively, compared to the modern orbital forcing control simulation. A 13% (31%) decrease in the MedSea water deficit occurs for the reduced MedSea level (control MedSea level) at precession minimum compared to modern orbital forcing. During precession minimum, reduced MedSea level substantially increases runoff, yet precipitation is reduced and evaporation is increased compared to filled MedSea conditions. Therefore, precession minimum can only tip the MedSea water balance to allow for Lago-Mare deposits under relatively high MedSea level. Changes in runoff can have implications on deep-water formation within the MedSea where increased freshwater input to the eastern MedSea inhibits deep-water formation. This should slow the thermohaline circulation and initiate sapropel (organic-rich sediments) deposition. Sapropels are mostly formed in the Eastern MedSea which has greater river runoff. During precession minimum, reduced MedSea level substantially dries Northern Africa and decreases runoff. However, use of a slab ocean model prohibits specifically examining changes in the Mediterranean circulation. The spatial pattern of anomalous precipitation over the MedSea with wetter conditions in the northeast and drier conditions in the southwest is consistent under all precession signals.

ODP Site 659, which is located near 18°N in the eastern Atlantic, just west of the Sahel, records past changes in African monsoon intensity. Greater precipitation over the Guinea Coast at reduced MedSea level results in more runoff into the eastern tropical Atlantic. This is in agreement with proxy evidence of enhanced total or-

ganic carbon accumulation (TOC) off equatorial West Africa at 5.65, 5.6 and 5.5Ma (Wagner, 2002).

The impact of oceanic circulation change on upwelling patterns, particularly off the West African coast, may impose feedbacks on the climate in our precession simulations. It has been shown that CCSM3 does not correctly simulate upwelling in the eastern tropical Atlantic, a feature that may influence West African monsoon rainfall (Meehl *et al.* (2006)). Changes in North and South Atlantic SSTs account for up to 50Generally, enhanced precipitation over North Africa during precession minimum reduces African dust production. Our simulations do not take this into account as dust loading has a seasonal cycle that is set at modern conditions. Although CCSM allows for vegetation-atmosphere interactions, we fail to take soil moisture and albedo changes into account due to the implementation of a spatially prescribed vegetation dataset. Soil moisture changes have been shown to enhance hydrological feedbacks in climate models (Kutzbach *et al.* (1996);Levis *et al.* (2004)).

Eolian deposition patterns in the eastern tropical Pacific Ocean indicate the ITCZ was displaced northwards of 7°N prior to 5 Ma and began shifting southwards at the beginning of the Pliocene (Hovan, 1995). Our Late Miocene study shows that reduced Mediterranean Sea stand results in greater precipitation over this region. However, the effect of restriction and closure of the Panama Strait on atmospheric-oceanic dynamics in this region should not be ignored.

4.6   Tables

Table 4.1: Description of the acronyms used for the simulations described in this article.

MedSea level	Current Orbital forcing	Precession Max	Precession Min
Upper Sea	US_CLIM, US	US_P+	US_P-
Lowered Sea	LS_CLIM, LS	LS_P+	LS_P-

Table 4.2: Orbital forcing applied to the simulations described in this article.

Simulation	US, LS	US_P+, LS_P+	US_P-, LS_P-
Obliquity	23.44627	23.44627	23.44627
Eccentricity	0.0167	0.05	0.05
Precession	102	90	270

Table 4.3: MedSea freshwater budget terms averaged over the region 3°to 46°N and 6°W to 37°E (sea points only). Averages of hydrological components are calculated using Gaussian weights. PD is present day orbital forcing, P+ is precession maximum orbital forcing, and P- is precession minimum orbital forcing.

Simulation	US	LS	US_P+	LS_P+	US_P-	LS_P-
Evaporation (E) (mm day^{-1})	3.35	3.48	3.33	3.44	3.37	3.61
Precipitation (P) (mm day^{-1})	1.00	0.88	0.88	0.88	1.53	1.32
Runoff (R) (mm day^{-1})	0.19	0.27	0.13	0.20	0.36	0.40
Water deficit [E-P-R (mm day^{-1})]	2.16	2.33	2.32	2.36	1.48	1.89

4.7   Figures
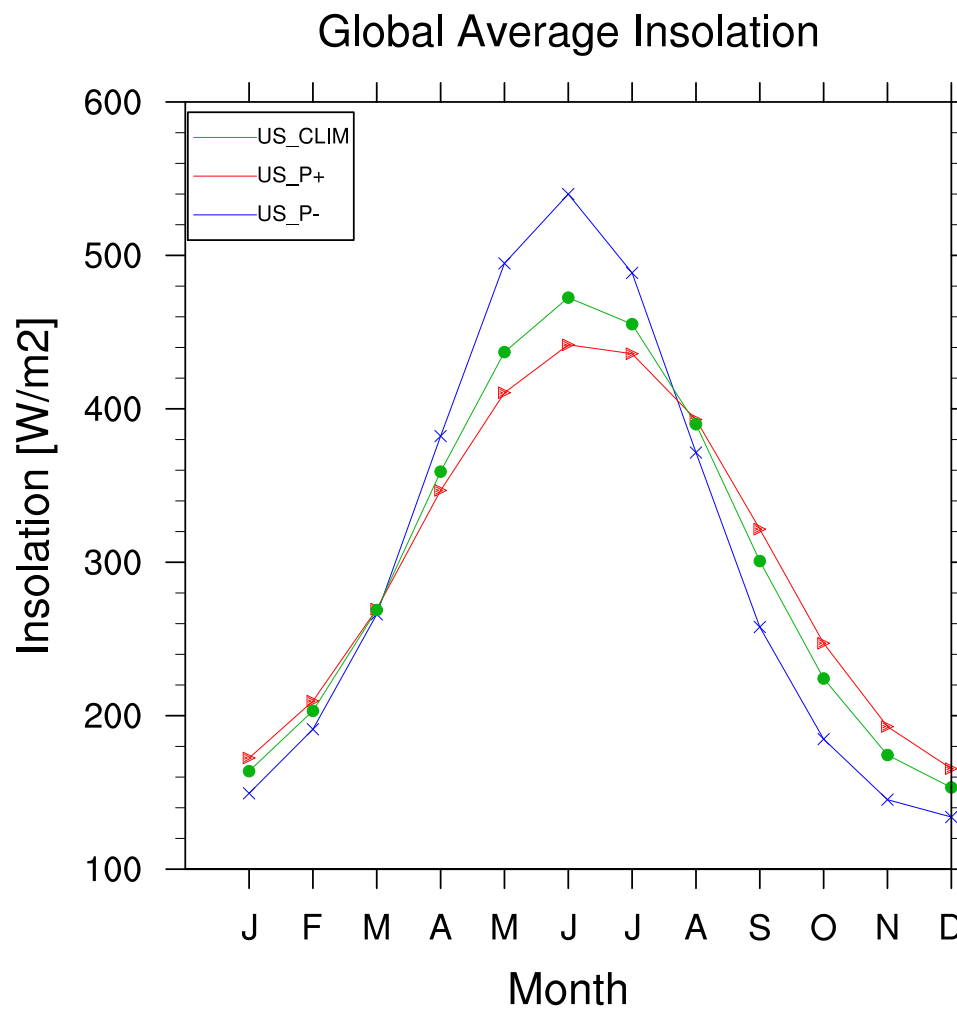
Figure 4.1: Annual cycle of Northern Hemisphere averaged insolation (W m^{-2}) for our US simulation under modern (green), precession maximum (red) and precession minimum (blue) orbital conditions.
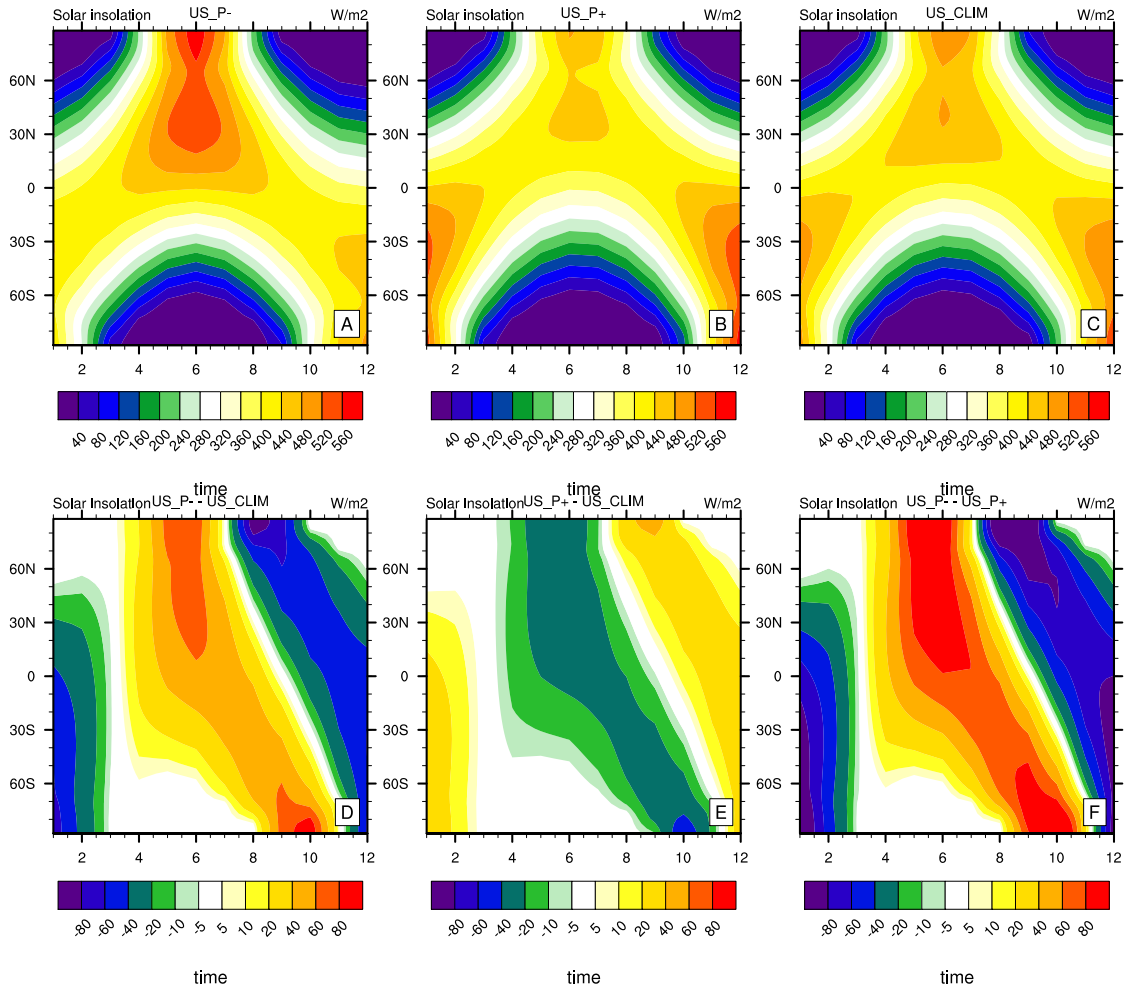
Figure 4.2: Annual cycle of zonally averaged insolation at the surface for our US precession minimum (A), precession maximum (B), and modern (C) orbital conditions. Panel D shows the difference between minimum and modern precession. Panel E shows the difference between maximum and modern precession. Panel F shows the difference between minimum and maximum precession.
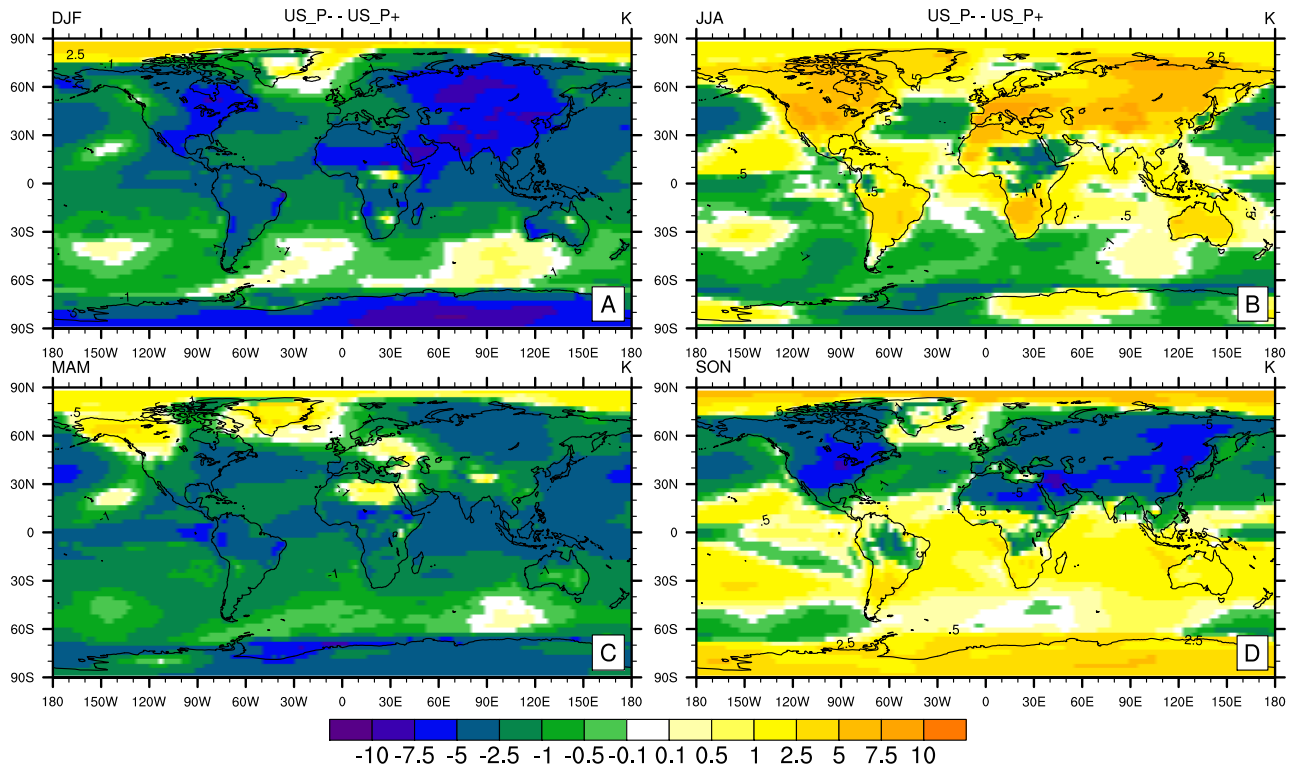
Figure 4.3: The difference in surface temperature (K) between precession minimum and maximum for our US simulation at DJF (A), JJA (B), MAM (C), SON (D).
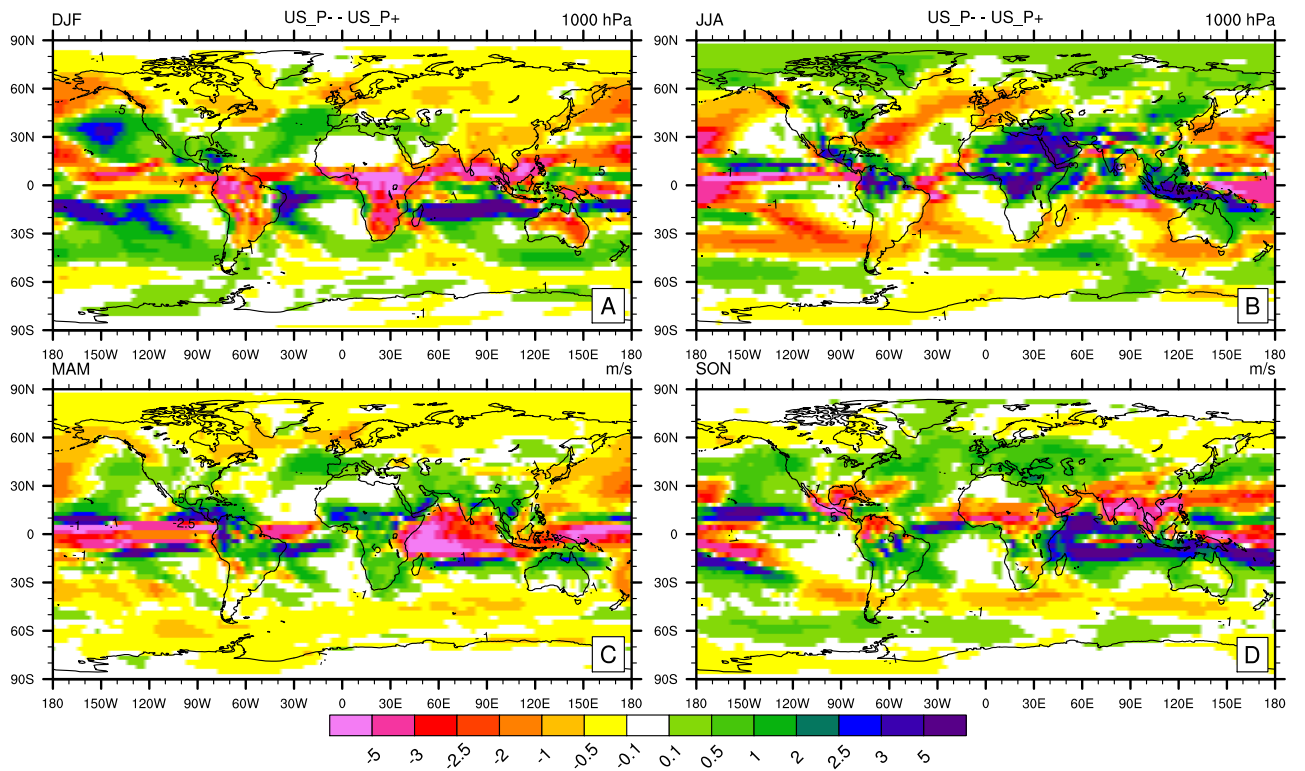
Figure 4.4: As Fig. 4.3 but for total precipitation (mm day^{-1}). Total precipitation includes both convective and large-scale precipitation.
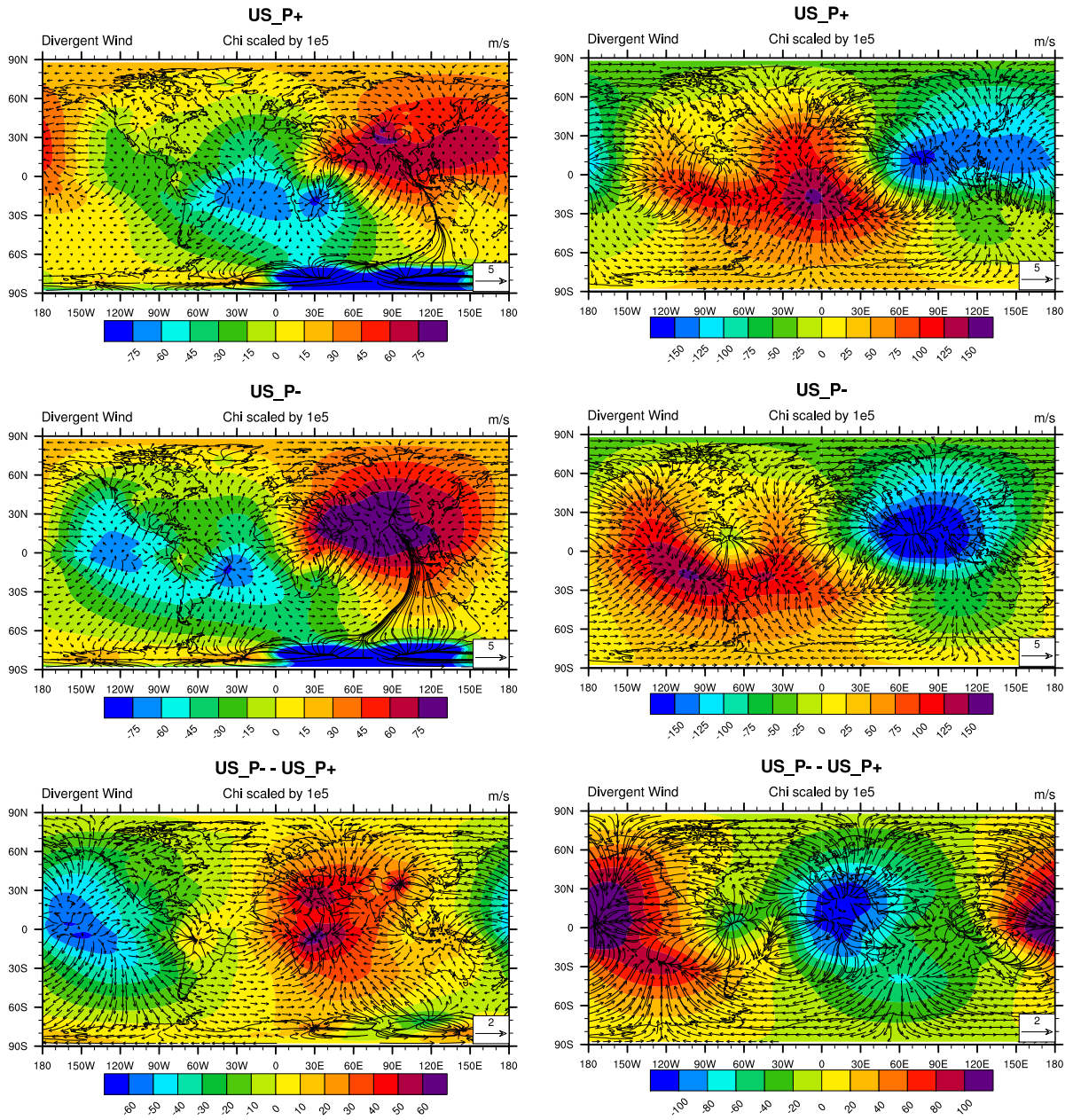
Figure 4.5: Climatological JJA Velocity potential (shaded) and wind (vectors) at 850-hPa (left) and 200-hPa (right) for our US simulation at precession maximum (top), precession minimum (middle), and the difference between precession minimum and maximum (bottom). All panels show statistically significant differences at the 95% level

Figure 4.6: The difference in annual mean precipitation (A), evaporation (B), and E-P (C) (mm day^{-1}) between our control precession minimum (US_P-) and control precession maximum (US_P+) simulations. All panels show statistically significant differences at the 95% level only.

Precipitation, Evaporation, and E-P Anomalies

(a)
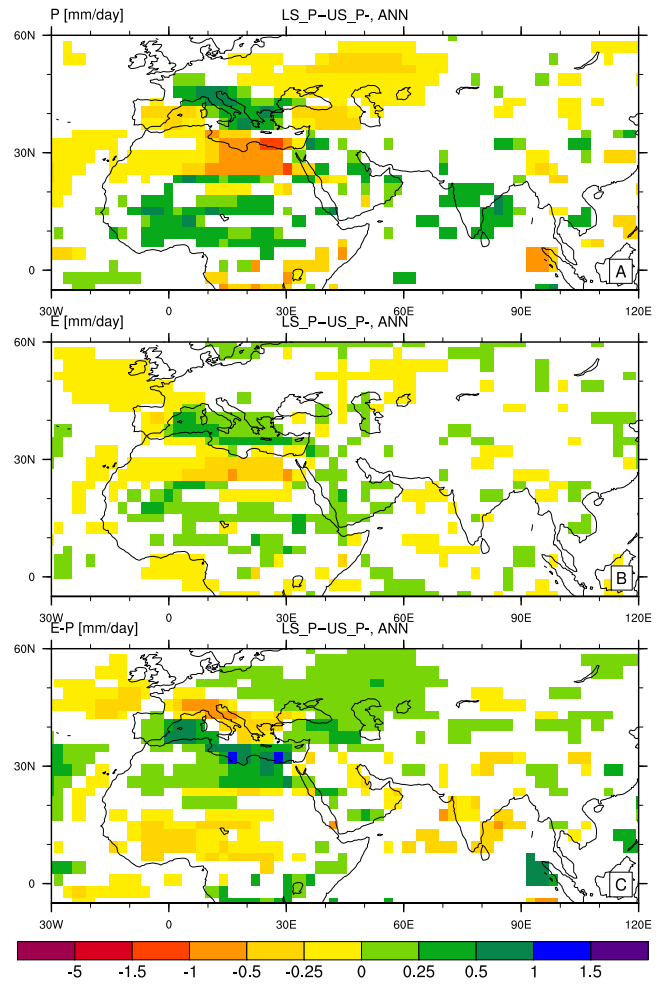
(b)

Figure 4.7: Annual mean difference in precipitation (top), evaporation (middle), and evaporation minus precipitation (bottom) (mm day^{-1}) over the Mediterranean and Southern Eurasia between the LL and US simulations at precession maximum (left) and precession minimum (right). All panels show statistically significant differences at the 95% level only.
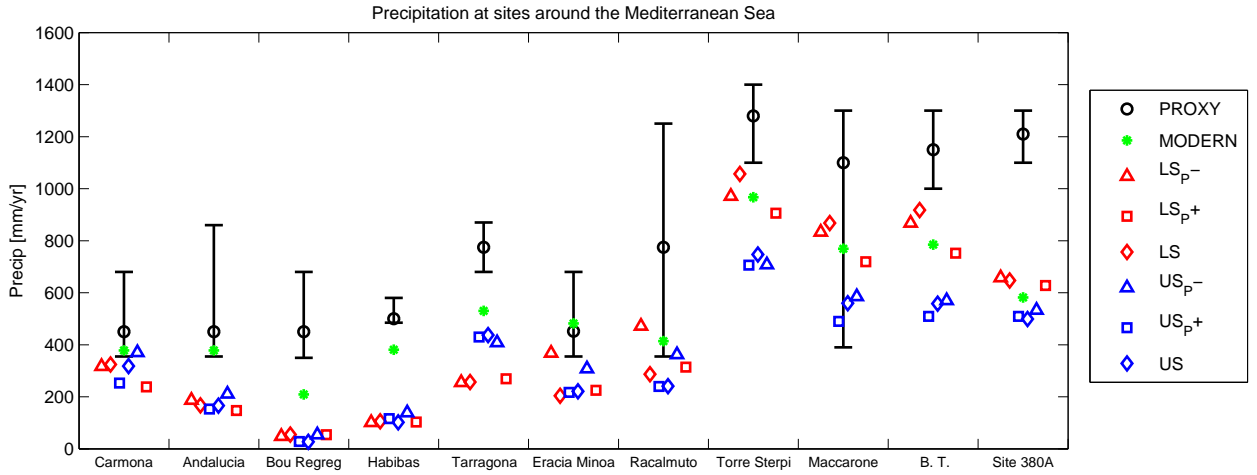
Figure 4.8: Precipitation at various sites surrounding the Mediterranean Sea. Black circles are values of precipitation from Fauquette et al. (2006). Error bars represent uncertainty in the method used to reconstruct the climate. Our LS simulations are represented with red markers and our US simulations are represented with blue markers. Present day values from the CMAP dataset are shown in green stars. Precession minimum simulations are denoted with triangles, precession maximum with squares and modern precession with diamonds.
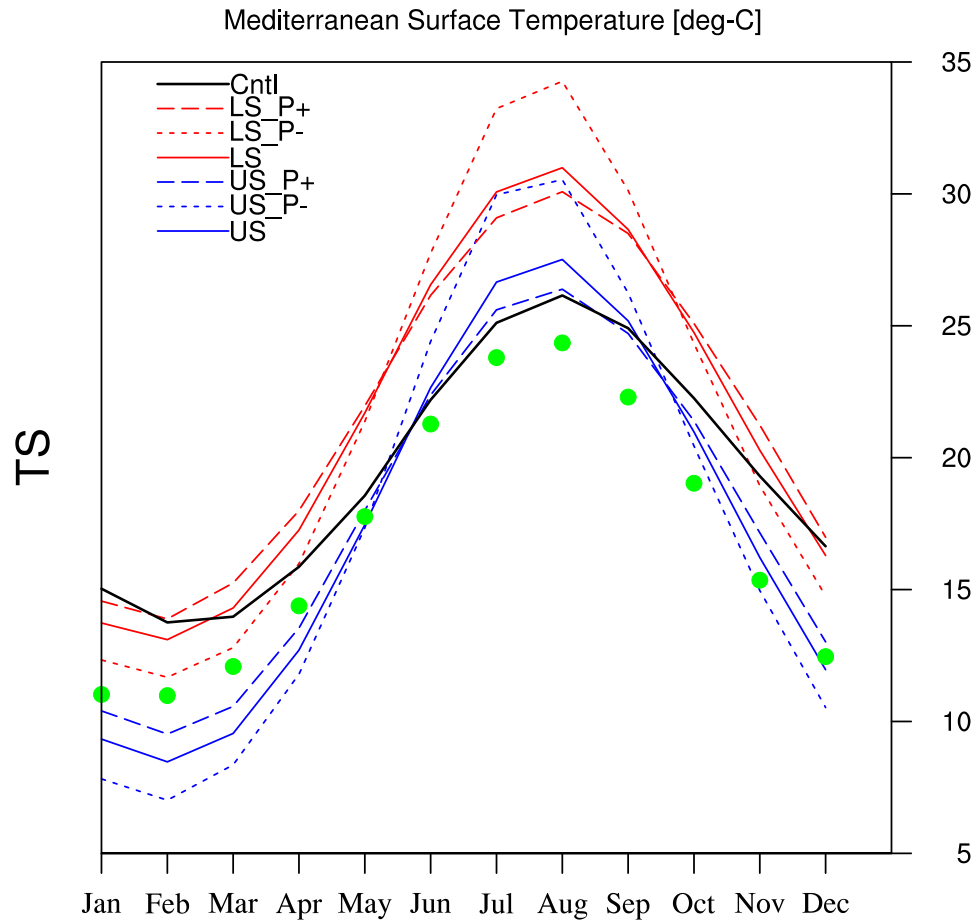
Figure 4.9: Annual cycle of surface temperature (°C) averaged over the Mediterranean Sea (6°W -37°E, 30°-46°N) for our control US (blue), a CAM-SOM control run with no Q-flux modification (Cntl) (black), and our LS simulation (red). Modern precession experiments are given in solid lines, precession minimum in small dashed lines, and precession maximum in long dashed lines. The green dots are calculated from the NCEP-NCAR reanalysis dataset.
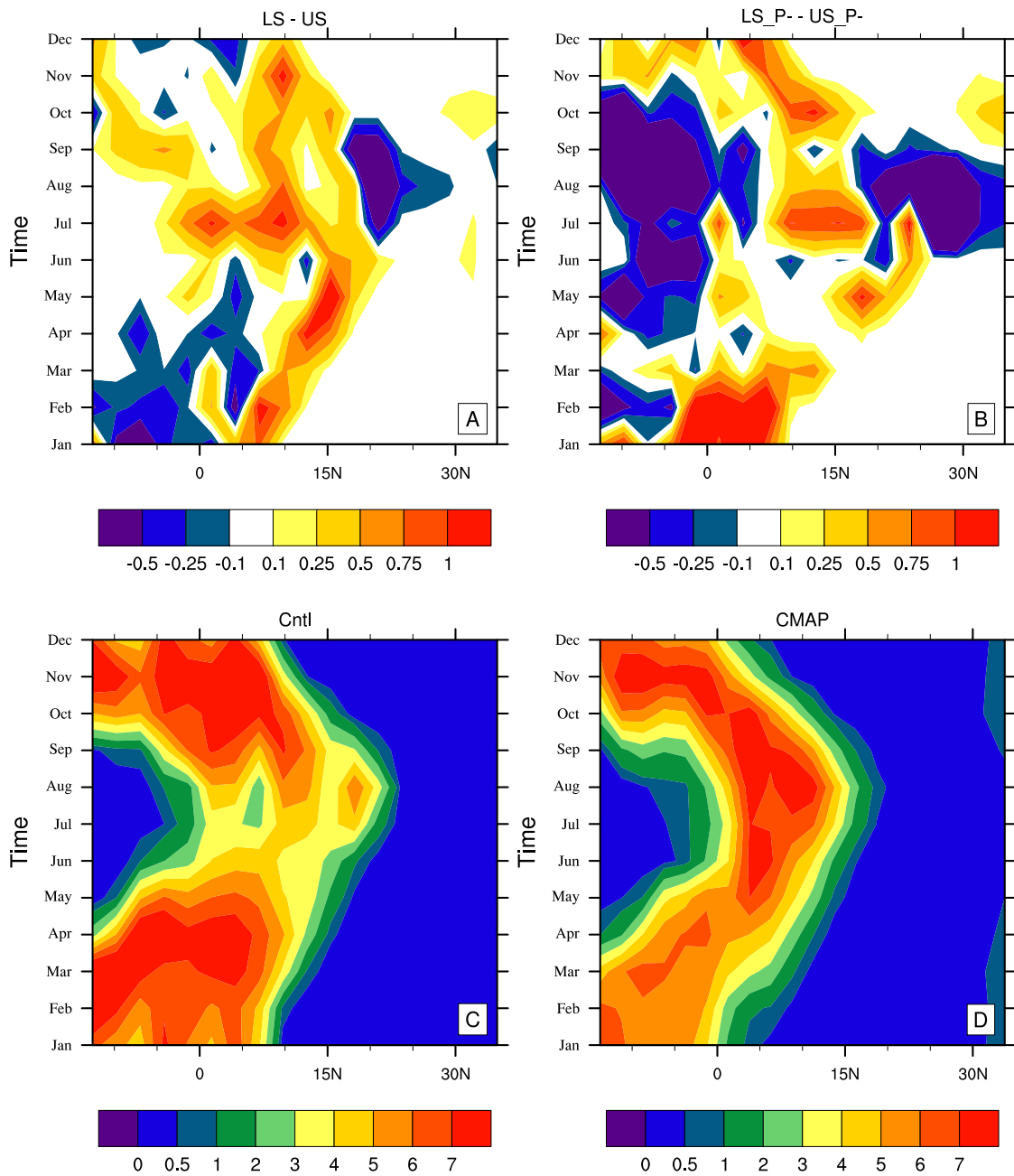
Figure 4.10: Annual cycle of precipitation (mm day^{-1}) averaged over North Africa (10°W-20°E) shown fm 10°S to 30°N. The difference between the LS and US is shown in panel A. The difference between the LS and US at precession minimum is shown in panel B. Panel C shows the climatology from the CAM-SOM Cntl simulation. Panel D shows the climatology based on the CMAP dataset.

500-hPa Omega Anomaly [Pa/s] (shaded) and 850-hPa Wind Anomaly [m/s] (vec)
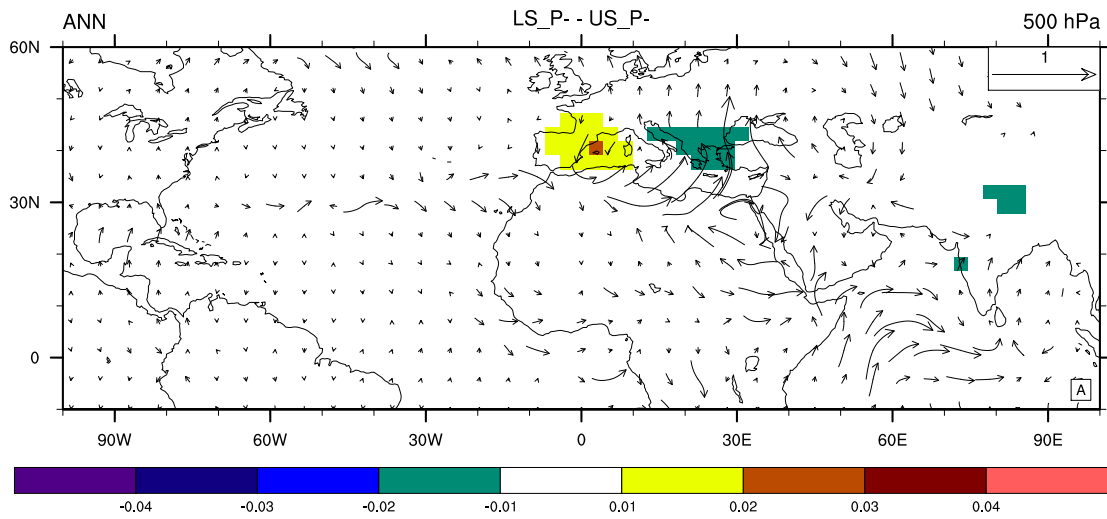
Figure 4.11: Annual mean vertical velocity (shaded) (Pa s^{-1}) at 500-hPa, and wind anomaly (vectors) (m s^{-1}) at 850-hPa over the Mediterranean and Southern Eurasia for the LS simulation. All panels show statistically significant differences at the 95% level only.
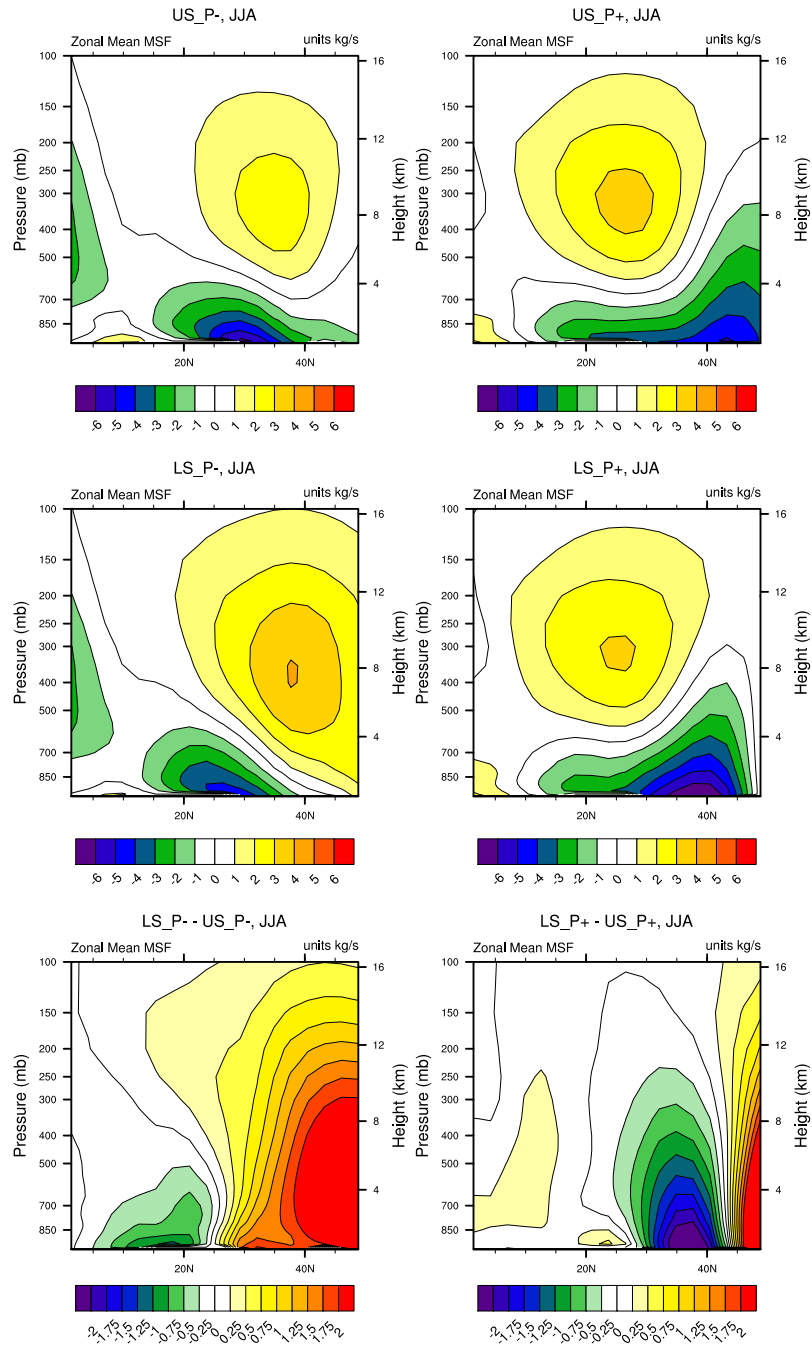
Figure 4.12: Sumertime (JJA) zonal mean meridional stream function averaged over North Africa (10°W -20°E) shown from the equator to 50°N for the US (top), the LS (middle), and the anomalies (bottom) at precession minimum (left) and precession maximum (right). Positive values represent anticyclonic, or clockwise, movement. Negative values represent cyclonic, or counterclockwise, movement.

99
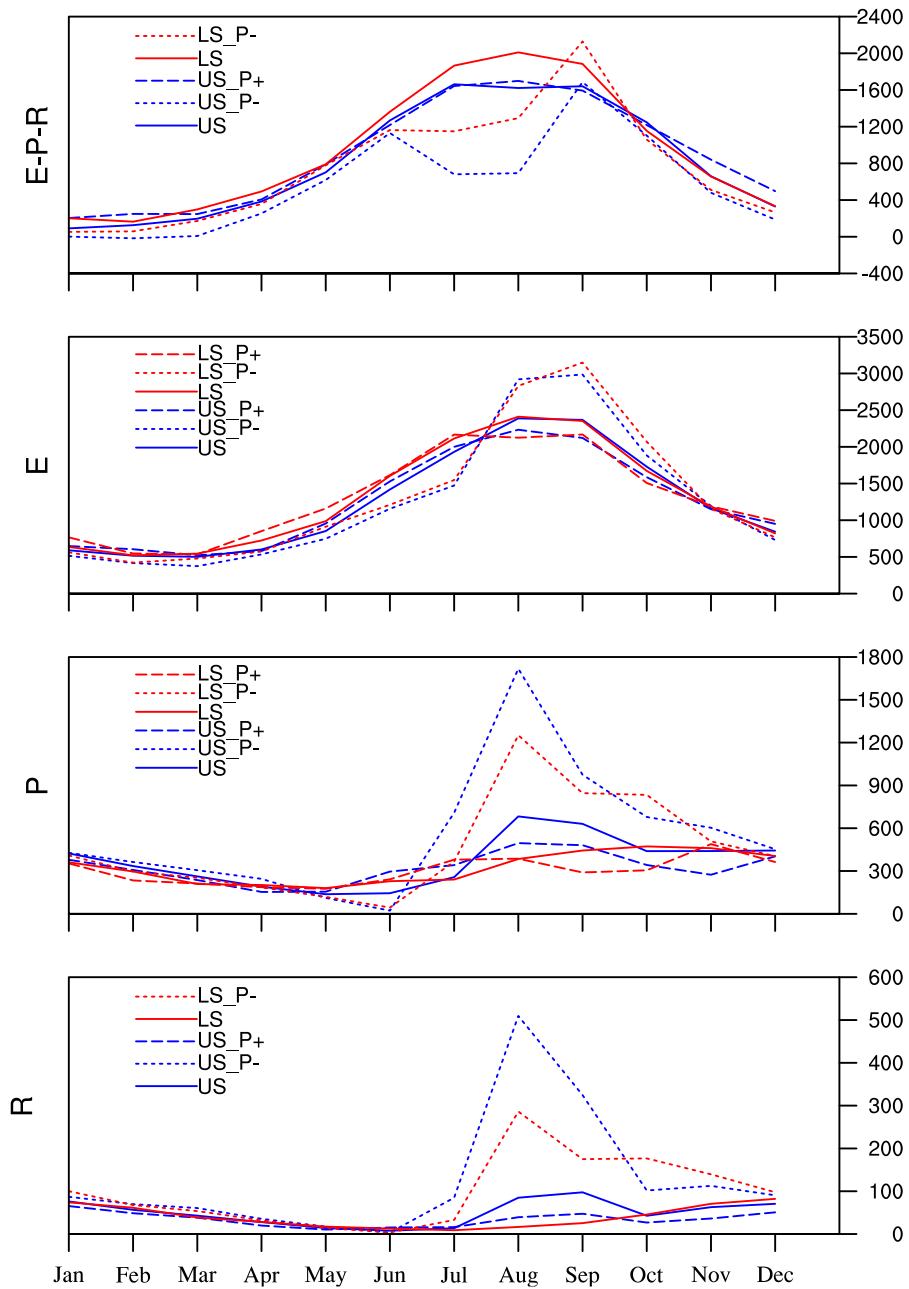
Figure 4.13: Annual cycle of evaporation-precipitation-runoff (E-P-R) (top), evaporation (second), precipitation (third), and runoff (bottom) averaged over the Mediterranean Sea (6°W-37°E, 30°-46°N) for our control US (blue) and LS (red) simulations at modern precession (solid), precession maximum (long dash) and precession minimum (short dash) simulations. The standard deviation calculated over the last 30 years of model simulation and is shown for the US simulation.
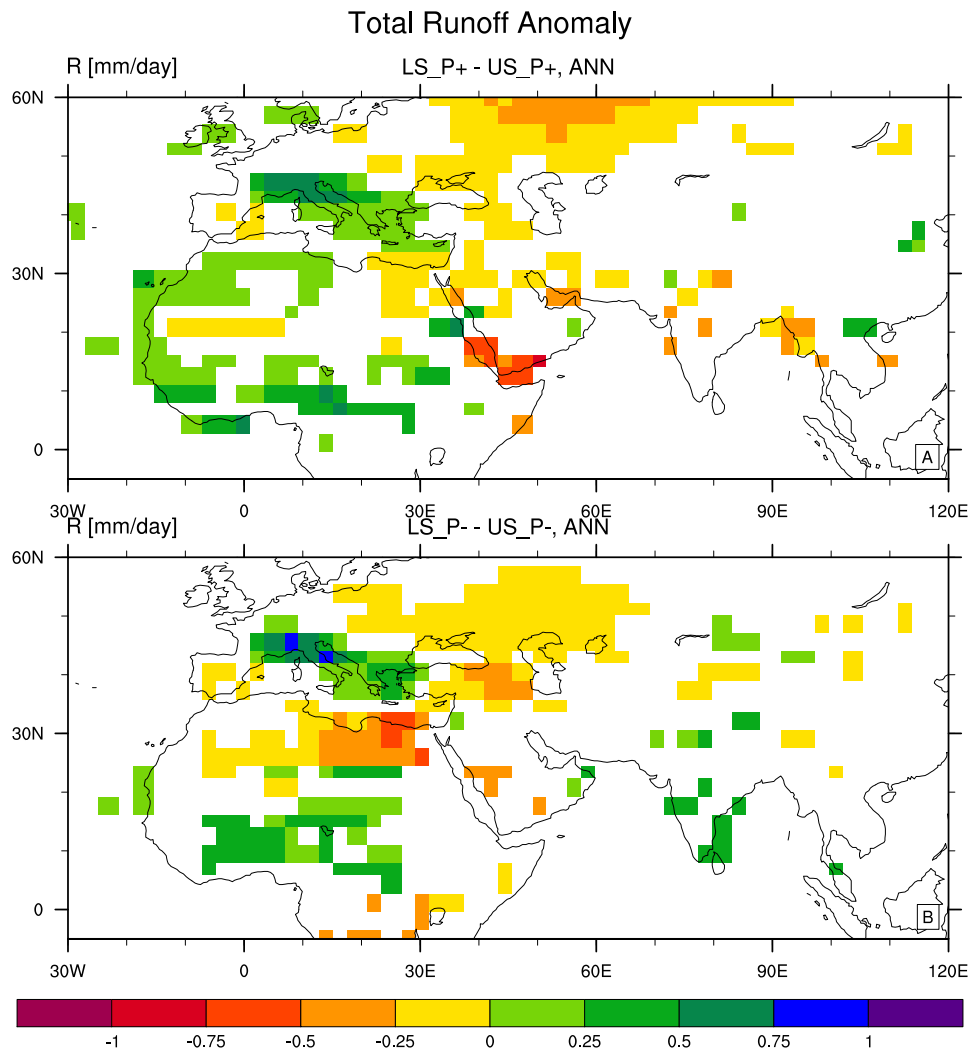
Figure 4.14: Annual mean runoff anomaly (mm day^{-1}) for the LS simulation at precession maximum (top) and precession minimum (bottom). All panels show statistically significant differences at the 95% level only.
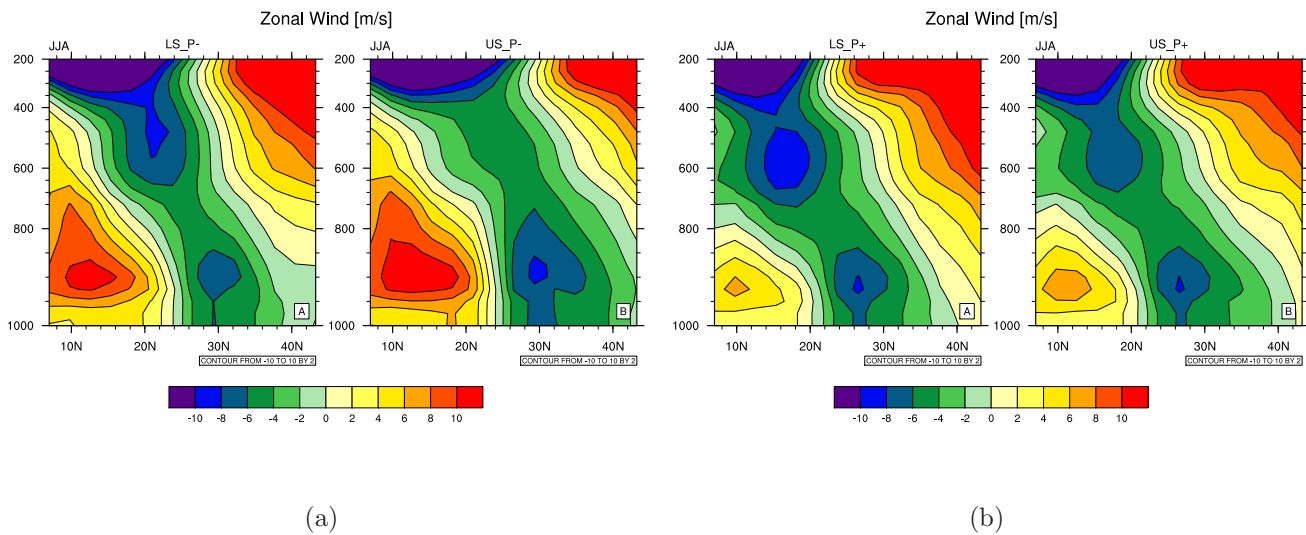
Figure 4.15: Meridional (north-south) vertical cross sections of summertime (JJA) zonal mean wind (m s^{-1}) for the LS (left) and US (right) simulations at precession minimum (a) and precession maximum (b).

Chapter 5

Dust forcing experiments

5.1 Abstract

Regional hydrological changes have important feedbacks on eolian dust sources. This may bring sizeable climate impacts from regional to hemispheric scales. Paleoclimate records indicate enhanced productivity in the Atlantic Ocean, increased aridity in Central Asia, and glaciation in the Northern hemisphere during the late Messinian. Nevertheless the mechanisms that generate such changes are still speculative. One possible source is the oceanographic isolation of the Mediterranean Sea, which resulted in substantial Mediterranean Sea level fall beginning at 5.96 Ma and desiccation with subaerial exposure between 5.59 to 5.50 Ma. We examine the role of an exposed basin on aerosols and the resulting dust feedback on climate using the NCAR Community Atmosphere Model (CAM3.1) configured with a slab ocean and coupled with an online aerosol model. Dust transport and deposition is prognostic in the model and atmospheric dust loading influences the climate system through radiative forcing. This study shows that an additional dust source from the desiccation of the MedSea may have contributed to glacial events and increased oceanic productivity shown in the geological record.

5.2 Introduction

General circulation models that implement advanced atmospheric tracer transport algorithms are capable of reproducing current patterns of dust transport and deposition (Tegen *et al.* (2002), Mahowald *et al.* (2006)). In the CCSM aerosol model it is mainly vegetation changes, not winds or soil moisture changes that will promote dust production. The ability for models to accurately simulate changes in dust deposition during the past is fundamental for evaluating climate models that are involved in future projections of climate change since hydrological changes can impact the dust cycle. Dust source regions, entrainment of dust into the atmosphere, and deposition regions are likely to change with changing climate (Mahowald et al., 2006).

In the Late Miocene, the oceanographic isolation of the MedSea resulted in substantial MedSea level fall. Consequently, the MedSea underwent a great drying episode known as the Messinian Salinity Crisis (MSC) in which it may have been desiccated for as long as 90 kyr, between 5.59 and 5.50 Ma (CIESM, 2008). The role of an exposed basin on aerosols and the resulting dust feedback on climate is an interesting aspect of the MSC. Subaerial exposure may have provided a substantial dust source area, and increased dustiness during this period may have implications on global climate through radiative forcing. Due to its proximity to a significant dust source (the Saharan Desert), precession-forced changes in dustiness are expected to impact the North Atlantic. Recent observational studies have shown that nearly 70% of the SST trend in the tropical North Atlantic is due to mineral aerosols, where reduced

dust cover warms SSTs off the coast of West Africa between 10-20°N (Evan *et al.* (2009)).

Dust radiative feedbacks alter the atmospheric circulation through changes in surface fluxes of heat and momentum. A weaker atmospheric circulation inhibits the mobilization of dust. Reduced dust mobilization means less dust is absorbed into the atmosphere, imposing a negative feedback. Atmospheric dust loading can scatter and absorb incoming and outgoing radiation, changing the local albedo and potentially cooling the surface while warming the atmosphere. Dust can indirectly affect the radiation budget through impacts on cloud properties, such as particle size and size distribution. The radiative effect of dust is still undertain (Miller *et al.* (2004)). Just as dust impacts climate through changes in radiative fluxes and optical properties, climate influences the amount, location and residence time of dust. Boundary layer mixing affects the lifetime of aerosols through changes in dry deposition. Similarly, wet deposition removes dust from the atmosphere through precipitation. Mineral aerosols may also serve as cloud condensation nuclei (CCN) and influence precipitation patterns both locally and globally. Recent studies have suggested that dust suppresses precipitation (Rosenfeld *et al.* (2001)) since a larger number of smaller particles would inhibit collision and coalescence, processes that lead to precipitation. This suggests a strong connection between dust and regional hydrological cycles. Reduced wet deposition increases the residence time of dust, and may also have a positive feedback on dust; less precipitation would lead to desertification and more dust (Nicholson (2000), Hastenrath (1990)). Atmospheric heating in the dust layer may influence convection. An examination of the effects of precession

variations and prognostic dust will provide a detailed and thorough analysis of the hydrological cycle under the different plausible scenarios during the MSC.

Jones *et al.* (2004) suggested that a climate-dust feedback mechanism may lead to more intense African Easterly Waves. The African Easterly Jet transports dust westward across the Atlantic Ocean. Dust particles contain important limiting nutrients such that deposition of dust over land and ocean may enhance photosynthetic carbon fixation. Sedimentation and deposition over the ocean may result in greater productivity since iron-laden dust particles provides this micro-nutrient to marine organisms (Jickells et al., 2005). Iron fertilization is especially important in oligotrophic (high nutrient, low chlorophyll) regions of the world ocean (Archer and Johnson, 2000). In terrestrial ecosystems, photosynthetic productivity is affected not only by climate change but also by key nutrients, such as nitrogen, phosphorus and iron, all found in dust particles.

Observational evidence suggests dust aerosols from playas containing shallow water bodies contribute significantly to the radiative effects of dust plumes (Reynolds et al., 2007). Reynolds et al. (2007) showed that lowered surfaces that contain a shallow water reservoir might contribute more dust aerosols to the overlying atmosphere because their surfaces are soft and can be easily lifted by the wind. Conversely, dry surfaces do not contribute as much dust. Topographic lows in arid regions are also important sources of dust due to the accumulation of particles that have been eroded and washed down by water or blown in by the wind (Prospero et al., 2002). Salt-rich dust aerosols from the bottom of lowered basins with a shallow layer of water contribute significantly to the radiative effects of dust plumes (Reynolds et al., 2007).

There were 18 glacial-interglacial oscillations that occurred in the Late Miocene from $\sim$6.26 to 5.50 Ma. (Hodell et al., 2001). Two prominent glacial events occurred in the Messinian Gap period when isolation of the MedSea and erosion occurred. The glacial stages during this interval were the TG12 at 5.51 Ma and TG14 at 5.58 Ma. During the TG12, $\delta^{18}O$ values exceeded the Holocene by $\sim$0.5%. Reports of ice-rafted debris off Greenland and in the Norwegian Sea suggest glaciers were large enough to reach sea level during the late Miocene (Jansen and Sjoholm, 1991; Larsen et al., 1994). In Pakistan, the $\delta^{18}O$ of soil carbonates documents increased aridity at similar to 5.5 Ma (Zhisheng *et al.* (2001)). This coincides with a peak in upwelling fauna at ODP Site 722 in the Arabian Sea.

What role would increased dust generation in the Late Miocene have on global climate? Nutrients contained in dust may enhance productivity in marine and terrestrial ecosystems, thus sequestering more atmospheric carbon dioxide and cooling global climate (Martin (1990), Okin *et al.* (2004)). Could the MSC have contributed to spikes in the $\delta^{18}O$ record? Increased biogenic blooms in the ocean may also result in changes in bio-optical heating, thus altering SSTs (Timmermann and Jin (2002)). Calcium Carbonate ($CaCO_3$) content is correlated with benthic foraminifera oxygen isotope changes, a proxy for high-latitude temperature and ice volume. The proxy record shows that diatoms that only live in sea ice were abundant in the North Pacific by 5.5 Ma (Lyle *et al.* (2008)), several million years prior to large-scale Northern Hemisphere glaciation.

If the MedSea went through several cycles of complete desiccation during the MSC, it probably became a source region for desert dust and aerosols. Proxy evidence of

aeolian dust in the eastern MedSea correlates with a northward shift in the African monsoon (Larrasoaa et al., 2003). In fact,Ruddiman and Kutzbach (1989) examined proxy data and found low dust flux records in the North Atlantic during the period of 8-5 Ma and concluded this was related to the North African wet phase. Analogously, a less humid Africa and dry Mediterranean basin would provide a substantial dust source region. A larger dust source will contribute more CCN that will be available for precipitation processes. Although this indirect effect of dust is not included in this model. Although, changes in the direct radiative forcing may implications on the water budget. An examination of the effects of precession variations and dust sources will provide a detailed and thorough analysis of the hydrological cycle under the different plausible scenarios during the MSC.

5.3   Experimental Setup

The National Center for Atmospheric Research Community Climate System Model (CCSM3) is a fully coupled atmosphere, ocean, land and sea-ice model (Collins *et al.* (2004)). For our study we use slab ocean model (SOM) and a mineral aerosol model in which dust in prognostic. The dust source mechanism and deposition is described in Mahowald et al. (2006). Modeled dust sources are typically dry regions containing strong winds, and dust sources are a function of total leaf area plus stem area index (Mahowald *et al.* (2006)). These indices are monthly mean values that are estimated from satellite data and are held fixed in all runs. When

this value is below 0.1, dust generation increases as a linear inverse function of vegetation cover. The wind friction threshold velocity increases with water content but is particle size dependent. The threshold velocity increases more quickly for smaller particles due to dielectric effects than for larger particles, which have greater mass and can easily subside. The aerosol model includes both dry and wet deposition and has a log-normal size distribution within the bins. Four separate size bins are used because of the large differences in the lifetime and optical properties of different sized particles.

While the SOM does not simulate the full ocean circulation, sea surface temperatures (SSTs) are able to respond to atmospheric changes. SSTs evolve in response to dust radiative effects (Yoshioka *et al.* (2007)). The mixed layer SOM includes a thermodynamic sea ice component and the atmosphere model uses a terrain-following hybrid coordinate with a spectral Eulerian dynamical core that has 26 vertical levels. A greater discussion on the implemented horizontal oceanic heat transport can be found in Murphy et al. (2009). The Community Land Model (CLM3) (Oleson et al., 2004) incorporates biogeophysics, hydrological cycle, and biogeochemistry. A river transport model is utilized in CLM to transport total runoff over land to the ocean; however, human water consumption and irrigation are not taken into account (Oleson et al., 2004). The vegetation is divided into plant functional types (PFT) that are characterized by its structure. The vegetation structure, including leaf and stem area index as well as canopy height, is input to each grid cell for each PFT. Greater detail of this model is provided in Collins et al. (2004) and Oleson et al. (2004).

Table 5.1 describes the additional simiulations described in this chapter. All simu-lations are run at T42 resolution (an equivalent grid spacing of roughly 2.8°x 2.8°). Branch runs were integrated from the equilibrated state of the Lowered Sea (LS) simulation described in Murphy et al. (2009). Prescribed present-day vegetation and present-day greenhouse gas concentrations are used. Several simulations were performed using restart conditions from the Lowered Land simulation in Murphy et al. (2009). We simulated the effect of a Mediterranean desert under precession maximum and minimum conditions. Since the cyclical sedimentary patterns are too frequent to account for changes in obliquity, we keep obliquity and eccentricity constant. Obliquity is held at the present day value of 23.45° while eccentricity is increased from 0.0167 to 0.05 to account for maximum seasonality in orbital preces-sion. As in Chapter 3, our LL simulations take vegetation and soil characteristics from a grid square over Northern Africa. In each of these branched simulations we now turn on dust, meaning that dust is prognostic in these new simulations. Dust alters climate through radiative effects. We run an additional simulation in which we remove dust ($LL\_P + \_NODUST$). This is done by setting the aerosol scaling factor to zero in the active radiation calculation. The difference between our desic-cated MedSea at precession maximum ($LL\_P + \_DUST$) and the simulation without dust ($LL\_P + \_NODUST$) will provide a way to calculate the dust feedback effect on the atmosphere.

5.4   Results

5.4.1   Precession-forced changes in Atmospheric Dust

In Chapter 4 we discussed the precessional effect on global precipitation, which consists of increased precipitation in the extratropics and decreased precipitation in the tropics and high latitudes during summer solstice (precession minimum orbital forcing) (Chapter 4, Figure 4). On annual time scales, a peak in precipitation occurs off the northern coast of South America. In fact, sediment traps and shelf sediments in the tropical Cariaco Basin, off the coast of Venezuela, show, in addition to a glacial-interglacial eccentricity frequency, a significant and coherent precessional relationship. According to Martinez *et al.* (2007), inorganic chemical proxies found in Cariaco sediments, namely Ti/Al, record variability in terrigenous source and/or flux, with variations corresponding to changes in the ITCZ. Increases in Ti/Al correspond to precession-induced moistening over the Cariaco Basin, which would discharge more runoff and deposit more dust (due to wet deposition), during both glacial and interglacial periods (Martinez et al., 2007). This chemical ratio is independent of eustatic sea-level variations. Orbital forcing is expected to have an impact on the atmospheric concentration of dust through associated changes in the water cycle. Precession minimum results in a strong summer monsoon that reduces the aridity of North Africa and decreases the atmospheric dust optical depth over much of the NH, with the exception of extreme Northern Africa and the eastern MedSea (figure 5.1). During this time, atmospheric dust loading is reduced over the tropical Atlantic and extending into the Caribbean. A reduction in dust deposition

(not shown) off the South American coast suggests that river input of chemical elements is more important that wet deposition of dust during periods of precession minimum forcing.

Figure 5.2 examines the anomalous changes in surface temperature due to changes in precession with prognostic dust (fig. 5.2A) and climatological dust (5.2B). Figure 5.2C shows the dust forcing on surface temperatures. While precession minimum forcing has a cooling effect on SSTs (figs. 5.2A, 5.2B), reduced dust loading over the tropical North Atlantic Ocean increases the incident solar radiation and warms SSTs north of the equator. This feature is consistent with recent studies that show dust forcing cools tropical North Atlantic SSTs, but in the opposite sense (Evan *et al.* (2009)). A classic Atlantic dipole pattern appears in anomalous SSTs, with warming north of the equator and cooling south of the equator (fig. 5.3), which has been shown to further amplify the North African precipitation signal (Braconnot *et al.* (2007)). Warmer SSTs enhance evaporation, which shifts the ITCZ northwards and produces more precipitation, particularly in the western tropical North Atlantic. Paleo-monsoon studies, in particular the Paleoclimate Modelling Intercomparison Project (PMIP), have recently shown that vegetation feedbacks may be less important for rainfall over Africa (Braconnot et al., 2007), yet these studies use models with seasonally-prescribed dust based on modern climatology. Our results suggest that dust may damp ocean and vegetation feedbacks. This emphasizes the role dust has on the tropical hydrological cycle and suggests that among vegetation and ocean-dynamical feedbacks, we must also take into account dust-radiative feedbacks in paleo-studies of the monsoon. Reduced precipitation in the equatorial Pacific ex-

acerbates the double ITCZ problem that is inherent in the CAM (Hack et al., 2006).

5.4.2   Dust deposition and optical depth

Figure 5.4 shows the annual mean dust deposition for our desiccated Med-Sea simulations (panels A), our control simulations (panels B) and the difference between the two (panel C) for precession maximum orbital forcing (left) and precession minimum orbital forcing (right). The anomalous dust optical depth illustrates the contribution of annual mean atmospheric dust loading from a MedSea contribution source. The annual zonal mean dust optical depth is plotted to the right of each panel. The top panels show a second dust peak at 35°N. Atmospheric dust loading from a MedSea dust source forced with precession maximum is almost as large as the Saharan source, which is evident at 18°N. Table 5.2 gives the global and NH annual mean dust optical depths for each simulation. Our control simulations are within the range of values given in Mahowald *et al.* (2006). Using the SOM, Mahowald gives a global dust optical depth value of 0.037, which is consistent with our value of 0.039 for the US_P-_DUST simulation. Precession maximum results in greater dust loading. Dust fluxes are correlated with the global ice volume: typically, a reduced hydrological cycle and stronger atmospheric circulation during glacial periods result in a dustier atmosphere (Rea (1994)). Precession maximum orbital forcing results in less insolation during NH summer, which reduces sea-ice melt, while stronger insolation in the winter increases evaporation. Greater moisture transport and pre-

cipitation leads to more ice buildup.

The annual mean NH dust optical depth is increased from 0.09 in our control (US_P+_DUST) to 0.14 under desiccated conditions (LL_P+_DUST). Under precession minimum orbital forcing, the Mediterranean dust source becomes larger than the Saharan. This is consistent with wetter conditions in North Africa. The annual mean NH dust optical depth is increased from 0.07 in our control (US_P-_DUST) to 0.11 under desiccated conditions (LL_P-_DUST). Our results show that a Med-Sea desert doubles the global annual mean dust optical depth compared to control conditions. Considerably higher dust optical depth values occur over the Northern Hemisphere in the summer, with positive values over the eastern North Pacific Ocean. High values of dust optical depth occur over central and eastern Asia in the spring and summer. Deep Sea Drilling Project Site 397, located near 27°N off the northwest Africa coast, records moderate-sized dust influx maxima between 6 and 5.5 Ma (Stein (1985)).

5.4.3   Dust Radiative Forcing

To determine the radiative forcing of dust in our simulations, we run our model for one year, turning on the passive aerosol radiative forcing calculation. This allows us to obtain aerosol forcing factors. Figures 5.5 and 5.6 show the shortwave radiative forcing of dust at the top of the atmosphere (A), within the atmosphere, and at the surface for precession minimum (fig. 5.5) and precession maximum (5.6)

forcing. Dust radiative forcing reduces the solar flux at the surface and top of the model over most of the NH. A large reduction of more than 40 W m^{-2} is found over North Africa. Our precession maximum simulations show stronger dust radiative forcing at high latitudes compared to precession minimum. This is the result of a > 60% increase in atmospheric dust loading.

5.4.4   Climate Response

5.4.4.1   Temperature

Local changes in aerosol cover may affect temperature via the scattering of sunlight and reduction in surface solar radiation. This is shown over the Med-Sea and North Africa where greater dust loading significantly decreases insolation. Although we would expect surface cooling due to greater reduction of incident insolation, the dust results in warming: Figure 5.7 shows the anomalous change in surface temperature resulting from a Mediterranean desert with prognostic dust (fig. 5.7A), climatological dust (fig. 5.7B), due to a Mediterranean dust alone (fig. 5.7C), and due to all dust in the model (fig. 5.7D). In our model dust has a lower albedo than the bright, desert surface. More dust loading over the desert leads to more absorbed solar radiation, which increases the surface temperature. Without dust in the atmosphere, the desert surface reflects more solar radiation.

Outgoing longwave radiation (OLR) is a function of surface temperature. However, dust and clouds tend to reduce the OLR from clear sky values. In Murphy

et al. (2009), reduced Mediterranean sea level raises the surface temperature due to adiabatic compression, resulting in a 20 W m^{-2} increase in OLR compared to control conditions. Dust loading when the MedSea produces dust acts as a blanket inhibiting OLR from escaping into space. Greater dust loading reduces the annual mean outgoing radiation by 10 W m^{-2} over the MedSea and North Africa. These competing effects depend on the cloud type, cloud water content, surface albedo. Locally, the surface temperature is increased because the trapping of OLR by dust dominates over the reduction in insolation due to increased albedo.

5.4.4.2   Precipitation

Changes in convective precipitation are mostly confined to the tropics, where strong localized latent-heat release in ascending air plays a bigger role in precipitation processes than large-scale systems. Figure 5.8 shows the difference in total precipitation between the desiccation simulations and the control for our prognostic dust (figure 5.8A), and climatological dust (figure 5.8B) simulations. Figure 5.8C shows the anomalous total precipitation attributed to dust from the MedSea, and figure 5.8D shows the effect of all dust. Increased heating from dust drives a stronger circulation from the Atlantic to North Africa resulting in increased precipitation along the Guinea Coast during precession maximum. Figures 5.8C and 5.8D show that dust shifts tropical precipitation into the Southern Hemisphere. Namely, there is a shift in convective precipitation into the Southern Hemisphere. Shifting

of the ITCZ leads to a decrease in high cloud amount and an increase in OLR in the tropical North Atlantic. Figure 5.8D shows that dust results in drying over the Sahel. This is consistent with theories that increased dustiness plays a fundamental role in the Sahel drought (Brooks and Legrand (2000)). Greater atmospheric dust loading and westward advection across the Atlantic Ocean decreases precipitation over northern South America, including most of the Amazon.

A MedSea dust source results in a drier Asia (figure 5.8). The Red-Earth Formation, located in Central China, was formed between 22-2.6 Ma and has long recorded the history of aridification in central Asia. Since ∼6.2 Ma, aeolian dust deposition is recorded at the central Loess Plateau the existence of deserts in the Asian interior. According to Zheng *et al.* (2004), the North Pacific and the Red Clay Formation at Jiaxian show moderately enhanced dust input values during the interval between about 5 and 7 Ma ago, reflecting a period of increasing aridity in Central Asia. Aridity was intense between ∼6.2–5 Ma and weaker from ∼5–3.6 Ma, coinciding with a decline in sediment accumulation rates in the Indian Ocean between 5.5–4 Ma in the Indian Ocean. This suggests the MSC may have contributed to Asian aridification in the Late Miocene.

A MedSea desert leads to a further reduction in precipitation regionally during precession minimum (figure 5.9). Continental heating during precession minimum is enhanced due to the warming effect of dust. This is consistent with a stronger circulation in the tropical Atlantic and Indian Oceans and into Africa (figure 5.10). When this anomalous westerly current reaches the East African mountains, orographic lifting results in a precipitation maximum. Increased precipitation over eastern North

Africa is only significant (at the 95% confidence level) in our prognostic dust runs. The moisture comes from the Atlantic, and not the MedSea as suggested by Griffin (2002). Our results suggest that heating from increased atmospheric dust loading during summer solstice allows circulation changes that support a wet phase over northeastern Africa. In the Indian Ocean, increased advection towards warm Africa results in less precipitation over India (figure 5.9C).

Under all orbital conditions, lowering the MedSea level leads to drying over Eastern Europe due to a reduction in large-scale precipitation, attributed to the poleward advection of dry, dust-laden air from the MedSea. Eastern Europe is drier in our P-runs compared to P+ (figure 5.8 and figure 5.9, respectively). This is in agreement with pollen data from Western Bulgaria that shows an abrupt change during the MSC. This change is represented by a sharp decrease in woody taxa and spreading of drier and more open vegetation. An opening of vegetation is correlated with a decrease in mean annual precipitation (Utescher et al., 2009).

5.4.4.3   Northern Hemisphere sea-ice cover

With the exception of desert surfaces, atmospheric dust reduces the surface temperature of the NH. Cooling is accentuated over the high latitudes, where surface temperature is reduced more than 1.5°C. Reduced MedSea level results in extratropical stationary waves evident in the anomalous geopotential height pattern that resembles an annular mode. A MedSea dust source contributes to even greater cool-

ing over the high Arctic. This is due to the development of a strong low-pressure system, and reduced geopotential heights at 250-hPa (figure 5.11) over the Arctic that prohibits heat transport, cooling the region, and resulting in greater sea-ice production (figure 5.12). Figure 5.11C shows the new geopotential height pattern due to dust forcing. Stationary extratropical waves are excited by the tropical response to the dust change. Our calculation of the dust radiative forcing suggests greater cooling over the Arctic at P+ compared to P- because of a substantial increase in dust at mid-latitudes. Precession minimum conditions leads to higher pressure over the North Atlantic Ocean and lower pressure off the coast of Greenland (figure 5.13). This advects more heat into the Norwegian Sea, resulting in warmer temperatures and reduced sea-ice formation (figure 5.14). Figure 5.15 (taken from Hodell et al., 2001) shows that two prominent glacial events (TG12 and TG14 denoted with red arrows), took place during the Messinian gap. Our results suggest that NH cooling due to a higher dust concentration during the MSC may have contributed to increased sea-ice formation in the Arctic.

5.5 Discussion

In northeastern Brazil, the Sahel and other semi-arid tropical regions, vegetation has a strong feedback on climate through radiative and hydrological effects. Our results show that dust decreases precipitation over the Amazon and northern South America due to a southward shift in the ITCZ. However, Okin *et al.* (2004)

suggests that nutrients in Saharan dust deposition over the Amazon sustains long-term productivity, a feature that is not included in our model. Enhanced dustiness during the Pliestocene, a period of global cooling and arid conditions, may be one feature that sustained the Amazon rainforest when climate conditions would favor dieback. Greening of the Sahara under precession minimum forcing would further act to reduce dust loading, suggesting amplification in the dust-hydrological cycle feedback response.

Strontium (Sr) isotopes record both the rate of weathering and provenance of the weathered material. The production rate of carbonates is also linked to the Sr cycle as S^{+2} readily subsititutes for Ca^{+2} in the production of marine carbonates, which is a primary sink for the element from seawater (Lyle et al., 2002). Sr/Ca ratios of coccolithophores may be affected by paleoproductivity and therefore have recently been used as a proxy for paleoceanographic changes. Sr/Ca ratios suggest increased productivity in the western Tropical Atlantic during the late Miocene (Billups *et al.* (2004)). The partition coefficient for benthic foraminifera, D_{Sr}, is positively correlated with rates of organic carbon fixation and calcification. D_{Sr} shows a large peak at the end of the Messinian at the northern edge of the Brazilian shelf, known as the Ceara Rise (King *et al.* (1997)). Increased atmospheric dust transport across the North Atlantic during the Messinian gap may result in increased productivity along this region. The peak is at the end of a slow rise since the beginning of the late Miocene that has been attributed to increased weathering and nutrient input to the ocean following the vertical uplift of Tibet.

The Mg/Ca ratio of foraminiferal shells is a proxy for past temperature change.

Benthic foraminiferal accumulation rates (BFAR) are considered to be a good proxy for export paleoproductivity. Lange and Berger (1993) suggest the increased occurrence of radiolaria and echinoids off the equatorial West African coast between 5.8 Ma and 5.25 Ma indicates either an increase in productivity or a temporary intrusion of silica-rich water masses. Typically, peaks in radiolaria occur during warm periods indicated in the δ^{18}O record. However, one peak occurs at around 5.7 Ma during a cold stage. In the Indian Ocean, ODP Site 721, located off the coast of Saudi Arabia, shows broad maximum in sedimentation rates and % $CaCO_3$ at 5.6 Ma, while BFAR derived paleoproductivity shows a distinct maxima at 5.8 Ma (Diester-Haass et al., 2006). Our results suggest that an additional MedSea dust source in the Late Miocene may have contributed to increased productivity in these regions at this time.

Guo *et al.* (2004) found evidence of greater aridity in Central China between 6.2 and 5 Ma. From 6 to 5.5 Ma, Atlantic Deep Sea Drilling Project Site 397, located on the African continental shelf at 27°N, shows a maximum in mass accumulation rates and moderate-sized dust influx maxima. Stein (1985) suggests this is a result of north Saharan aridity and an intensified atmospheric circulation. On the contrary, the record shows south Saharan humidity (Tiedemann *et al.* (1989)). Our results favor increased humidity in the Sahel and sub-Saharan North Africa when the MedSea level is reduced. The effect of dust on this region leads to more arid conditions.

We have shown that MedSea level has a significant impact on Northern Hemisphere sea-ice formation. At reduced MedSea level, sea ice growth spreads southward, especially in the Labrador and Bering Seas. Interestingly, Wolf and Thiede (1991) found

discontinuous sea-ice cover in the Labrador Sea to the south of Greenland since the late Miocene times, a few million years prior to Northern Hemisphere glaciation. Significant tidewater glacial effects occurred between 6 and 4.2 Ma. Proxy data indicates that ice-rafting began by 5.5-6.0 Ma in both the northwest Pacific and Gulf of Alaska sites (Krissek (1995)). ODP Site 881 ($\sim$48°N,162°E) lying just outside the Sea of Okhotsk shows a peak in mass accumulation rates of coarse sand-sized IRD at 5.5 Ma. This site is within the zone of southward advancing sea ice in our LL_P- simulation.

5.6 Concluding remarks

This study has examined the influence of the MSC on climate during the Late Miocene Messinian Gap period. This study shows that an additional dust source from the desiccation of the MedSea may have contributed to glacial events and increased oceanic productivity shown in the geological record.

Precession-minimum orbital forcing reduces the aridity of North Africa. Modeling the dust source and transport changes in response to decreased dustiness shows that warmer tropical North Atlantic SSTs attributed to increased insolation in the absence of dust enhances evaporation and favors more precipitation over the western tropical North Atlantic. This stresses the importance of allowing dust to respond to climate change and including prognostic dust in paleo-simulations that examine changes in the tropical hydrological cycle. Enhanced dust loading over the tropical

North Atlantic Ocean occurs when the Mediterranean is desiccated. This reduces the net radiative flux at the surface, which cools SSTs north of the Equator and shifts the ITCZ towards the Southern Hemisphere, consistent with theories that links African dust with extended Sahel droughts. Greater ocean productivity results from nutrient rich iron-laden dust waters, which is consistent with increased benthic foraminiferal accumulation rates off the African coast between 5.8 Ma and 5.25 Ma. The dustier Northern Hemisphere inhibits convective precipitation in the tropical North Atlantic and large-scale precipitation over Eastern Europe and into Central Asia, in agreement with proxy evidence of greater aridity in in these regions. Our results show that a desiccated Mediterranean has a significant impact on Northern Hemisphere sea-ice formation during precession maximum, which agrees with d18O proxies. Sea ice growth spreads southward, especially in the Labrador Sea, Bering Sea and Sea of Okhotsk. Interestingly, proxy data studies show discontinuous sea-ice cover from the Labrador Sea to the south of Greenland, and concurrent ice-rafting in both the northwest Pacific and Gulf of Alaska sites in the late Miocene, a few million years prior to Northern Hemisphere glaciation

5.7 Tables

Table 5.1: Description of the acronyms used for the simulations described in this article.

MedSea level	Prognostic Dust	Climatological Dust	No Dust
Upper Sea P-	US_P-_DUST	US_P-_CLIM	
Lowered Land P-	LL_P-_DUST	LL_P-_CLIM	
Upper Sea P+	US_P+_DUST	US_P+_CLIM	
Lowered Land P+	LL_P+_DUST	LL_P+_CLIM	LL_P+_NODUST

Table 5.2: Annual mean dust optical depth averaged over the Northern Hemisphere and the global.

Simulation	$US\_P - \_DUST$	$US\_P + \_DUST$	$LL\_P - \_DUST$	$LL\_P + \_DUST$
NH mean	0.074	0.090	0.114	0.142
Global mean	0.039	0.047	0.059	0.073

5.8   Figures

Dust Optical Depth in visible Anomaly [None]
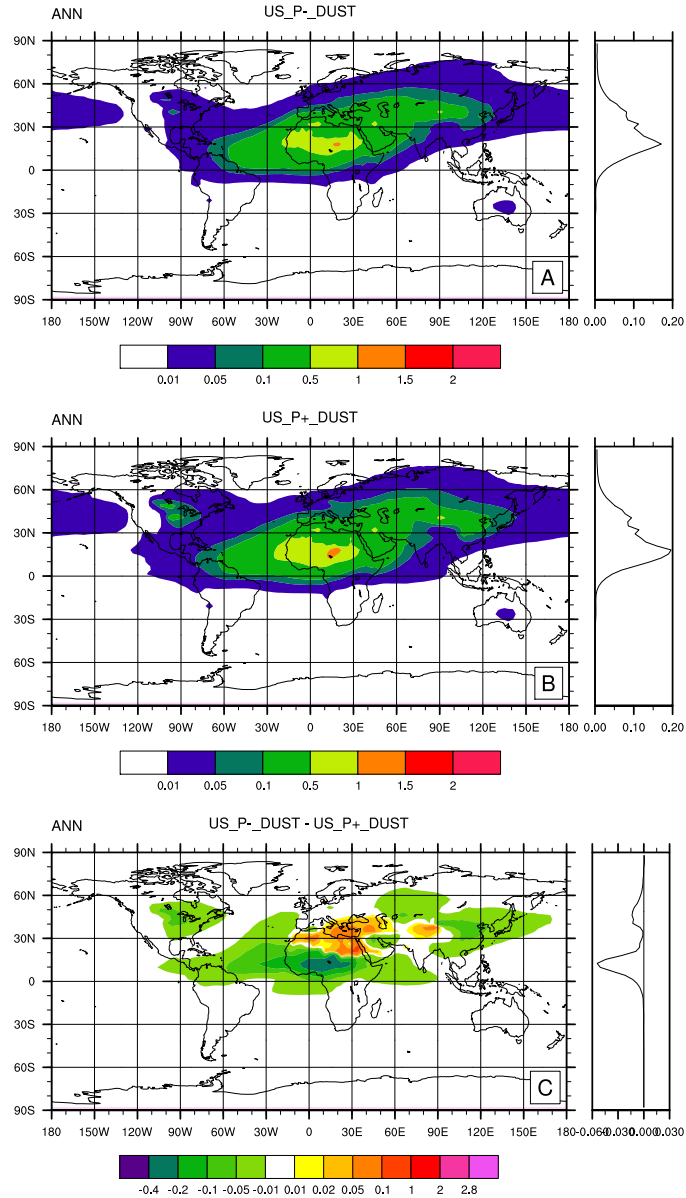
Figure 5.1: The difference in annual mean dust optical depth between our control precession minimum (US_P-_DUST) and control precession maximum (US_P+_DUST) prognostic dust simulations. A zonal mean plot is attached to the right edge of the map.
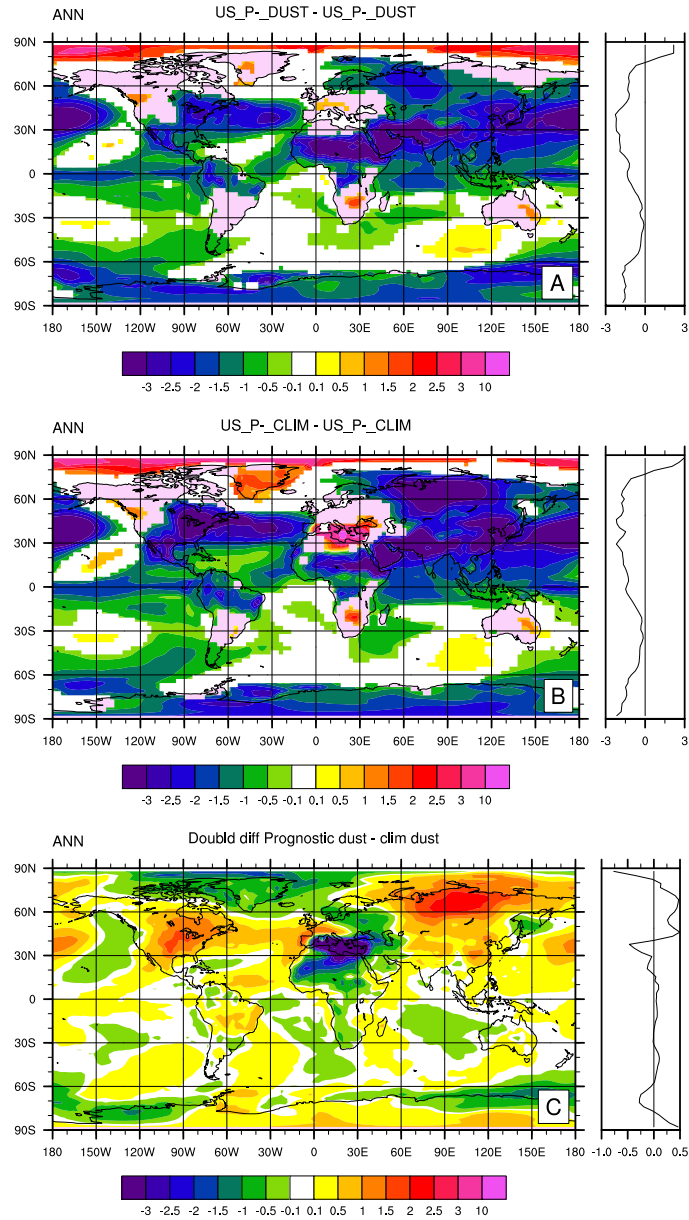
Figure 5.2: Panel A gives the difference in annual mean surface temperature (K) between our US_P-_DUST and US_P+_DUST prognostic dust simulations. Panel B gives the difference in annual mean surface temperature (K) between our US_P-_CLIM and US_P+_CLIM simulations with a dust seasonal cycle based on present-day climatology. Panel C shows the difference between panel A and panel B, which is the difference between our prognostic dust and climatological dust simulations. A zonal mean plot is attached to the right edge of each map.

Figure 5.3: As Fig. 5.2 but showing total precipitation (mm day^{-1}). Total precipitation includes both convective and large-scale precipitation.
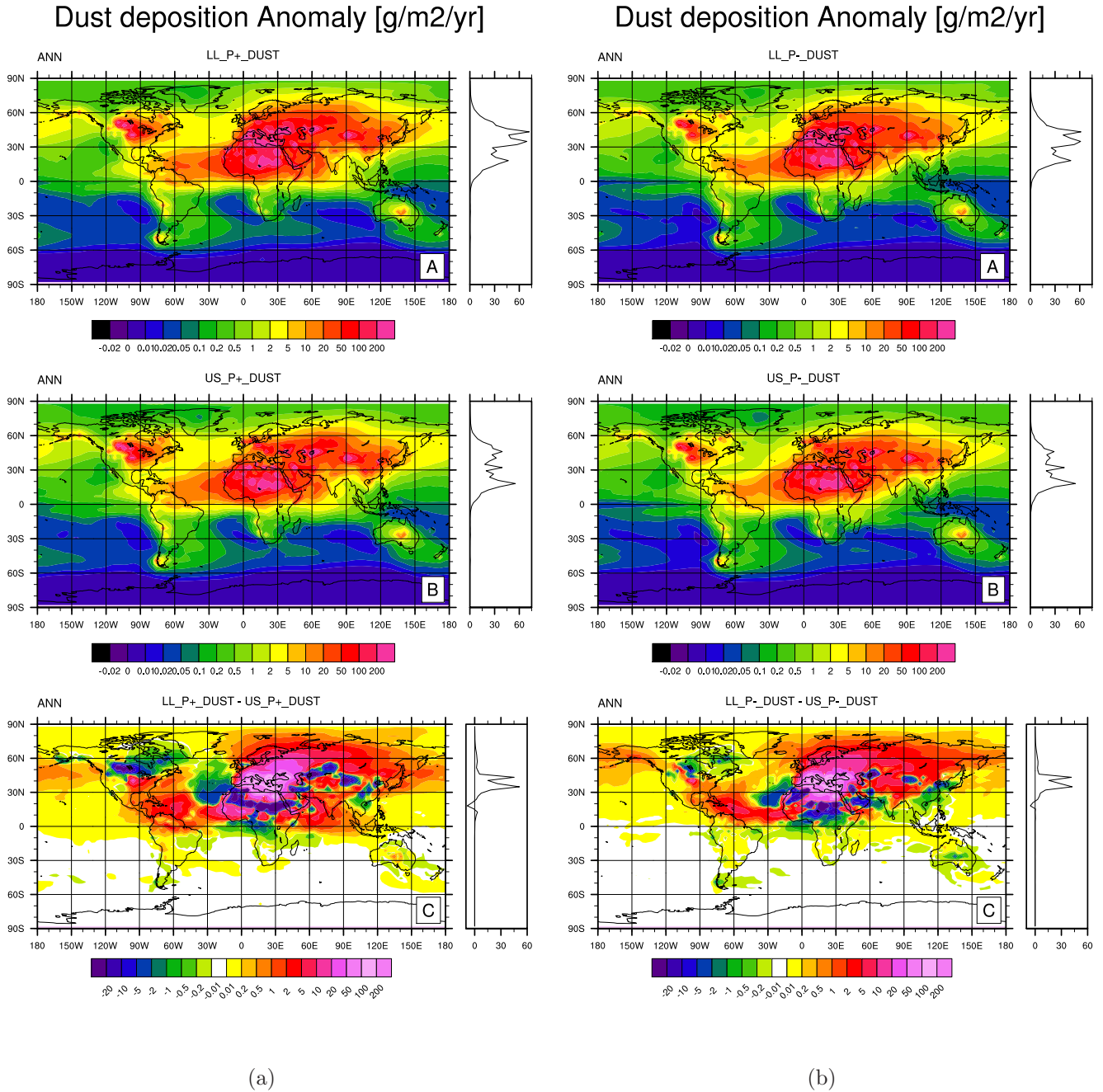
Figure 5.4: Annual mean dust deposition anomaly for the LL (panel a, top) and US (panel b, middle) simulations at precession maximum (left) and precession minimum (right). The difference in annual mean dust deposition between our LL and US simulations at precession maximum (panel C left) and precession minimum (panel C right). All panels show averages for our prognostic dust simulations. A zonal mean plot is attached to the right edge of each map.
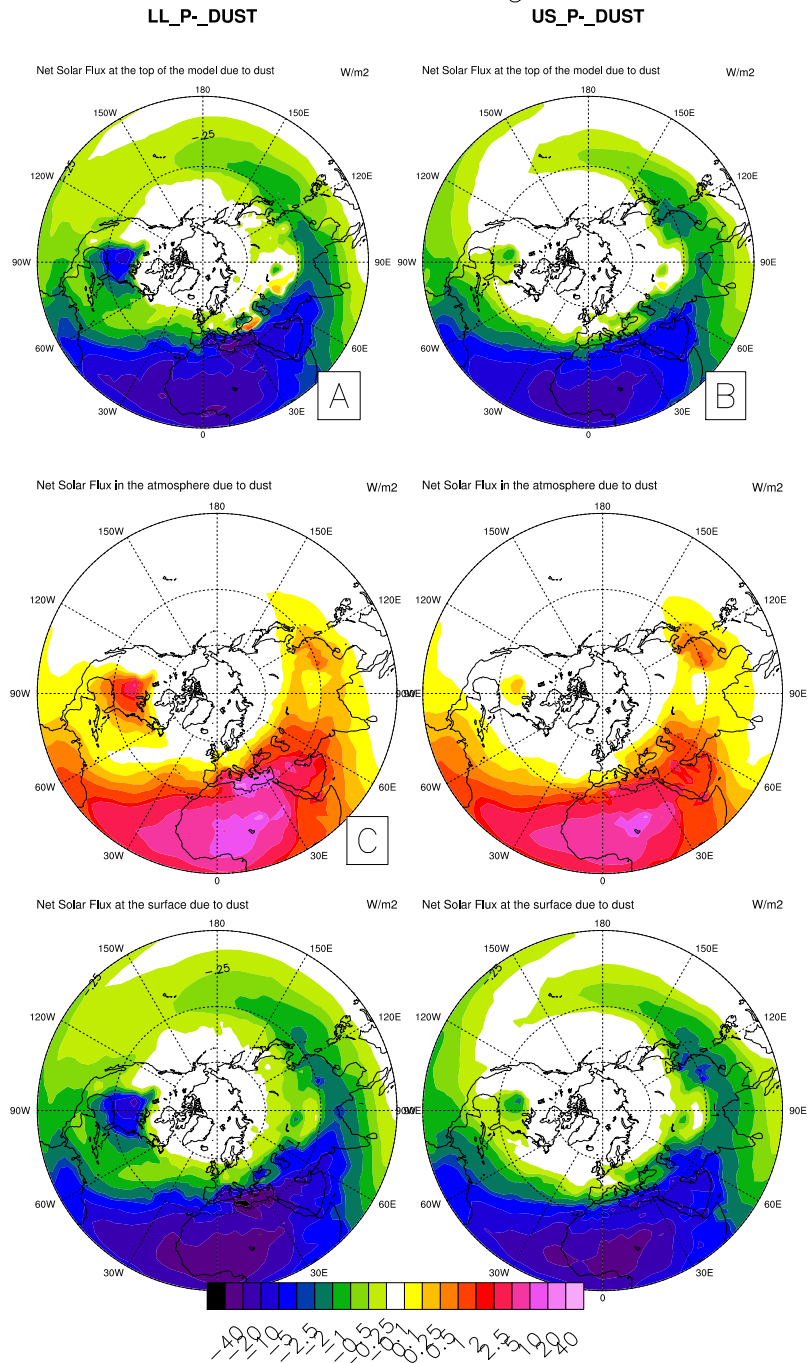
Figure 5.5: The DJF seasonal mean shortwave radiative forcing of dust for the top of the atmosphere (top), middle of the atmosphere (middle) and surface (bottom) at precession minimum. The LL prognostic dust simulations are shown on the left and the US prognostic dust simulations are shown on the right.

SW Radiative Forcing of Dust

LL_P+_DUST   **US_P+_DUST**
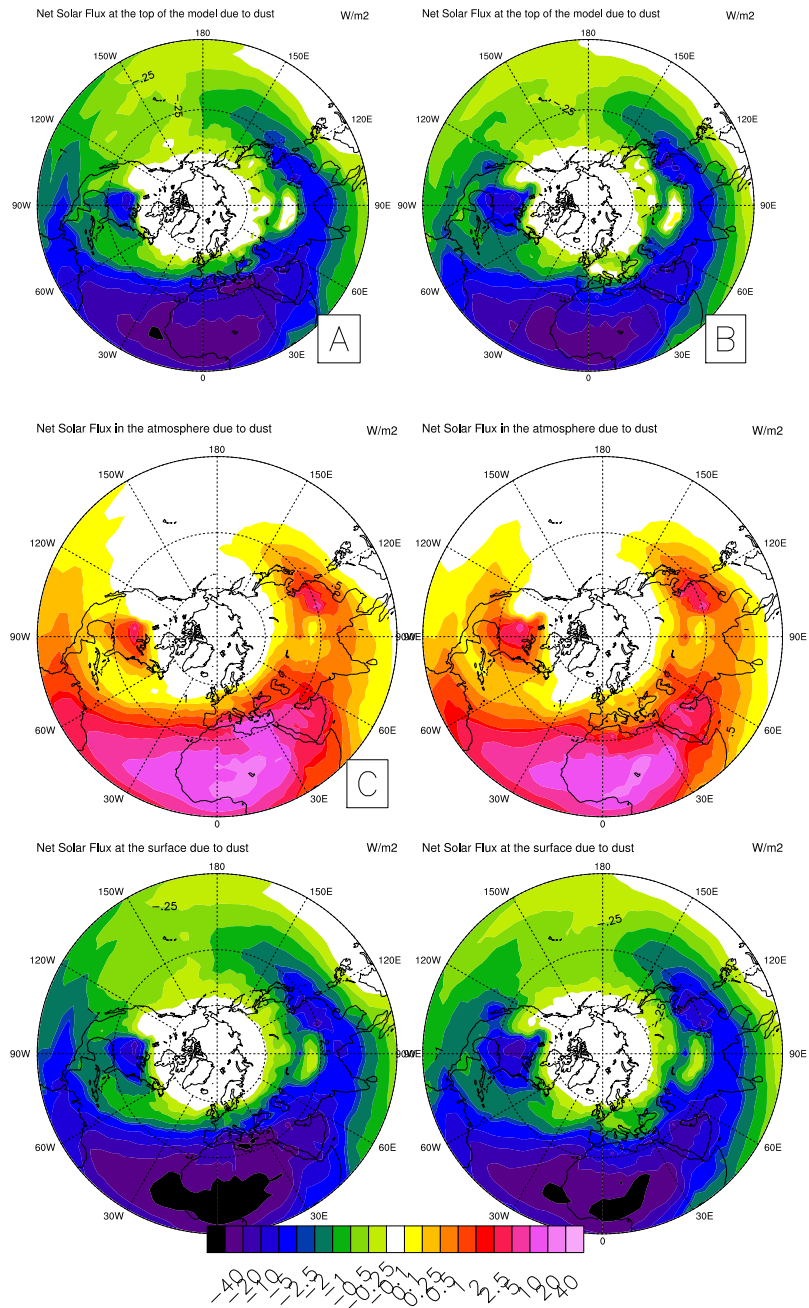
Figure 5.6: As Fig. 5.5 but for precession maximum.
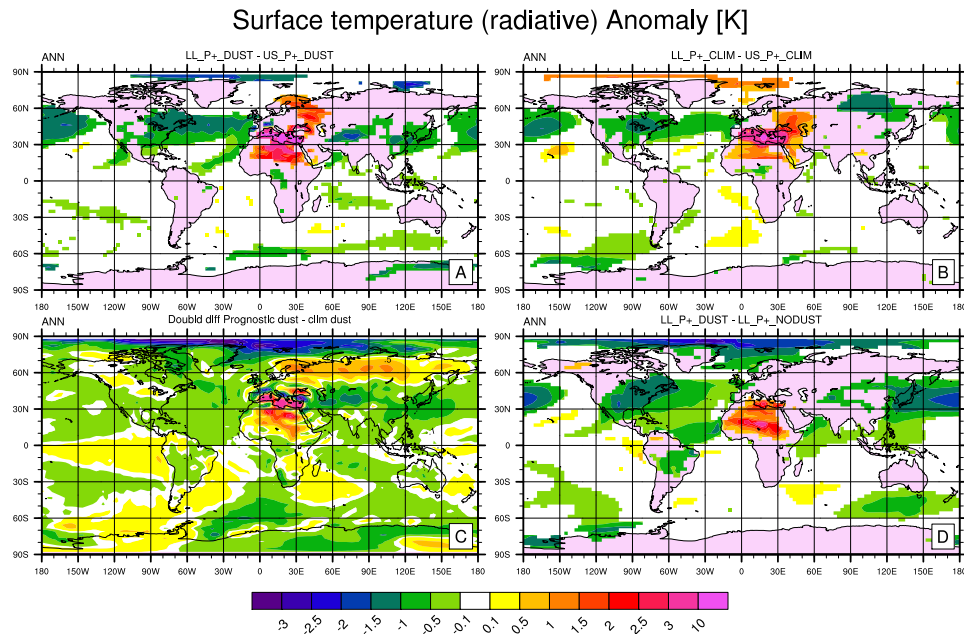
Figure 5.7: Annual mean surface temperature anomaly (K) at precession maximum for the prognostic dust (A), climatological dust (B), and the double difference (C). Panel D shows the difference between our LL prognostic dust (LL_P+_DUST) and our LL no dust (LL_P+_NODUST) simulations, showing the effect of all dust.
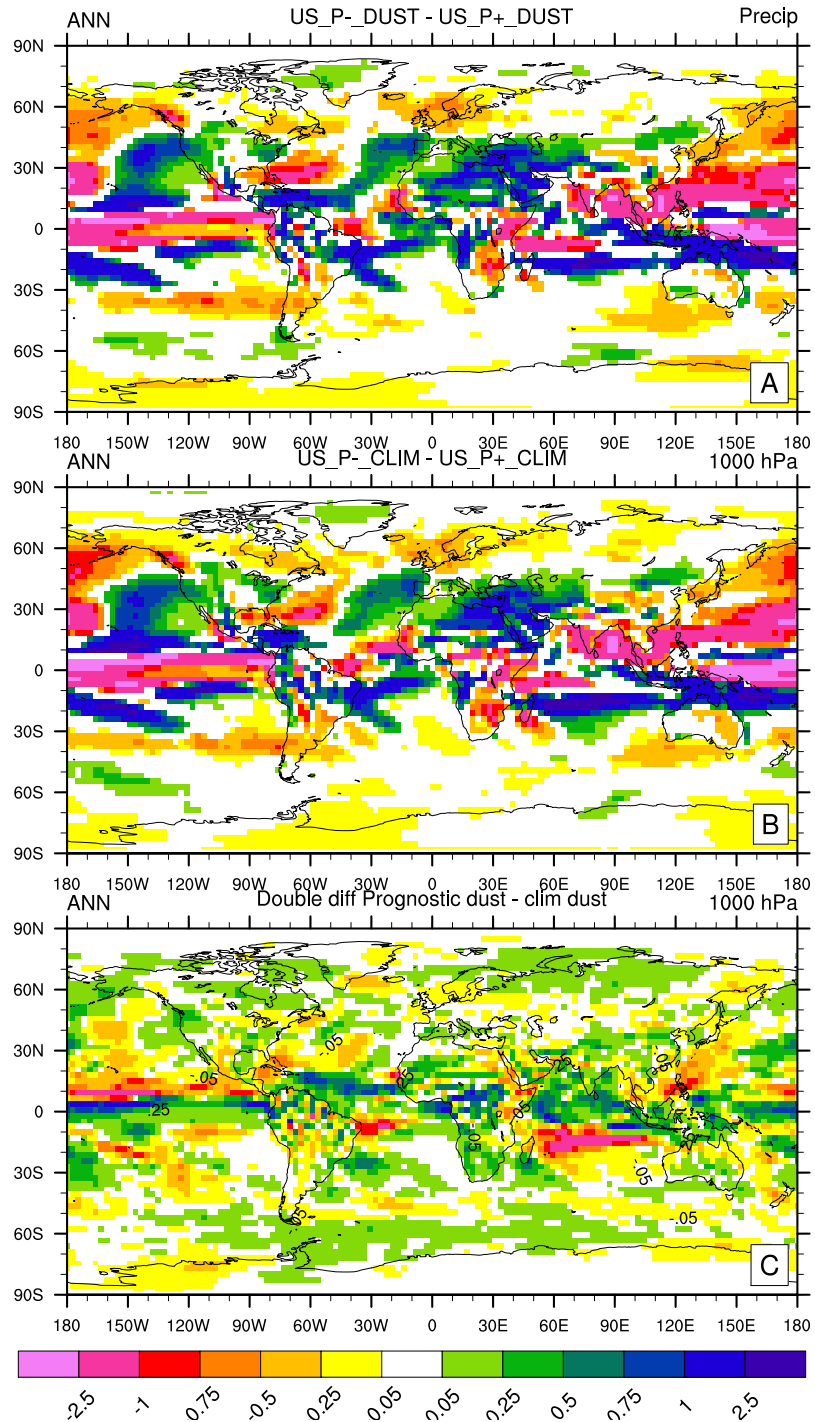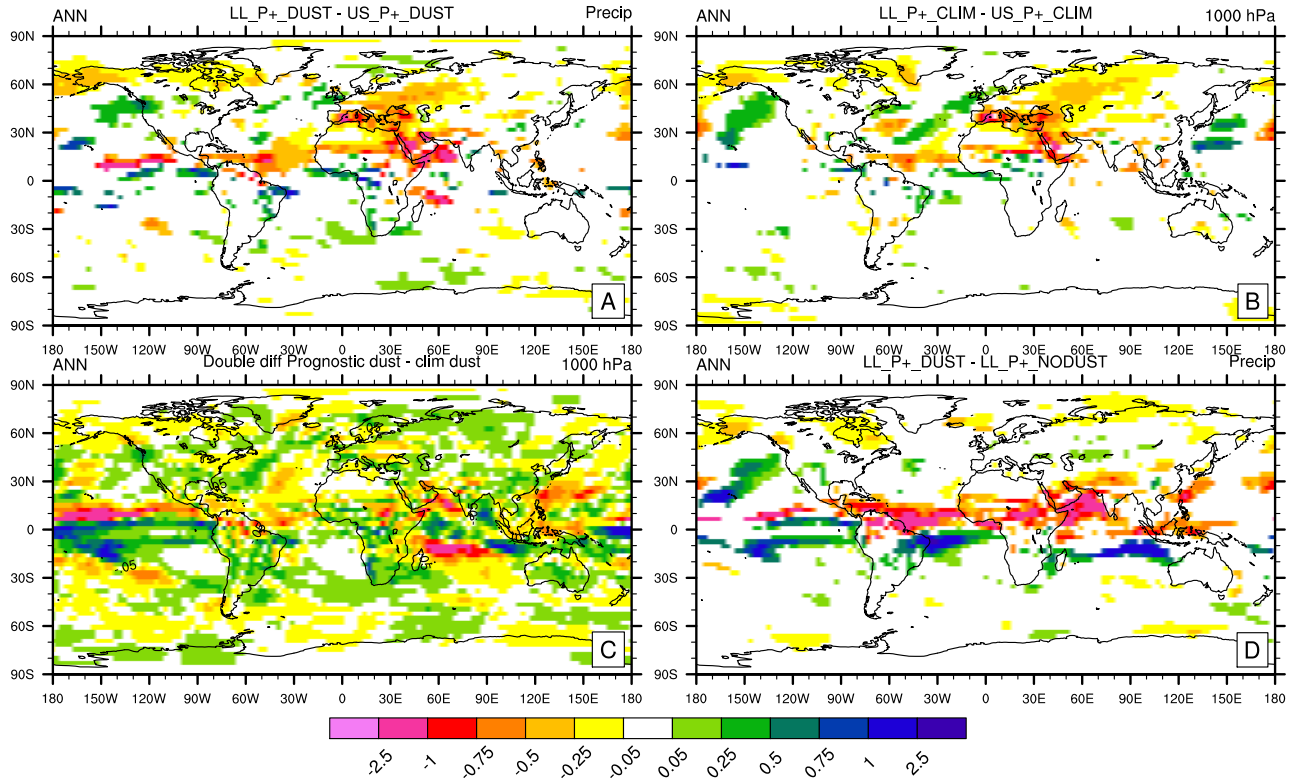
Figure 5.8: As Fig 5.7 but for total precipitation (mm day^{-1}). Total precipitation includes both convective and large-scale precipitation.
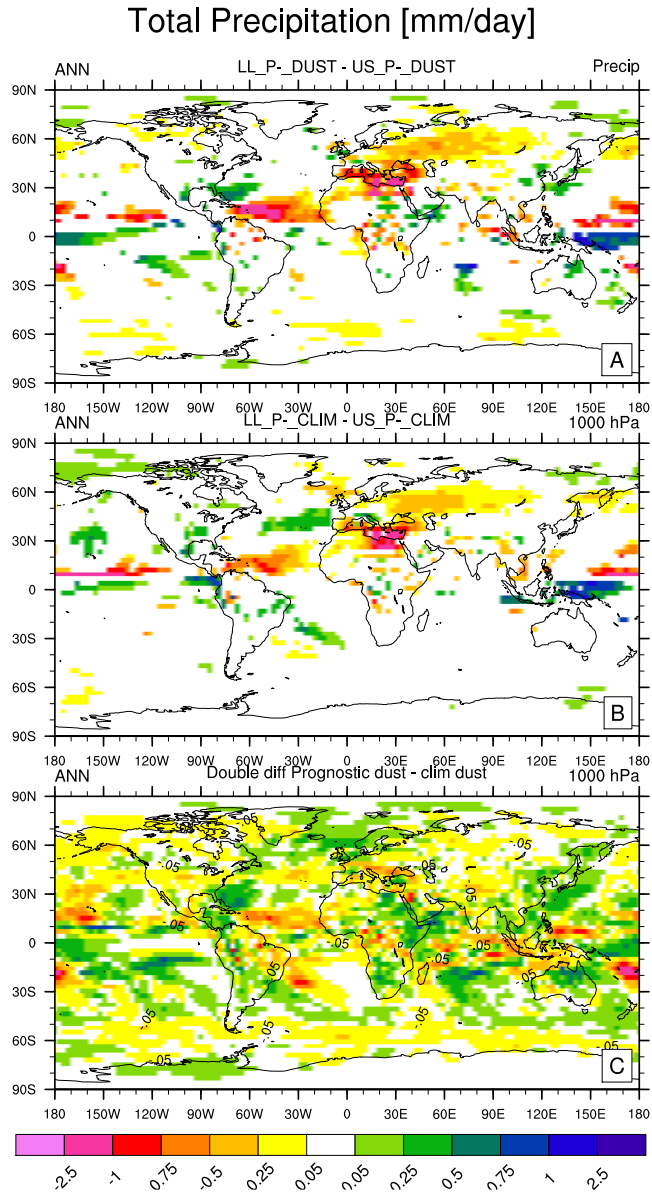
Figure 5.9: The difference in annual mean total precipitation (mm day^{-1}) between our LL and US simulations at precession minimum. Total precipitation includes both convective and large-scale precipitation. Panel A shows the difference for our prognostic dust simulations. Panel B shows the difference for our climatological dust simulations. Panel C shows the difference between panel A and panel B, which is the difference between our prognostic dust and climatological dust simulations. This double difference effectively shows the effect of dust.
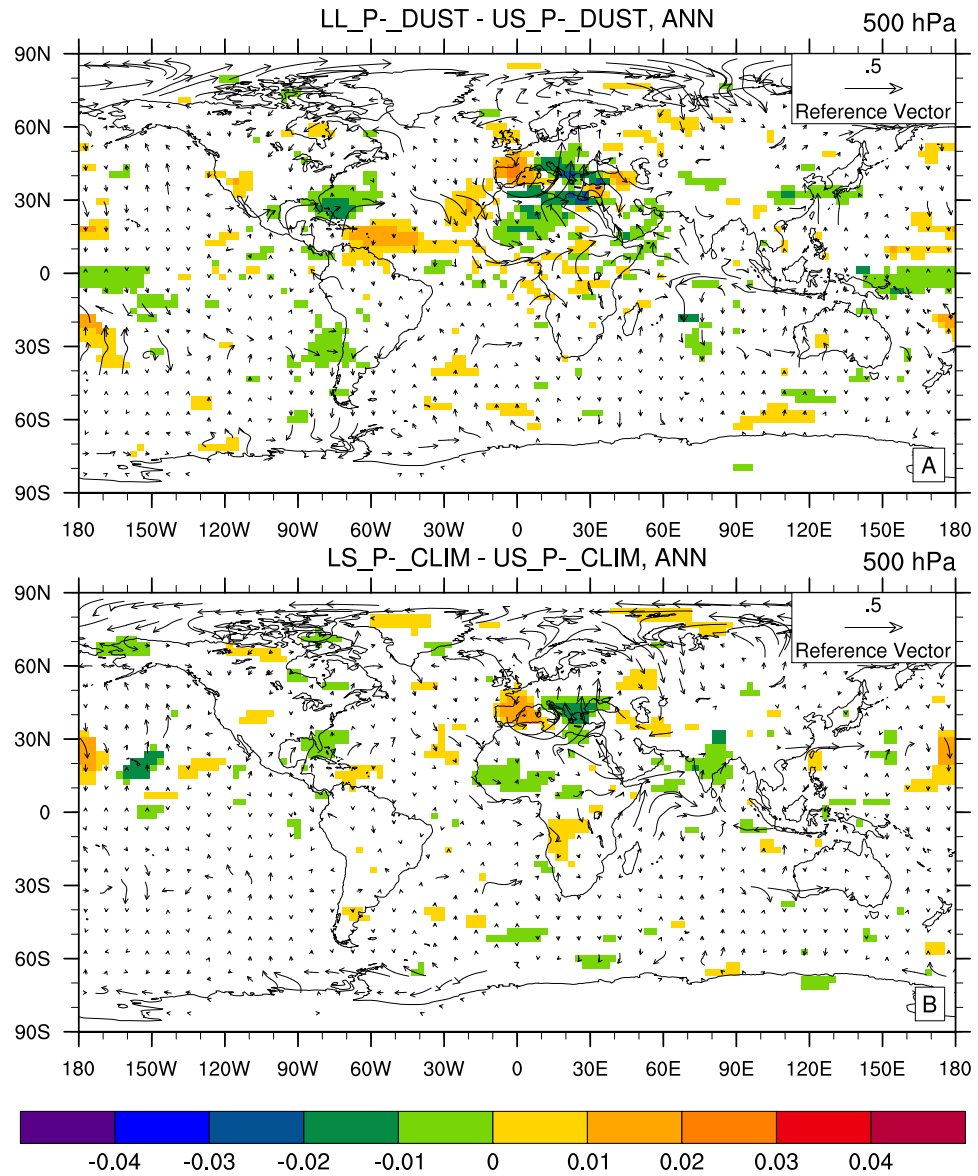
Figure 5.10: Annual mean vertical velocity (shaded) (Pa s^{-1}) at 500-hPa, and wind anomaly (vectors) (m s^{-1}) at 850-hPa at precession minimum for the prognostic dust (top) and climatological dust (bottom) simulations. All panels show statistically significant differences at the 95% level only.
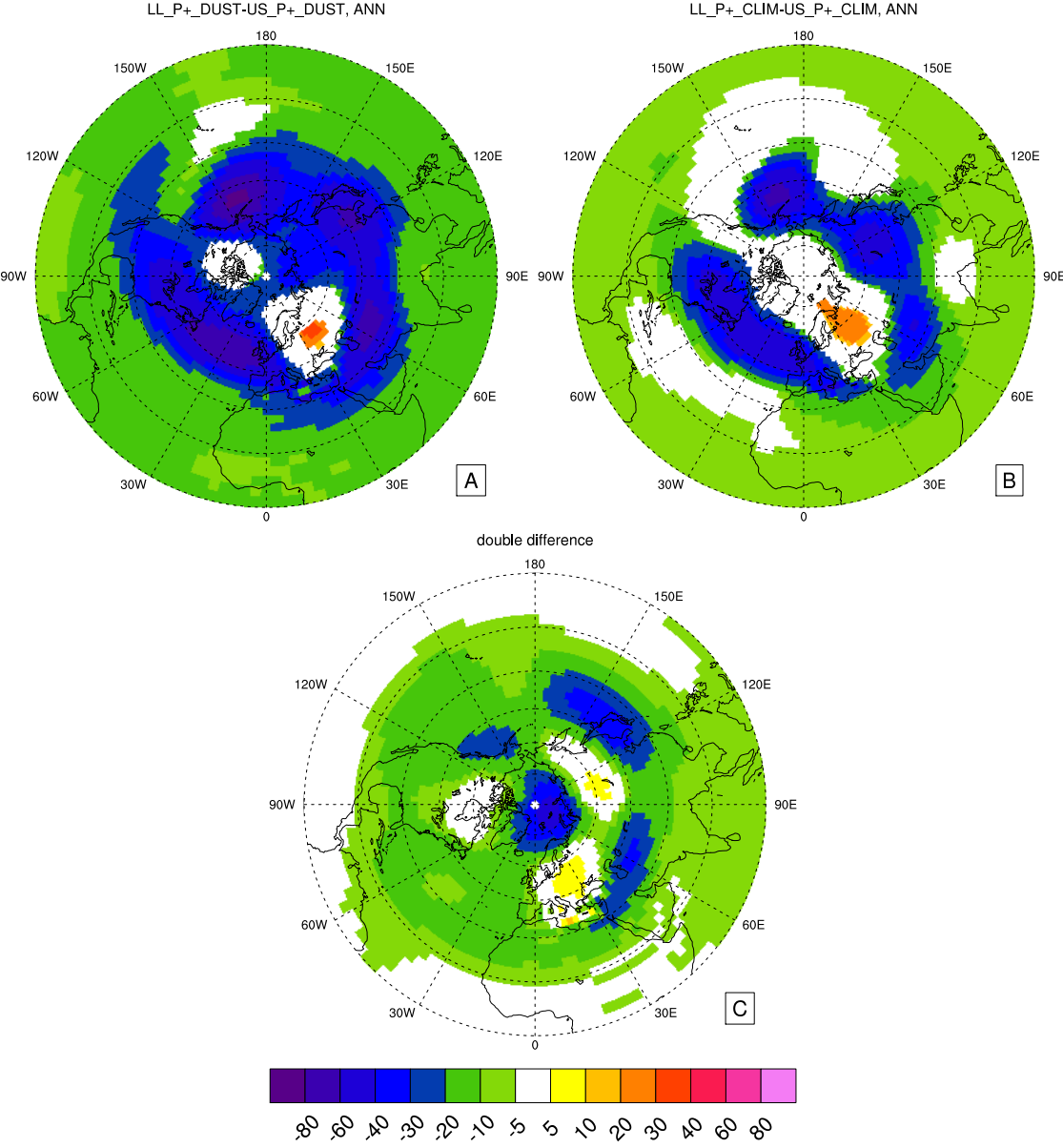
Figure 5.11: Northern Hemisphere Polar Stereographic plots of geopotential height anomalies (m) at precession maximum for the prognostic dust (A), climatological dust (B) and the double difference (C).

Fraction of sfc area covered by sea-ice Anomaly [fraction]
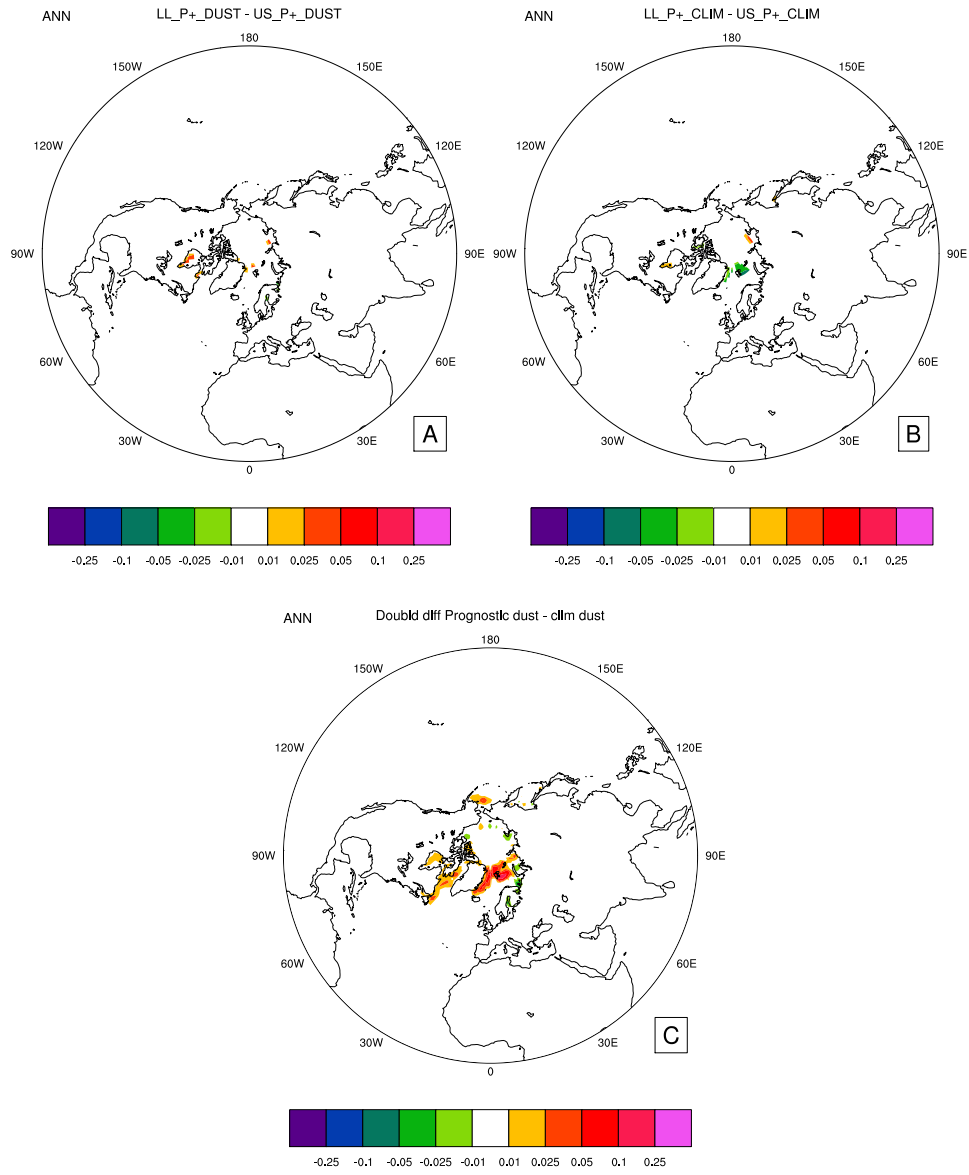
Figure 5.12: As Fig. 5.11 but for annual mean sea-ice anomaly at precession maximum.
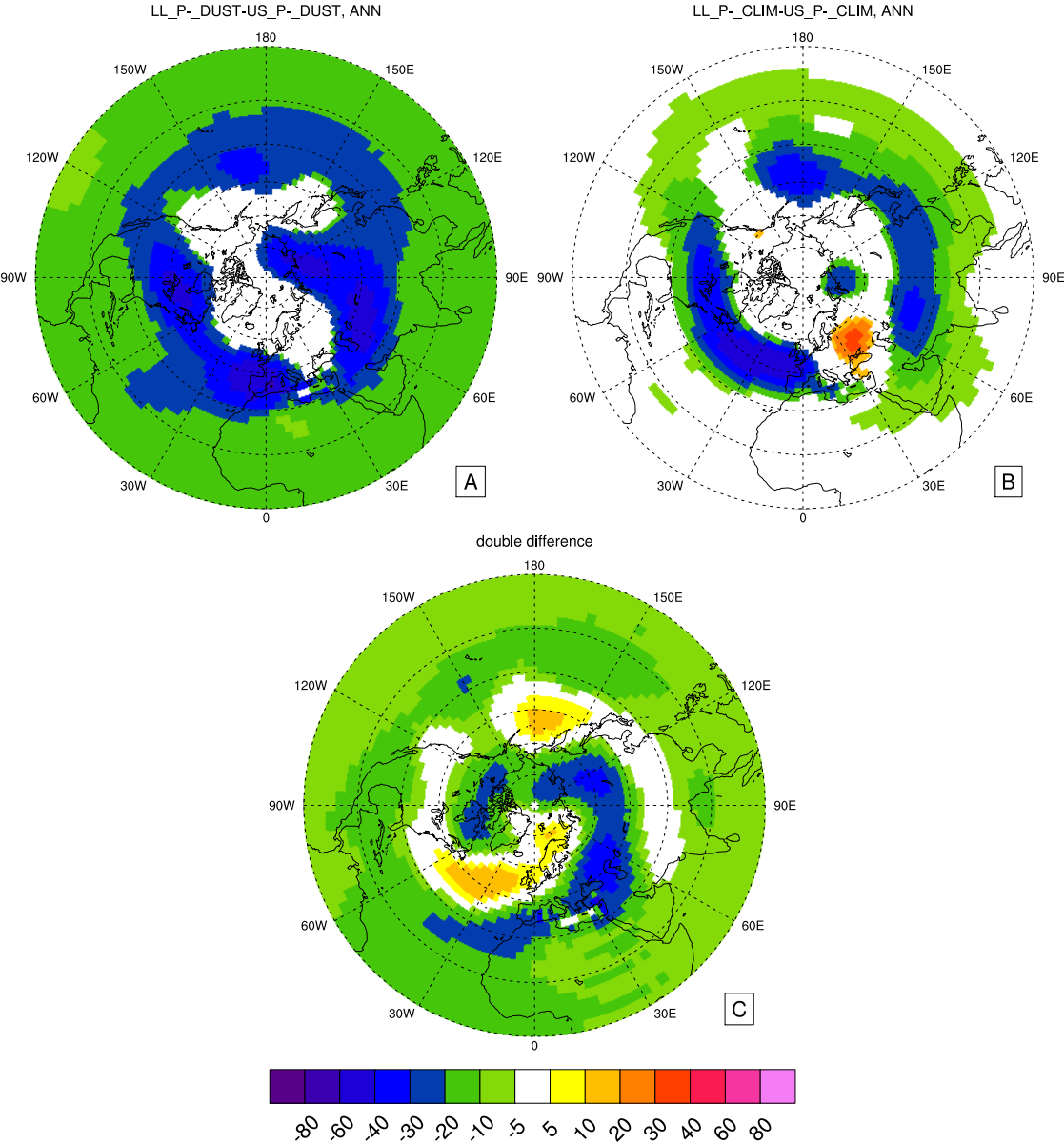
Figure 5.13: As Fig. 5.11 but for precession minimum.

Fraction of sfc area covered by sea-ice Anomaly [fraction]
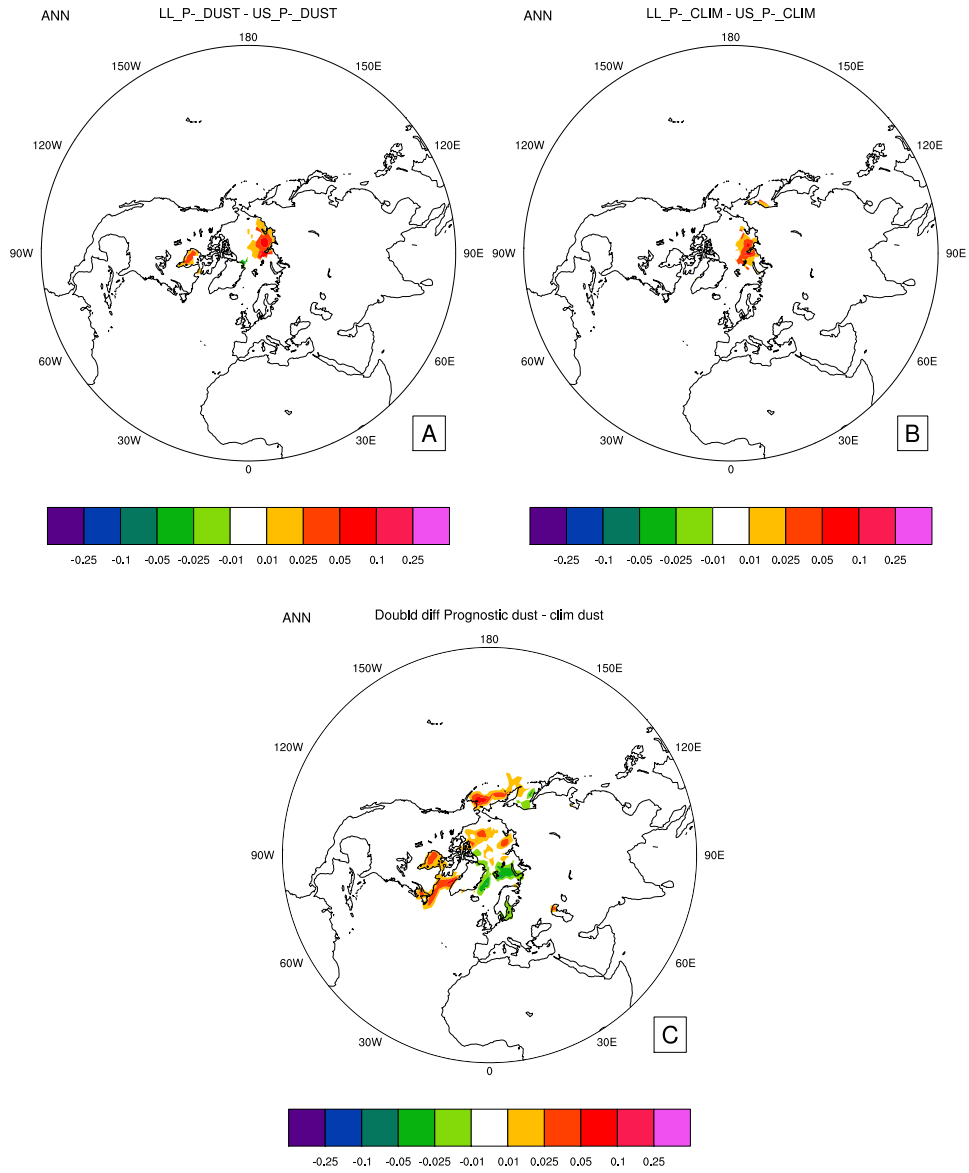
Figure 5.14: As Fig. 5.12 but for precession minimum.
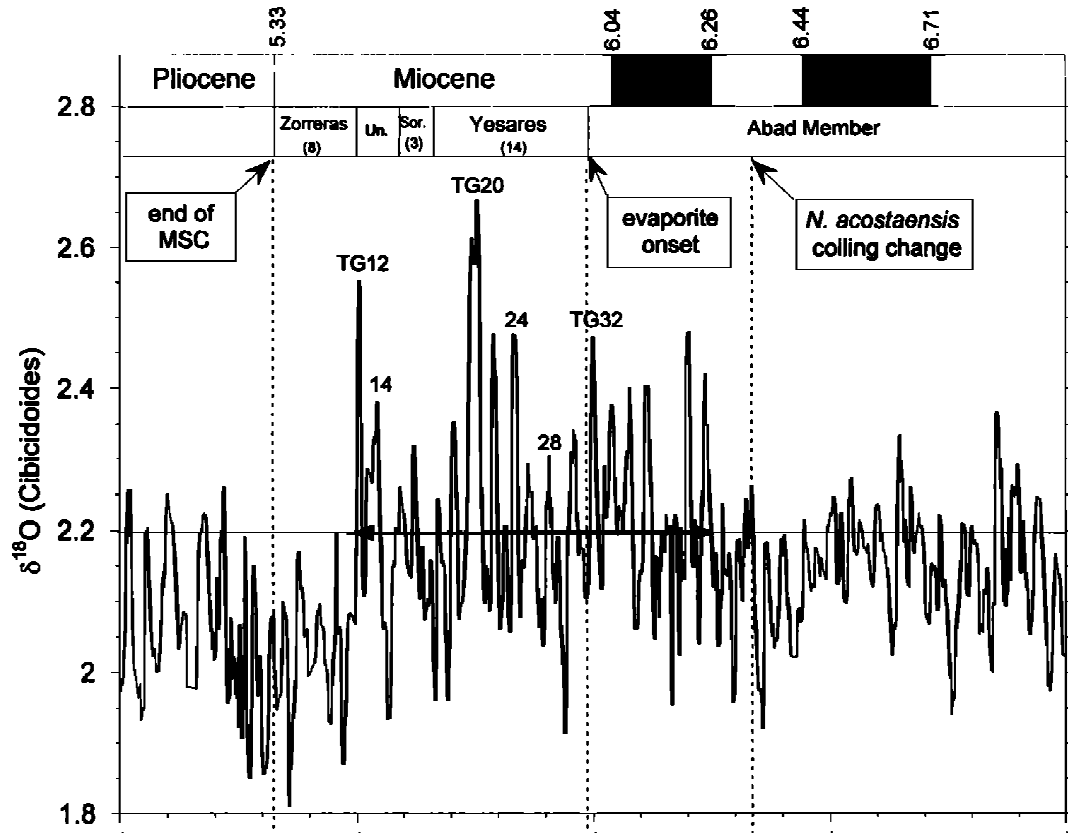
Figure 5.15: Figure 9 from Hodell et al. (2001). The TG12 and TG14 glacial events occur during the period of the "Messinian Gap" from 5.59 to 5.5 Ma. The time scale is from 5000 kyr to 7000 kyr with a tickmark at every 100 kyr. Oxygen isotope signals were measured on benthic foraminifera at ODP Site 982 (57°N, 15°W) in the North Atlantic. During the "Messinian Gap" the complete desiccation, erosion and deposition of halite occurred.

Chapter 6

Conclusions

6.1 Summary

Paleoclimate records indicate enhanced productivity in the Atlantic Ocean, increased aridity in Central Asia, and glaciation in the Northern hemisphere during the late Messinian. In this dissertation, we try to explain these mechanisms by modeling an extreme event that occurred within the MedSea. Climate changes in the MedSea have been correlated with the NAO (Hurrell (1995)). The MedSea also lies on the edge of the African-Asian waveguide, enhancing the teleconnectivity of the region. Regional hydrological changes have important feedbacks on the climate system on hemispheric to global scales. The oceanographic isolation of the MedSea resulted in substantial MedSea level fall beginning at 5.96 Ma and desiccation with subaerial exposure between 5.59 to 5.50 Ma. We used the NCAR Community Atmosphere Model to examine the climate response to reduced MedSea level, orbital variations, and to a MedSea dust source. Focusing our analysis on the large-scale pattern of variability that results from anomalous forcing allows us to validate our simulated atmospheric response against the geological proxy record, bringing a critical perspective to both the model output and the paleoclimate reconstruction.

In Chapter 3, we examined the atmospheric response to complete desiccation and lowered MedSea level while keeping other factors constant. Reduced MedSea level

increased evaporation and decreased precipitation, thus increasing the water deficit, making it difficult to sustain a partially filled MedSea, despite the significant increase in precipitation occuring over the Alps when the MedSea level is low. This response is consistent with evidence of increased weathering of the Alps during the Late Miocene. Globally, a MedSea depression generates planetary-scale atmospheric waves that lead to a hemispheric response that includes a notable deepening of the Aleutian Low and an equatorward shift in the Atlantic jet stream.

In Chapter 4, we examined how MedSea level change and orbital forcing combine to alter the hydrological budget. While reduced MedSea leads to strong heating in the summer, the elimination of horizontal heat transport into the MedSea during the winter prevents the LS SSTs from exceeding PD temperatures. Reduced MedSea level leads to enhanced precipitation and runoff from the northern borderlands. This feature is robust in all orbital forcing simulations. Since reduced sea level increases the water deficit of the MedSea, we find that precession minimum can only tip the MedSea water balance to allow for Lago-Mare deposits under relatively high MedSea level. Our LS simulations result in increased rainfall over the West African monsoon region. This result occurs under all precession signals. Greater runoff from the Guinea Coast may be correlated to enhanced organic carbon accumulation in this region during the Late Miocene.

In Chapter 5, we showed that a desiccated MedSea becomes a significant dust source. In our dust model, higher dust loading over North Africa and the MedSea results in regional warming. Since we do not account for the chemical composition of dust this result may change since salt is much more reflective than sand. Enhanced dust

loading over the tropical North Atlantic Ocean occurs when the Mediterranean is desiccated. This reduces the net radiative flux at the surface, which cools SSTs north of the Equator and shifts the ITCZ towards the Southern Hemisphere. The dustier Northern Hemisphere inhibits convective precipitation in the tropical North Atlantic and large-scale precipitation over Eastern Europe and into Central Asia, in agreement with proxy evidence of greater aridity in Central China between 6.2 and 5 Ma. Our results show that a desiccated Mediterranean has a significant impact on Northern Hemisphere sea-ice formation. While significant glaciation of the Northern Hemisphere did not occur until roughly 3 Ma (Moran *et al.* (2006)), there is proxy evidence of localized glaciation in the Gulf of Alaska and the North Atlantic as early as the latest Miocene, coinciding with the MSC (Jansen and Raymo (1996); Vidal et al., 2002; Zellers and Gary (2007)).

6.2 Paleo-vegetation

Tuenter *et al.* (2003) and Larrasoana *et al.* (2006) studied the effects of orbital forcing on the African summer monsoon and found that the stronger land-sea temperature contrast during precession minima resulted in an African summer monsoon that was displaced further poleward and had greater precipitation. The resulting vegetation changes over the Saharan desert due to greater precipitation are expected to give a positive feedback on the monsoon (Harrison et al., 1998). Vegetated land has a lower albedo than the desert; this leads to increased absorption

of radiation at the surface. Stronger surface heating would produce greater vertical ascent over the Saharan region, which can lead to more precipitation. Incorporating paleo-vegetation in modeling studies has resulted in significant temperature departures (Dutton and Barron (1997); Otto-Bliesner and Upchurch, 1997). Lohmann et al. (2006) showed significant warming of the global oceans in a Late Tortonian model configured with paleo-geography and paleo-vegetation (Figure 5, taken from Lohmann *et al.* (2006)). This shows the importance of incorporating a dynamical vegetation model in paleostudies.

Most paleoclimate modeling studies incorporate globally uniform soil texture and soil color due to the lack of quantitatively useful data. This has consequences for the availability of soil moisture (Shellito and Sloan, 2005) as well as surface temperature as soil color changes greatly affect the surface albedo. The amount of sand and clay in soil determines both soil thermal and hydrologic properties. Vegetation has important feedbacks on climate through biogeophysics, the hydrological cycle, and biogeochemistry. Vegetation changes will influence evapotranspiration, surface albedo, carbon feedbacks, and dust generation. These feedbacks have played important roles in past climate change (Dutton and Barron (1997); Otto-Bliesner and G.R. Upchurch (1997); Levis *et al.* (2004); Haywood and Valdes (2006)). Global reconstructions of biome distributions based on proxy data are sparse. The Pliocene Research, Interpretation and Synoptic Mapping (PRISM) project, part of the US Geological Survey climate change research effort, has made significant contributions to reconstructing the vegetation distribution of the Pliocene ($\sim$3.3-3.0 Ma) (Chandler *et al.* (2008)). Yet global maps of Late Miocene biomes are still unavail-

able (Lunt *et al.* (2008)) and few Late Miocene studies have examined the role of vegetation on climate during the MSC (Favre *et al.* (2007)). Favre et al. (2007) did not take into account the extreme fall in MedSea level, which has been shown to have a significant effect on both the local and global climate (Murphy et al., 2009). Implementing dynamical vegetation models can be used for obtaining Late Miocene vegetation maps. Incorporating the new vegetation distribution in paleoclimate modeling studies will provide the most accurate assessment of the climate and greatly improve our understanding of the climate during the MSC.

Preliminary results using our Late Miocene climate output to force a dynamic vegetation model shows large changes in the Mediterranean basin, central Asia, and Australia. Within the MedSea there is a change to desert vegetation while open woodlands and steppic ecosystems occur in the regions surrounding the dried basin. In central Asia, desert regions expand, which interestingly corresponds to the birth of the Taklimakan Desert (Sun and Liu, 2006).

6.3   Future work and implications

Mediterranean Outflow Water (MOW) provides a large source of salty water to the intermediate depths of the North Atlantic. MOW is one of three sources in the North Atlantic that contribute to North Atlantic Deep Water (NADW) formation (Talley (1996)), the subsurface component of the Atlantic meridional overturning circulation (MOC), and is characterized as a salinity and density maximum (Reid

(1994)). Due to its high salinity, MOW influences the variability of the Atlantic meridional overturning circulation (MOC) (Calmanti et al., 2006) but its impacts on the MOC are unresolved. Reid (1979) suggested that without the MOW, the strength of the NADW and Antarctic Bottom Water (AABW) formation would be reduced. Chan and Motoi (2003) found that eliminating the exchange of heat and salinity between the Mediterranean Sea (MedSea) and the Atlantic in a coupled model leads to a decrease in North Atlantic and Southern Ocean sea surface temperatures (SST). A 20We use the Coupled Climate System Model version 3 (CCSM3) to model the consequences of the closure of the straits connecting the MedSea to the Atlantic Ocean, focusing on the elimination of Mediterranean Outflow Water (MOW) from the Atlantic Ocean in the Late Miocene. We will examine important feedbacks in the MOC resulting from changes in the MOW and compare results to available proxy data. In addition, the increase in spatial resolution from T42 to T85 will allow enhanced realism and allow us to realistically model diurnally varying katabatic winds in the desiccated MedSea basin. Sun and Liu (2006) suggested that a 6 ppt reduction in global oceanic salinity during the MSC (Hsu *et al.* (1977)) may have resulted in greater sea ice formation due to the higher freezing point of the lower salinity water. Lower salinity and cooler waters in the North Atlantic due to the elimination of the MOW would reduce the MOC and lead to important consequences to global climate. We will determine if the elimination of the transport in the Gibraltar Strait, a lowered MedSea base level, and the climatic and hydrological impacts resulting from topographic forcing of a lowered MedSea basin, influences the salinity of the world ocean. The coupled system model may result in important

146

feedbacks in the thermohaline circulation as it is expected that the salinity of the Atlantic Ocean will be reduced due to the absence of MOW. Lower salinity and cooler waters in the North Atlantic would reduce the overturning circulation and lead to important consequences to global climate. This effect can subsequently influence global temperature through changes in heat transport.

Throughout the second half of the 20th century, the MedSea has become increasingly salty and warmer (Roether *et al.* (1996)). Under the IPCC-A2 global warming scenario, the MedSea is expected to warm an additional 3.1°C and the salinity will increase 0.48 partial salinity units by the end of the 21st century (Somot *et al.* (2006)). The Coupled Model Intercomparison Project (CMIP3) simulations predict a substantial decrease in freshwater input to the MedSea by the end of the 21st century as well as a warming-enhancement in evaportation, which would lead to increased salinity (Mariotti *et al.* (2008)). Warmer SSTs and increased salinity have competing effects on water density. Increased MedSea deep-water salinity over the last 40 years (Roether *et al.* (1996)) contributed to higher density values in MOW (Curry *et al.* (2003)). Future increases in the salinity of the MedSea would increase MOW at the Gibraltar Strait, since transport is driven by the density difference between the MedSea and the Atlantic Ocean. While increased MedSea SSTs decrease the density of water and reduce deep-water formation. Beyond changes in MedSea circulation, our results suggest a drier MedSea region results in arid conditions over Eastern Europe and the Middle East. We also find that MedSea warming and reduced MedSea sea-level results in a hemispheric response that can bring about signficiant changes in the storm tracks and North Pacific and North Atlantic SSTs.

147

Decreased atmospheric stability may also lead to more extreme precipitation events in the area. Increased population growth, greater irigation, exploited ground water and drier conditions predicted for the future will all exacerbate the water crisis in the peri-Mediterranean region. Future changes in the MedSea are not only important regionally but may also impact climate conditions throughout the Northern Hemisphere.

Bibliography

Baker, P., Rigsby, C., Seltzer, G., Fritz, S., Lowenstein, T., Bacher, N., and Veliz, C. (2001). Tropical climate changes at millennial and orbital timescales on the Bolivian Altiplano. *Nature*, **409**, 698–701.

Bartol, J. and Govers, R. (2009). Flexure due to the Messinian-Pontian sea level drop in the Black Sea. *Geochem., Geophys., Geosyst..*, **10**, Q10013.

Billups, K., Rickaby, R. M., and Schrag, D. (2004). Cenozoic pelagic Sr/Ca records: Exploring a link to paleoproductivity. *Paleoceanography*, **19**(PA3005,doi:10.1029/2004PA001011.), 698–701.

Braconnot *et al.* (2007). Results of PMIP2 coupled simulations of the Mid-Holocene and Last Glacial Maximum Part 2: feedbacks with emphasis on the location of the ITCZ and mid- and high latitudes heat budget. *Clim. Past*, **3**, 279–296.

Brooks, N. and Legrand, M. (2000). *Dust variability over northern Africa and rainfall in the Sahel*. Kluwer Academic Publishers.

Chandler, M., Dowsett, H., and Haywood, A. (2008). The PRISM Model/Data Cooperative: Mid-Pliocene data-model comparisons. *PAGES News*, **16**, 24–25.

CIESM (2008). The Messinian Salinity Crisis from mega-deposits to microbiology - A consensus report. Technical report, CIESM Vorkshop Monograph (F. Briand, Ed.), Monaco.

Clauzon, G., Suc-J.-P., G., F., B. A., and Loutre, M.-F. (1996). Alternate interpretation of the Messinian salinity crisis: Controversy resolved? *Geol.*, **24**, 363–366.

Collins, W., Rasch, P., Boville, B., Hack, J., McCaa, J., Williamson, D., Kiehl, J., Briegleb, B., Bitz, C., Lin, S.-J., Zhang, M., and Dai, Y. (2004). Description of the NCAR Community Atmosphere Model (3.0), NCAR/TN–464+STR, NCAR Technical Note. Technical report, NCAR, Boulder, CO, http://www.ccsm.ucar.edu/models/atm-cam/docs/description/.

Curry, R., Dickson, B., and Yashayaev, I. (2003). A change in the freshwater balance of the atlantic ocean over the past four decades. *Nature*, **426**, 826–828.

da Silva, A., Young, C., and Levitus, S. (1994). *Algorithms and Procedures*, volume 6. NOAA Atlas NESDIS.

Darbas, G., Nazik, A., Temel, A., and Gurbuz, K. (2008). A paleoenvironmental test of the Messinian Salinity Crisis using Miocene-Pliocene clays in the Adana Basin, Southern Turkey. *Applied Clay Science*, **40(1-4)**, 108–118.

Duggen, S., Hoernle, K., van der Boogard, P., Rupke, L., and Phipps Morgan, J. (2003). Deep roots of the Messinian salinity crisis. *Nature*, **422**, 602–606.

Dutton, J. and Barron, E. (1997). Miocene to present vegetation changes; a possible piece of the Cenozoic cooling puzzle. *Geology.*, **25**, 39–41.

Evan, A. T., Vimont, D., Heidinger, A., Kossin, J., and Bennartz, R. (2009). The role of aerosols in the evolution of tropical North Atlantic ocean temperature anomalies. *Science*, **234**, 779–781.

Fauquette, S., Suc, J.-P., Bertini, A., Popescu, S.-M., Warny, S., Taoufiq, N., Villa, M.-J. P., Chikhi, H., Feddi, N., Subally, D., Clauzon, G., and Ferrier, J. (2006). How much did climate force the Messinian salinity crisis? Quantified climatic conditions from pollen records in the Mediterranean region. *Palaeogeography, Palaeoclimatology, Palaeoecology*, **238**, 281–301.

Favre, E., Francois, L., Fluteau, F., Cheddadi, R., Thevenod, L., and Suc, J.-P. (2007). Messinian vegetation maps of the Mediterranean region using models and interpolated pollen data. *Geobios*, **43**, 433–443.

Floegel, S. and Wagner, T. (2006). Insolation-control on the Late Cretaceous hydrological cycle and tropical African climate-global climate modelling linked to marine climate records. *Palaeogeography, Palaeoclimatology, Palaeoecology*, **235**, 268–304.

Francois, L., Ghislain, M., Otto, D., and Micheels, A. (2006). Late Miocene vegetation reconstruction with the CARAIB model. *Palaeogeography, Palaeoclimatology, Palaeoecology*, **238**, 302–320.

Gargani, J. (2004). Modeling of the erosion in the Rhone Valley during the Messinian crisis (France). *Quat. Int.*, **121**, 13–22.

Gargani, J. and Rigollet, C. (2007). Mediterranean Sea level variations during the Messinian crisis. *Geophys. Res. Lett.*, **34**, L10405.

Gillet, H., Lericolais, G., and Rehault, J.-P. (2007). Messinian event in the black sea: Evidence of a Messinian erosional surface. *Marine Geology.*, **244**, 142–165.

Gladstone, F., Flecker, R., Valdes, P., Lunt, D., and Markwick, P. (2007). The Mediterranean hydrologic budget from a Late Miocene global climate simulation. *Palaeogeography, Palaeoclimatology, Palaeoecology*, **251**, 254–267.

Griffin, D. (2002). Aridity and humidity: two aspects of the late Miocene climate of North Africa and the Mediterranean. *Palaeogeography, Palaeoclimatology, Palaeoecology*, **182**, 65–91.

Guo, Z., Peng, S., Hao, Q., adn Z. An, P. B., and Liu, T. (2004). Late MiocenePliocene development of Asian aridification as recorded in the Red–Earth Formation in northern China. *Global and Planetary Change*, **41**, 135–145.

Hastenrath, S. (1990). Decadal-scale changes of the circulation in the tropical atlantic sector associated with sahel drought. *Int. J. Climatol.*, **10**, 459–472.

Haywood, A. and Valdes, P. (2006). Vegetation cover in a warmer world simulated using a dynamic global vegetation model for the Mid-Pliocene. *Palaeogeography, Palaeoclimatology, Palaeoecology*, **237**, 412–427.

Hilgen, F., Kuiper, K., Krijgsman, W., Snel, E., and van der Laan, E. (2007). Astronomical tuning as the basis for high resolution chronostratigraphy: the intricate history of the Messinian salinity crisis. *Stratigraphy*, **4**, 231–238.

Hodell, D., Curtis, J., Sierro, F., and Raymo, M. (2001). Correlation of late Miocene to early Pliocene sequences between the Mediterranean and North Atlantic. *Paleoceanography*, **16**, 164–178.

Hsu, K., W.B.F., R., and Cita, M. (1973). Late Miocene desiccation of the Mediterranean. *Nature*, **242**, 240–244.

Hsu, K., Montadert, L., Bernouilli, D., Cita, M., Erickson, A., Garison, R., Kidd, R., Melieres, F., Muller, C., and Wright, R. (1977). History of the Mediterranean salinity crisis. *Nature*, **267**, 399–403.

Hurrell, J. (1995). Decadal trends in the north atlantic oscillation: Regional temperatures and precipitation. *Science*, **269**, 676–679.

Jansen, E. and Raymo, M. (1996). New frontiers on past climates. *Proceedings of the Ocean Drilling Program, Initial Reports*, **162**, 5–20.

Jones, C., Mahowald, N., and Luo, C. (2004). Observational evidence of African desert dust intensification of easterly waves. *Geophys. Res. Lett.*, **31**, L17208.

King, T., Ellis, W., Murray, D., Shackleton, N., and Harris, S. (1997). Miocene evolution of carbonate sedimentation at the ceara rise: A multivariate data/proxy approach. *Proc. Ocean Drill. Program Sci. Results*, **154**, 349–365.

Krijgsman, W. and Meijer, P. (2008). Depositional environments of the Mediterranean Lower Evaporites of the Messinian salinity crisis: Constraints from quantitative analyses. *Mar. Geol.*, **253**, 73–81.

Krijgsman, W., Hilgen, F., Raffi, I., Sierro, F., and Wilson, D. (1999). Chronology, causes and progression of the Messinian salinity crisis. *Nature*, **400**, 652–655.

Krijgsman, W., Fortuin, A., Hilgen, F., and Sierro, F. (2001). Astrochronology

for the Messinian Sorbas Basin (SE Spain) and orbital (precessional) forcing for evaporite cyclicity. *Sed. Geol.*, **140**, 43–60.

Krissek, L. (1995). Cenozoic ice-rafting records from leg 145 sites in the North Pacific: Late Miocene onset, late Pliocene intensification, and Pliocene-Pleistocene events. *Proceedings of the Ocean Drilling Program, Scientific Results*, **145**, 179–194.

Kutzbach, J. (1981). Monsoon climate of the Early Holocene: Climate Experiment with the Earth's Orbital Parameters for 9000 years ago. *Science*, **214**, 59–61.

Kutzbach, J. and Otto-Bliesner, B. (1982). The Sensitivity of the African-Asian Monsoonal Climate to Orbital Parameter Changes for 9000 yr B.P. in a Low-resolution General Circulation Model. *J. Atmos. Sci.*, **39**, 1177–1188.

Kutzbach, J., Bonan, G., Foley, J., and Harrison, S. (1996). Vegetation and soil feedbacks on the response of the African monsoon to orbital forcng in the early to middle Holocene. *Nature.*, **384**, 623–626.

Larrasoana, J., Roberts, A., Hayes, A., Wehausen, R., and Rohling, E. (2006). Detecting missing beats in the Mediterranean climate rhythm from magnetic identification of oxidized sapropels (Ocean Drilling Program Leg 160). *Physics of the Earth and Planetary Interiors*, **156**, 283–293.

Laskar, J., Joutel, F., and Boudin, F. (1993). Orbital, precessional and insolation quantities for the Earth from -20 myr to +10 myr. *Astronomy and Astrophysics.*, **270**, 522–533.

Levis, S., Bonan, G., and Bonfils, C. (2004). Soil Feedback Drives the Mid-Holocene North African Monsoon Northward in Fully Coupled CCSM2 Simulations with a Dynamic Vegetation Model. *Clim. Dyn.*, **23**, 791–802.

Lohmann, G., Butzn, M., Micheels, A., Bickert, T., and Mosbrugger, V. (2006). Effect of vegetation on the Late Miocene ocean circulation. *Clim. Past Discuss*, **2**, 605–631.

Lunt, D., Flecker, R., Valdes, P., Salzmann, U., Gladstone, R., and Haywood, A. (2008). A methodology for targeting palaeo proxy data acquisition: A case study for the terrestrial late Miocene. *Earth and Planetary Sciences*, **271**, 53–62.

Lyle, M., Barron, J., Bralower, T., Huber, M., Lyle, A., Ravelo, A., Rea, D., and Wilson, P. (2008). Pacific ocean and Cenozoic evolution of climate. *Reviews of Geophysics*, **46**, 2002–2008.

Macdonald, A., Candela, J., and Bryden, H. (1994). An Estimate of the Net Heat Transport Through the Strait of Gibraltar. *Coastal and Estuarine Studies.*, **46**, 13–32.

Mahowald, N., Yoshioka, M., Collins, W., Conley, A., Fillmore, D., and Coleman, D. (2006). Climate response and radiative forcing from mineral aerosols during the last glacial maximum, pre-industrial, current and doubled-carbon dioxide climates. *Geophys. Res. Lett.*, **33**, L20705, doi:10.1029/2006GL026126.

Mariotti, A., Struglia, M., Zeng, N., and Lau, K.-M. (2002). The hydrological

cycle in the Mediterranean region and implications for the water budget of the Mediterranean Sea. *J. Clim.*, **15**, 1634–1690.

Mariotti, A., Zeng, N., Yoon, J.-H., Artale, V., Navarra, A., Alpert, P., and Li, L. (2008). Mediterranean water cycle changes: transition to drier 21st century conditions in observations and cmip3 simulations. *Environmental Research Letters*, **3**, 044001 (8pp).

Martin, J. (1990). Glacial-interglacial co2 exchange: The iron hypothesis. *Paleoceanography*, **5**, 1–13.

Martinez, N., Murray, R., Thunell, R., Peterson, L., Muller-Karger, F., Astor, Y., and Varela, R. (2007). Modern climate forcing of terrigenous deposition in the tropics (Cariaco Basin, Venezuela). *Earth and Planetary Science Letters*, **264**, 438–451.

Meehl, G., Arblaster, J., Lawrence, D., Seth, A., Schneider, E., Kirtman, B., and Min, D. (2006). Monsoon regimes in the CCSM3. *J. of Clim.*, **19**(11), 2482.

Meijer, P. (2006). A box model of the blocked-outflow scenario for the Messinian salinity crisis. *Earth and Planetary Sci. Lett.*, **248**, 471–479.

Meijer, P. and Krijgsman, W. (2005). Quantitative analysis of the desiccation and re-filling of the Mediterranean during the Messinian salinity crisis. *Earth Planet Sci. Lett.*, **240**, 510–520.

Meijer, P., Slingerland, R., and M.J.R., W. (2004). Tectonic control on past circula-

tion of the Mediterranean Sea: A model study of the late Miocene. *Paleoceanography*, **19**, PA1026, doi:10.1029/2003PA000956.

Micheels, A., Bruch, A., Uhl, D., Utescher, T., and Mosbrugger, V. (2007). A Late Miocene climate model simulation with echam4/ml and its quantitative validation with terrestrial proxy data. *Palaeogeography, Palaeoclimatology, Palaeoecology*, **253**, 251–270.

Miller, R., Tegen, I., and Perlwitz, J. (2004). Surface radiative forcing by soil dust aerosols and the hydrologic cylce. *J. Geophys. Res.*, **109**, D04203.

Moran, K., Backman, J., Brinkhuis, H., Clemens, S., Cronin, T., Dickens, G., Eynaud, F., Gattacceca, J., and et al. (2006). The Cenozoic palaeoenvironment of the Arctic Ocean. *Nature*, **441**, 601–605.

Murphy, L., Kirk-Davidoff, D., Mahowald, N., and Otto-Bliesner, B. (2009). A numerical study of the climate response to lowered Mediterranean Sea level during the Messinian salinity crisis. *Palaeogeography, Palaeoclimatology, Palaeoecology*, **279**, 41–59.

Nicholson, S. (2000). Land surface processes and sahel climate. *Rev. Geophys.*, **38**, 117–139.

Nolet, G. and Corliss, B. (1990). Benthic foraminiferal evidence for reduced deepwater circulation during sapropel deposition in the Eastern Mediterranean. *Mar. Geol..*, **94**, 109–130.

Okin, G., Mahowald, N. M., Chadwick, O., and Artaxo, P. (2004). The impact of desert dust on the biogeochemistry of phosphorus in terrestrial ecosystems. *Global Biogeochemical Cycles*, **18**, 10.1029/2003GB002145.

Oleson, K., Dai, Y., Yongjiu, D., Bonan, G., Bosilovich, M., Dickinson, R., Dirmeyer, P., Hoffman, F., Houser, P., Levis, S., Niu, G., Thornton, P., Vertenstein, M., Yang, Z., and Zeng, X. (2004). Technical description of the Community Land Model (CLM), NCAR/TN–461+STR, NCAR Technical Note. Technical report, NCAR, Boulder, CO, http://www.ccsm.ucar.edu/models/atm-cam/docs/description/.

Otto-Bliesner, B. and G.R. Upchurch, J. (1997). Vegetation induced warming of high latitude regions during the Late Cretaceous period. *Nature*, **385**, 804–807.

Popescu, S.-M., Suc, J.-P., and Loutre, M.-F. (2006). Early pliocene vegetation changes forced by eccentricity-precession. Example from Southwestern Romania. *Palaeogeography, Palaeoclimatology, Palaeoecology*, **238**, 340–348.

Rea, D. (1994). The paleoclimatic record provided by eolian deposition in the deep sea: The geological history of wind. *Reviews of Geophysics*, **32**, 159–195.

Reid, J. (1994). On the total geostrophic circulation of the north-atlantic ocean - flow patterns, tracers and transports. *Prog. Ocean.*, **33**, 1–92.

Rodwell, M. and Hoskins, B. (1996). Monsoons and the dynamics of deserts. *Q. J. R. Meteorol. Soc.*, **122**, 1385–1404.

Roether, W., Manca, B., Klein, B., Bregant, D., Georgopoulos, D., Beitzel, W., Kovacevic, V., and Luchetta, A. (1996). Recent chanes in eastern mediterranean deep waters. *Science*, **271**, 333–334.

Rosenfeld, D., Rudich, Y., and Lahav, R. (2001). Desert dust suppressing precipitation: A possible desertification feedback loop. *Proc. Nat. Acad. Sci.*, **98**, 975–980.

Rossignol-Stick, M. (1983). Afircan monsoons, an intermediate climate response to orbital insolation. *Nature.*, **304**, 46–49.

Roveri, M., Bassetti, M., and Lucchi, F. R. (2001). The Mediteranean Messinian salinity crisis: an Apennine foredeep perspective. *Sediment. Geol..*, **140**, 201–214.

Rowell, D. (2003). The impact of Mediterranean SSTs on the Sahelian Rainfall Season. *J. of Clim.*, **16**, 849–862.

Ruddiman, W. and Kutzbach, J. (1989). Forcing of late Cenozoic northern hemisphere climate by uplift in southern Asia and the American West. *J. Geophys. Res.*, **94**, 1840918427.

Sierro, F., Flores, J., Zammareno, I., Vazquez, A., Utrilla, R., Frances, G., Hilgen, F., and Krijgsman, W. (1999). Messinian pre-evaporite sapropels and precession-induced oscillations in western Mediterranean climate. *Mar. Geol.*, **153**, 137–146.

Somot, S., Sevault, F., and Deque, M. (2006). Transient climate change scenario simulation of the mediterranean sea for the twenty-first century using a high-resolution ocean circulation model. *Clim. Dyn.*, **27**, 851–879.

Stein, R. (1985). Late Neogene changes of paleoclimate and paleoproductivity off northwest Africa (dsdp site 397). *Palaeogeography, Palaeoclimatology, Palaeoecology*, **49**, 47–59.

Stepphun, A., Micheels, A., Geiger, G., and Mosbrugger, V. (2006). Reconstructing the Late Miocene climate and oceanic heat flux using the AGCM ECHAM4 coupled to a mixed-layer ocean model with adjusted flux correction. *Palaeogeography, Palaeoclimatology, Palaeoecology*, **238**, 399–423.

Sun, J. and Liu, T. (2006). The age of the Taklimakan desert. *Science*, **312**, 1621.

Talley, L. (1996). North atlantic circulation and variability reviewed for the cnls conference. *Physica D*, **98**, 625–646.

Tegen, I., Harrison, S., Kohfeld, K., Prentice, I., Coe, M., and Heimann, M. (2002). Impact of vegetation and preferential source areas on global dust aerosol: Results from a model study. *J. Geophys. Res.*, **107**, 4576, doi:10.1029/2001JD000963.

Tiedemann, R., Sarnthein, M., and Stein, R. (1989). Climatic changes in the western Sahara: Aeolo-marine sediment record of the last 8 million years (Sites 657-661). *Proceedings of the Ocean Drilling Program*, **108**, 241–277.

Timmermann, A. and Jin, F.-F. (2002). Phytoplankton influences on tropical climate. *Geophys. Res. Lett.*, **29**, 2104, doi:10.1029/2002GL015434.

Tuenter, E., Weber, S., Hilgen, F., and Lourens, L. (2003). The response of the African summer monsoon to remote and local forcing due to precession and obliquity. *Global and Planetary Change*, **36**, 219–235.

Vidal, L., Bickert, T., Wefer, G., and Rohl, U. (2002). Late Miocene stable isotope stratigraphy of SE Atlantic ODP Site 1085: Relation to Messinian events. *Mar. Geol.*, **180**, 71–85.

Willett, S., Schlunegger, F., and Picotti, V. (2006). Messinian climate change and erosional destruction of the central European Alps. *Geol.*, **34**, 613–616.

Wolf, T. and Thiede, J. (1991). History of terrigenous sedimentation during the past 10 my in the North Atlantic (ODP Legs 104, 105 and DSDP 81. *Marine Geology*, **101**, 83–102.

Xie, P. and Arkin, P. (1996). Analysis of global monthly precipitation using gauge observations, satellite estimates, and numerical model predictions. *J. Clim.*, **9**, 840–858.

Yoshioka, M., Mahowald, N., Conley, A., Collins, W., Fillmore, D. W., Zender, C., and Coleman, D. (2007). Impact of desert dust radiative forcing on sahel precipitation: Relative importance of dust compared to sea surface temperature variations, vegetation changes, and greenhouse gas warming. *J. of Clim.*, **20**, 1445–1467.

Zachos, J., Pagani, M., Sloan, L., Thomas, E., and Billups, K. (2001). Trends, rhythms and aberrations in global cliamte, 65 Ma to present. *Science*, **292**, 686–693.

Zellers, S. and Gary, A. (2007). Unmixing foraminiferal assemblages: polytopic

vector analysis applied to Yakataga Formation sequences in the offshore Gulf of Alaska. *Palaios*, **22**, 47–59.

Zheng, H., Powell, C. M., Rea, D., Wang, J., and Wang, P. (2004). Late Miocene and mid-Pliocene enhancement of the East Asian monsoon as viewed from the land and sea. *Global and Planetary Change*, **41**, 147–155.

Zhisheng, A., Kutzbach, J., Prell, W., and Porter, S. (2001). Evolution of Asian monsoons and phased uplift of Himalaya-Tibetan plateau since Late Miocene times. *Nature*, **411, doi:10.1038/35075035**, 62–66.